Lehrstuhl für Biomedizinische Physik
Fakultät für Physik
Technische Universität München

Phase-contrast Radiography and Dark-field Computed Tomography for the Detection of Bronchial and Pulmonary Pathologies

Stephan Markus Umkehrer

Dissertation

April 2021

Betreuer:

Prof. Dr. Franz Pfeiffer

Prof. Dr. Julia Herzen

Technische Universität München

Technische Universität München
Fakultät für Physik

Phase-contrast Radiography and Dark-field Computed Tomography for the Detection of Bronchial and Pulmonary Pathologies

Stephan Markus Umkehrer

Vollständiger Abdruck der von der Fakultät für Physik der Technischen Universität München zur Erlangung des akademischen Grades eines

Doktors der Naturwissenschaften (Dr. rer. nat.)

genehmigten Dissertation.

Vorsitzender:	Prof. Dr. Martin Zacharias
Prüfer der Dissertation:	1. Prof. Dr. Franz Pfeiffer
	2. Prof. Dr. Jan Jakob Wilkens

Die Dissertation wurde am 03.05.2021 bei der Technischen Universität München eingereicht und durch die Fakultät für Physik am 02.03.2022 angenommen.

Abstract

In the past decades, a number of efforts have been made to successfully introduce the complementary contrast modalities of X-ray phase contrast and dark-field to conventional and already established X-ray absorption, both in scientific research and in (pre)clinical practice. Among several methods the approach of grating-based X-ray interferometry, which consists of three gratings, has proven to be one of the most promising technique. The advantage of this method is that the soft tissue-differentiating and small-angle scattering-sensitive modalities can also be resolved with a conventional, incoherent X-ray tube.

In order to prove the clinical benefit of this method, the fundamentals for this work were established in previous PhD theses. These dealt with the development of a first prototype small animal phase contrast and dark-field CT scanner on a rotating gantry, the implementation of data processing and reconstruction algorithms, and the demonstration of some primarily radiography-based dark-field applications. The present work, titled 'Phase-contrast Radiography and Dark-field Computed Tomography for the Detection of Bronchial and Pulmonary Pathologies', aims at the further technical development and optimization - especially with focus on three-dimensional imaging - and a first application of phase contrast in diagnostics.

The current configuration of the setup is optimized for two-dimensional radiographic imaging, among other things due to the long exposure times and the resulting insufficient number of angular projections. Within the context of this work, this limitation is to be overcome by hardware optimization. A first step towards this goal is done by improving the configuration of the grating interferometer in order to obtain a homogeneous intensity and visibility distribution over the entire field of view. Furthermore, the integration of a new detector allows the exposure time of individual projections to be reduced, so that the time gained can be used to acquire images at additional angles. The last optimization approach performed in this thesis is the restructuring of the data acquisition protocol. Thus, the limited time available is optimally used to ensure the maximum number of angle projections during acquisition, thus obtaining a reconstruction volume of best possible quality. Parts of these findings were published in the following study: Umkehrer et al., Optimization of in-vivo murine X-ray dark-field computed tomography, Review of Scientific Instruments (2019).

Today, it is impossible to imagine everyday clinical practice without absorption-based X-ray radiography in particular. However, dark-field radiography has already shown great potential for application in the field of lung imaging in the course of several preclinical studies. In contrast, the diagnostic value of the second additional contrast

modality, the phase-contrast signal, has not yet been demonstrated in-vivo in preclinical research. Within this work the first potential application for the phase-contrast signal in clinical routine is presented. A model for lung transplantation in mice is used for this purpose, as a result of which pulmonary atelectasis and bronchial pathologies have occurred. The tissue differentiating property of phase contrast helps to diagnose these pathologies in terms of bronchial stenoses or bronchial truncations in phase-contrast radiographs. The findings of this study was published under Umkehrer et al., A proof-of principal study using phase-contrast imaging for the detection of large airway pathologies after lung transplantation. Scientific Reports (2020).
The benefit of dark-field radiography for the detection and diagnosis of lung tumors has already been demonstrated in a previous study. However, this study included a high number of major tumor nodules. In this work, the advantage of dark-field CT over radiography limited to two dimensions is shown, since the scattered signal can be examined in three-dimensional propagation. Parts of this study are currently under preparation to be published.

Zusammenfassung

In den vergangenen Jahrzehnten wurden eine Reihe von Bemühungen unternommen, um neben der konventionellen und bereits etablierten Röntgenabsorption, die komplementären Kontrastmodalitäten des Röntgen-Phasenkontrasts und -Dunkelfelds, sowohl in der Forschung als auch im (vor-)klinischen Alltag zugänglich zu machen. Neben vielen anderen Ansätzen, hat sich dabei die Methode der gitterbasierten Röntgeninterferometrie als die vielversprechendste Technik herausgestellt. Der Vorteil dieser Methodik ist, dass die gewebedifferenzierende und kleinwinkelstreuungsensitive Modalitäten auch mit einer konventionellen, inkohärenten Röntgenröhre aufgelöst werden können.
Um den klinischen Mehrwert dieser Methode unter Beweis zu stellen, wurde im Rahmen vorangegangener Dissertationen der Grundstein dieser Arbeit gelegt. Dabei behandelten diese die Entwicklung eines ersten Prototyp Kleintier Phasenkontrast- und Dunkelfeldcomputertomographs auf einer rotierenden Gantry, die Implementierung der Datenverarbeitung und Rekonstruktionsalgorithmen, sowie der Demonstration einiger primär radiographiebasierter Dunkelfeld-Anwendungen. Darauf aufbauend zielt die vorliegende Arbeit mit dem Titel 'Phase-contrast Radiography and Dark-field Computed Tomography for the Detection of Bronchial and Pulmonary Pathologies' auf die technische Weiterentwicklung und Optimierung - insbesondere mit Fokus auf die dreidimensionale Bildgebung – sowie einer ersten Anwendung des Phasenkontrast in der Diagnostik ab.
Die derzeitige Konfiguration des Aufbaus ist, unter anderem aufgrund der langen Belichtungszeiten und der daraus resultierenden ungenügenden Anzahl von Winkelprojektionen, auf die zweidimensionale, radiographische Bildgebung optimiert. Im Rahmen dieser Arbeit soll diese Limitierung durch diverse hardwareseitige Optimierungen überwunden werden. Ein erster Schritt zu diesem Ziel ist die Verbesserung der Konfiguration des Gitterinterferometers, um eine homogene Intensitäts- und Visibilitätsverteilung über das gesamte Sichtfeld zu erhalten. Des Weiteren ermöglicht der Einbau eines neuen Detektors eine Reduzierung der Belichtungszeit einzelner Projektionen, sodass die eingesparte Zeit zur Aufnahme zusätzlicher Winkel genutzt werden kann. Der letzte in dieser Arbeit durchgeführte Optimierungsansatz ist die Umstrukturierung des Datenakquisitionsprotokolls. So wird die begrenzte, zur Verfügung stehende Zeit optimal genutzt, um die maximale Anzahl an Winkelprojektionen zu gewährleisten, und so ein Rekonstruktionsvolumen in bestmöglicher Qualität zu erhalten. Teile dieser Erkenntnisse wurden in folgender Studie veröffentlicht: Umkehrer et al., Optimization of in-vivo murine X-ray dark-field computed tomography., Review of

Scientific Instruments (2019).
Im klinischen Alltag ist heutzutage vor allem die absorptionsbasierte Röntgenradiographie nicht mehr wegzudenken. Allerdings bewies auch die Dunkelfeldradiographie im Rahmen einiger vorklinischen Studien bereits großes Anwendungspotenzial im Bereich der Lungenbildgebung. Im Gegensatz dazu, konnte der diagnostische Mehrwert der zweiten zusätzlichen Kontrastmodalität, dem Phasenkontrast-Signal, in der vorklinischen Forschung in-vivo bisher noch nicht nachgewiesen werden. Im Rahmen dieser Arbeit wird die erste mögliche Anwendung des Phasenkontrastsignals in der klinischen Routine vorgestellt. Dazu wird ein Modell für die Lungentransplantation bei Mäusen verwendet, in deren Folge morphologische Änderungen in Form von pulmonalen Atelektasen und Bronchialpathologien aufgetreten sind. Die gewebedifferenzierende Eigenschaft des Phasenkontrastes hilft dabei die Bronchialpathologien in zweidimensionalen Radiographien zu diagnostizieren. Die Erkenntnisse dieser Studie wurden unter Umkehrer et al., A proof-of principal study using phase-contrast imaging for the detection of large airway pathologies after lung transplantation, Scientific Reports (2020) publiziert.
Der Nutzen der Dunkelfeldradiographie zur Erkennung und Diagnose von Lungentumoren wurde bereits in einer vergangenen Studie nachgewiesen. Allerdings beinhaltete diese Studie eine hohe Anzahl an großen Tumorknoten. Im Rahmen dieser Arbeit wird der Vorteil des Dunkelfeld-CT gegenüber der auf zwei Dimensionen limitierten Radiographie gezeigt, da hier das Streusignal in dreidimensionaler Ausbreitung untersucht werden kann. Teile dieser Untersuchungen sind derzeit in Vorbereitung um unter Umkehrer et al., Dark-field CT imaging visualizes micromorphological changes in murine lung tumors veröffentlicht zu werden.

Contents

1 Introduction

1.1 Motivation

Since their groundbreaking discovery by Wilhelm Conrad Röntgen in 1895 [Röntgen, 1896], for which he received the first Nobel Prize in Physics in 1901, X-rays provide a broad range of applications and have become an indispensable part of not only medical imaging, but also other fields such as industrial research.
Since X-rays are able to penetrate most kind of materials, they enable a non-invasive view into the human body, which is used in medical diagnostics to identify injuries such as bone fractures. However, until the introduction of computed tomography (CT) in clinical routine in 1971, permitting diagnostics on three-dimensional volume images and improving the diagnostic value of X-ray imaging tremendously, diagnostics on two-dimensional attenuation-based radiography was the only modality available. Thereby, the contrast of both radiography and CT images exclusively is based on the varying amount of absorption of X-rays caused by differences in density and composition of various types of tissue. Osseous structures with a high content of calcium, for example, differentiate from soft or muscle tissue in X-ray imaging due to its strong absorption. Various types of soft tissue such as inner organs, in contrast, differ only slightly in density and therefore generate hardly any contrast, constraining the diagnosis of even drastic structural and pathological changes.
One possibility to improve the visualization of soft tissue in clinical routine - beside using the already conventional and established techniques such as ultrasound, magnetic resonance imaging (MRI) or positron emission tomography (PET) - is to utilize the wave property of X-rays. In this case, the image contrast is obtained from perturbations in the wavefront caused by a phase-shift imposed when traversing a material. Tissues with low atomic number elemental compositions, such as soft tissue, tend to exhibit stronger differences in phase-shifting ability than in X-ray attenuation. Therefore, phase-sensitive techniques offer an improved soft tissue contrast and additional information compared to the conventional X-ray images. As the refraction angles lie in the range of nano radians, the phase-shift of the wavefront, however, cannot be resolved directly and another approach has to be exploited to access the phase information. In

the past years, various phase-contrast X-ray imaging techniques, providing information about refraction in the sample, have been developed.
A first approach to demonstrate X-ray phase-contrast imaging was reported by Bonse and Hart in 1965 [Bonse, 1965]. By inserting three single-crystals of silicon into the beamline at a synchrotron, the phase changes of coherent and monochromatic X-rays when passing through an object were visualized. The comparison of the interference pattern with and without the object in the beam makes the determination of the phase of the object possible. Equivalent to this method of Bonse and Hart, which relies on Bragg refraction, analyzer-based phase-contrast imaging was introduced in the 1990's where only one analyzer crystal and no reference beam is needed to resolve the phase-gradients of the object. Here, the angle of the analyzer is changed relative to the first crystal offering different planar sections of the distorted wavefront and leading to a series of images in which various features of the object have different contrast [Davis, 1995; Chapman, 1997].
Another approach to visualize the phase contrast uses the free-space propagation of the wavefront to the detector. In contrast to other techniques, this method does not require any additional optical elements in the beam path. However, a detector with small pixel sizes as well as a high beam coherence, which is provided by synchrotron facilities, to resolve the edge-enhancement is needed [Snigirev, 1995; Cloetens, 1999].
With the development of grating-based interferometry, where the so-called Talbot effect [Talbot, 1836] is used to create self-images of the interference pattern after passing the phase grating downstream the beam, a further important step in phase-contrast imaging was realized [Momose, 2003]. An object in the beam modulates the interference pattern and the changes can be resolved by inserting an analyzer grating right in front of the detector [David, 2002; Weitkamp, 2005]. This method does not only provide the differential phase-contrast signal, but also a small-angle scattering information called dark-field signal in analogy to light microscopy. Originally developed at synchrotron facilities, grating-based dark-field and phase-contrast interferometry is one of the most promising approach to bring those additional and complementary contrast information into clinical environment, as it can also be realized using low-brilliance laboratory-based X-ray sources [Pfeiffer, 2006; Pfeiffer, 2007a; Pfeiffer, 2008].
The first step towards the clinical application was done by developing, engineering, and performing experiments with a prototype small-animal phase-contrast and dark-field CT scanner, constructed in collaboration with Bruker microCT (Kontich, Belgium) [Tapfer, 2013]. This scanner features a rotating gantry around a stationary sample, which is a requirement for the acquisition of tomographic scans for *in-vivo* measurements. Within Tapfer's thesis, evaluations of the stability and challenges of a rotating interferometer were investigated, and quantitative images using a calibration phantom were performed. [Velroyen, 2015] mainly dealed with the tasks of overcoming technological setup constraints by algorithmic signal-retrieval corrections and obtaining

higher robustness in the processing of the data acquired with this setup. Furthermore, the first *in-vivo* experiments on mice using 2D radiography as well as CT measurements with this scanner and compatible radiation dose were shown within this work. [Yaroshenko, 2015] focused on the evaluation of the diagnostic value and diagnostic advantages of first relevant applications in medical X-ray dark-field imaging compared to conventional attenuation imaging of living mice for detecting and staging several pulmonary disorders such as chronic obstructive pulmonary diseases (COPD), pulmonary fibrosis, pneumothoraces, and pulmonary carcinoma [Hellbach, 2015; Hellbach, 2017; Hellbach, 2016; Scherer, 2017]. Quite recently, with the development of a large animal dark-field scanner, which poses some major conceptual and technical challenges, a further big step of X-ray dark-field radiography towards clinical application was accomplished. [Gromann, 2017] presented first *in-vivo* dark-field chest images of pigs, serving as a model for the human thorax. As a preliminary stage for the implementation to the clinic, this setup with the large field-of-view (FOV) was also used to perform *in-situ* experiments with deceased human lungs [Willer, 2018]. Finally, a milestone in dark-field radiography was reached by translating this additional contrast information into the clinical environment, dedicated to first *in-vivo* feasibility studies on human lungs.
Even though great achievements could be realized for dark-field imaging and various aspects of the small-animal scanner have been addressed in previous projects, the aim here is to extend the preclinical dark-field research from two-dimensional radiography to three-dimensional computed tomography. In order to do so, the existing prototype dark-field CT scanner must be optimized in order to increase the image quality, while reducing or preserving CT measurement time in order to increase the field to some interesting biomedical applications. For this purpose, some modifications are necessary on the prototype, such as the implementation of a new detector or the new configuration of the existing grating interferometer. Moreover, some questions are if the supplementary and simultaneously generated X-ray phase-contrast signal can also contribute an additional value to medical diagnostics as the dark-field signal? Does the dark-field CT with the improved setup provide clinical benefits for lung tumor diagnostics compared to conventional absorption CT? Is it possible to assess the functionality with respect to gas exchange of the lung in three-dimensional dark-field CT measurements? These and other challenges are addressed in this thesis.

1.2 Outline

This thesis can be divided into different aspects of X-ray dark-field imaging. Chapter 2 provides a theoretical introduction to the essentials of X-rays in general but also the principles behind the grating-based interferometry including phase-contrast and dark-

field imaging, as well as fundamentals of CT reconstruction.
The main part of the thesis can be divided into three chapters. First, Chapter 3 includes an introduction and characterization of the this preclinical phase-contrast and dark-field small-animal CT scanner with respect to tomographic measurements. In detail, the X-ray source, X-ray detector, grating configuration, and the data handling will be explained.
The second topic, described in Chapter 4, focuses on the evaluation of the diagnostic value using *in-vivo* X-ray phase-contrast and dark-field imaging for transplanted murine lungs. The relevance of this project will be motivated in the corresponding chapter.
The final main part of this thesis in Chapter 5 deals with evaluating the diagnostic value of *in-vivo* X-ray dark-field CT measurements with respect to tumor detection as well as lung functionality. Again, an introductory motivation is given at the beginning of the chapter.
Finally, Chapter 6 concludes this work and provides a short outlook for further research.

Theoretical and Experimental Basis 2

Besides an introduction to the fundamental properties of X-rays, this chapter includes the theoretical background of grating-based interferometry using incoherent, lab-based X-ray sources and the principles behind computed tomography. First, the basics of X-rays including the interaction processes with matter, the complex refractive index as well as coherence will be explained. In the following, the fundamentals behind grating-based dark-field and phase-contrast imaging will be introduced, i.e. the Talbot effect, the basic design of a grating interferometer with the phase-stepping and signal extraction, as well as the requirements and restrictions for measuring with incoherent X-ray sources or divergent beams. Finally, the principles of computed tomography, including the Radon transform, Fourier Slice theorem, filtered backprojection, and the more advanced reconstruction algorithm of statistical iterative reconstruction, will be explained. The references mainly used for this chapter are [AlsNielsen, 2011; Paganin, 2006; Kak, 1988; Buzug, 2008; Russo, 2017].

2.1 Definition of X-rays

X-rays (or Röntgen radiation) are a part of high-energy electromagnetic radiation and can be described by two basic models: the classical model and the quantum model. In the classical view, X-rays have a wave-like behavior and are electromagnetic, transverse waves which can be found at short wavelengths around 1 Ångström (10^{-10} m) and are located between ultraviolet and gamma rays. However, the overlap between X-ray and ultraviolet radiation in the lower energetic part and gamma radiation on the higher energetic side of the electromagnetic spectrum is continuous. The electromagnetic spectrum is shown in Figure 2.1.

From a quantum mechanical perspective, X-rays can also be seen as a particles, quantized into photons. In vacuum they are traveling with the speed of light 2.998×10^8 m/s and their energy E is defined by

$$E = \hbar\omega = \frac{hc}{\lambda}, \tag{2.1}$$

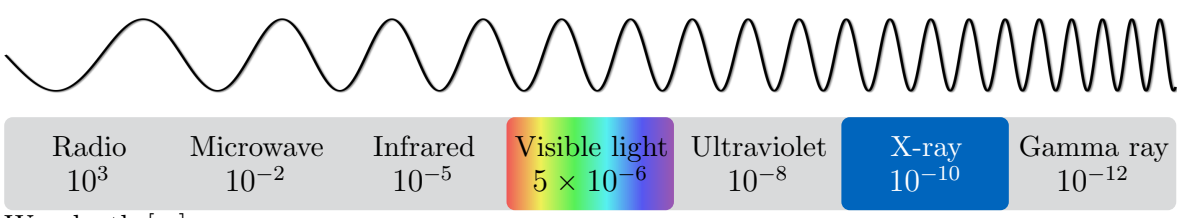

Figure 2.1: Sketch of the electromagnetic spectrum. The continuous electromagnetic spectrum includes wavelengths varying from long-wave radio-waves, used for broadcast radio and television or GPS navigation, to very short-wave gamma radiation. The X-ray spectrum is spread between ultraviolet spectrum and the gamma rays.

with Planck's constant $h = 4.136 \times 10^{-15}$ eVs, wavelength λ and radiation frequency $\omega = 2\pi f$. The typical energy range of X-rays is covering a few 100 eV to several 100 keV, whereas medical imaging typically includes a range from 20 keV to 140 keV. Both the classical, as well as the quantum mechanical view, are important and necessary in order to understand the interaction of X-rays with matter. The quantum mechanical description of X-rays helps to explain the interaction between X-ray photons and electrons of an atom. The classical picture of X-ray leads to the phenomena of refraction and interference. The generation of X-rays will be explained in more detail in Section 2.1.1.

2.1.1 X-ray Generation

In general, there are multiple ways to generate X-rays. Besides the conventional X-ray tube, there are more advanced and sophisticated systems for the generation of X-rays such as the rotating anode tube, the liquid metal jet source, synchrotron sources, or inverse Compton X-ray source systems [AlsNielsen, 2011]. The generation of X-rays will be explained in the following. Historically, the first and also most straightforward approach to generate X-rays is to emit electrons from a heat coil - the cathode - and accelerate those through an applied voltage in kV-range towards a target material - the anode. As sketched in Figure 2.2(A), after penetrating the target material the electrons are decelerated and deflected in the strong electric field near the nuclei and thus emitting X-rays. This so-called *bremsstrahlung* is a continuous spectrum limited by a maximum energy, which is defined by the acceleration voltage U and the electric charge e as $E_{\text{max}} = eU$. If the energy of an incoming electron corresponds to at least the binding energy of an electron of an inner shell, it is capable of releasing it from the shell and ionizing the material. The resulting electron vacancy is filled by an electron of the outer shell, resulting in the emittance of a characteristic radiation due to energy conservation. This characteristic radiation is depending on the target material and su-

perimposes the continuous spectrum of the bremsstrahlung. A typical X-ray spectrum can be seen in Figure 2.2(B).
The main advantage of conventional X-ray sources is that they provide a cost-effective

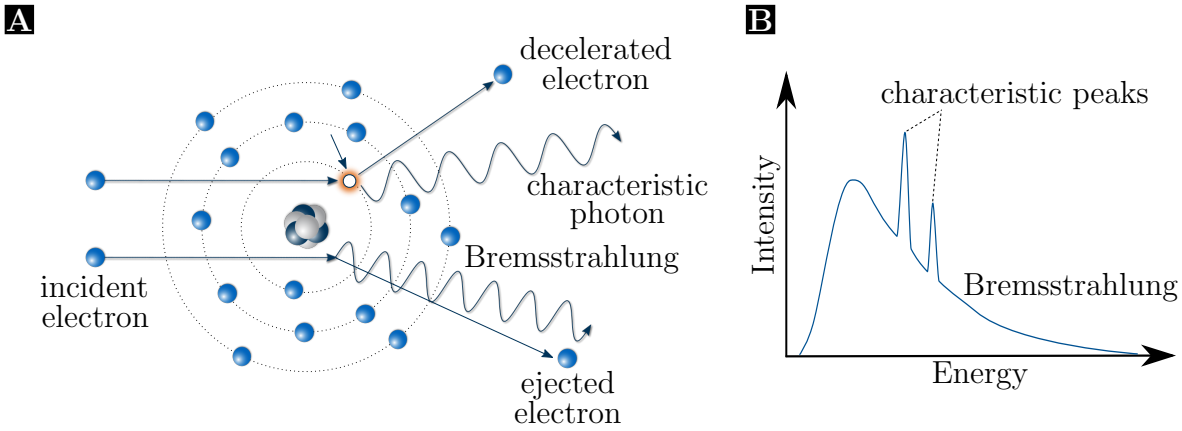

Figure 2.2: Generation of X-rays. Electrons, emitted from the cathode, are accelerated towards the anode by applying high voltage. In the anode, the incoming electron interacts with electrons from the target material (A) which finally results in the spectrum consisting of *bremsstrahlung* and characteristic peaks (B).

and compact way for the generation of X-rays, especially within the clinical environment. Hence, X-ray tubes are widely used in both non-destructive testing and imaging. The flux provided by an X-ray tube is, however, comparable low as the cooling capacity of the target material is limited. In order to overcome this issue, either a rotating anode, which dissipates the induced heat over a larger area, or a liquid metal jet source, where the target consists of a metal alloy based on indium and gallium, can be used [Hemberg, 2003].
A spectrum which is more brilliant and tuneable to the optimal wavelength for the experiment is provided at a synchrotron facility. The brilliance is thereby a figure of merit and describes the quantities of the photon flux, the beam divergence, and the energy bandwidth of a radiation. In particle physics, synchrotron radiation was regarded as an undesired side-effect, since an acceleration of charged particles in the magnetic field of the bending magnets results in a loss of energy. In newer synchrotron generations, special inserted devices with a periodic arrays of magnets, such as wigglers or undulators, force the electrons to follow an oscillating path, generating highly brilliant synchrotron radiation. However, synchrotrons with several hundred of meters in diameter are very maintenance-intensive and expensive. Therefore, efforts on inverse Compton X-ray sources, combining the benefits from the high brilliance of synchrotron radiation with the advantages of conventional X-ray sources such as compactness, and lower costs, have been made. For the generation of X-rays, inverse Compton X-ray

sources make use of the phenoma of the inverse Compton effect: Electrons with relativistic energies stored in a storage ring collide with a highly focused laser beam. As a result, the electrons transfer a part of their energy to the laser beam, shifting the electromagnetic radiation of the laser beam into the X-ray regime. For more details, the reader is referred to read [Eggl, 2016; Eggl, 2017; Jud, 2018].

2.1.2 Detection of X-rays

In general, there are multiple detector system for the detection of X-rays. According to Paganin [Paganin, 2006], X-ray detectors can be classified into two major types: integrating detectors and photon-counting detectors. Both will be introduced in the following.

Types of X-ray Detectors

Integrating Detectors

The first example of an integrating detector is the analog X-ray film. Since X-ray films are not very sensitive to X-rays per se, an intensifying screen is used to convert the information contained in the X-ray beam into light photons, which finally expose the emulsion layer of the film with a significantly increased intensity. The emulsion layer contains silver halide crystals, typically primarily silver bromide, which decompose when exposed to X-rays. In the development process the contained information appears through blackening of the reduced metallic silver [Martin, 2006]. X-ray films benefit from several properties such as a high dynamic range combined with a high sensitivity, or large areas combined with low costs. Nevertheless, the utilization of an X-ray film implies the limitation to 2D radiographies, the necessity of digitizing the images, and the degradation with age [Paganin, 2006].
In the meantime, however, analog X-ray films have been replaced by digital detectors in most areas of research and medical imaging. Examples for modern digital integrating detectors are charge coupled device (CCD) or flat panel detectors. The principle behind flat panel detectors is an indirect detection of X-rays based on conversion and detection. Incoming X-rays are converted in the scintillator layer by the absorption of the X-ray and emitting low-energetic photons in the visible light regime via relaxation processes. The scintillator layer is optically coupled to a pixelized matrix of photo diodes combined with a transistor. In the photo diodes the visible light is converted into an electrical signal and charge is produced in the form of electron-hole pairs. The charge is collected and integrated pixel-wise over the exposure time and finally converted and read-out into a digital signal using a transistor, such as CMOS or TFT. In

comparison, CCD detectors are based on semi-conductors, where the transformation of X-ray photons to visible light is not necessary, and each pixel collects electron charge proportional to the amount of photons passing through.
Equivalent to analog X-ray films, digital integration detectors benefit from an excellent linearity over a moderate dynamic range and a high spatial resolution. But, those detectors suffer from slow readout times and dark-current noise. Moreover, as the amount of charge created is integrated over the exposure time, no information about individual photon energies can be provided using this technology. Nevertheless, integrating detectors are widely used as they can be produced with large field of views and can reach high quantum efficiencies.

Counting Detectors

Counting detectors (or single-photon counting detectors) are able to convert individual X-ray photons directly to an electric signal, which finally results in a significantly higher amount of charge per photon compared to detectors using conversion mechanisms [Ehn, 2017]. Beside the great dynamic range and the box-like point-spread-function (PSF) of counting detectors, they offer an energy discrimination and the implementation of energy thresholds which finally results to the absence of dark current and electronic noise during the data acquisition. Nevertheless, counting detectors offer a limited spatial resolution and a comparably low efficiency sensor material [Paganin, 2006].

Characterization of Imaging Devices

This section introduces the mathematical functions which are used for the characterization and for the quantification of the detector system's quality. This introduction is based on the linear system theory and describes in particular the spatial resolution. For this purpose, the concepts of describing the response of an imaging system is explained, i.e. point-spread function (PSF), line-spread function (LSF), and edge-spread function (ESF). For a more detailed discussion of this topic, the reader is referred to the textbooks [Behling, 2015; Boreman, 2001; Buzug, 2008; Russo, 2017]. In this section, those quantities are introduced with focus on the particular case of a linear and shift invariant system described by real response functions. This represents the experimental setup used for the image acquisition in this work. An optical imaging system is considered to be linear, which implies that the principle of superposition is valid. That means that a linear combination of individual input signals $i_i(x, y)$ (in this case a 2D representation of the object) is described by a linear combination of the

individual impulse-response output signals $o_i(x, y)$ (acquired 2D image) as

$$S\{i_1(x,y) + i_2(x,y)\} = S\{i_1(x,y)\} + S\{i_2(x,y)\} \tag{2.2}$$
$$= o_1(x,y) + o_2(x,y) \tag{2.3}$$

and

$$S\{ai_i(x,y)\} = aS\{i_i(x,y)\}, \tag{2.4}$$

where $S\{\ \}$ describes the transfer characteristic, and a is any real constant. Moreover, in order to refer to an imaging system as linear translation invariant, the condition of shift-invariance has to be fulfilled. This means that a shift in the position of the input signal causes only a shift in the position of the output signal according to

$$S\{i(x - x', y - y')\} = o(x - x', y - y'). \tag{2.5}$$

Point-Spread Function

The derivation of the PSF requires the consideration of a linear translation invariant system as well as a delta-peak shaped input impulse. With a test function $\phi(x', y')$, this input signal is assumed to be a Dirac Delta distribution $\delta(x, y)$, whose main property is defined by

$$\int_{\mathbb{R}} \delta(x,y)\mathrm{d}x\mathrm{d}y = 1, \tag{2.6}$$

and leads to

$$\int_{\mathbb{R}} \delta(x - x', y - y')\phi(x', y')\mathrm{d}x'\mathrm{d}y' = \phi(x, y). \tag{2.7}$$

The response of the system is defined as

$$S\{\delta(x - x', y - y')\} = \mathrm{PSF}(x - x', y - y'), \tag{2.8}$$

and characterizes the resolution of an imaging device. It describes the measured signal distribution and the blurring induced during the image formation process of the system. In order to guarantee that the convolution does not affect the integral intensity in the image, the PSF is normalized to one

$$\iint_{\mathbb{R}^2} \mathrm{PSF}(x,y)\mathrm{d}x\mathrm{d}y = 1. \tag{2.9}$$

Consequently, the output signal of the imaging system can be described as

$$o(x, y) = \mathrm{PSF}(x, y) \otimes i(x, y). \tag{2.10}$$

For a series of several optical elements, such as the source, the gratings, or the detector in the case of the work presented here, the PSF of an imaging system results in a convolution of the respective PSF of the optical element i and results in

$$\mathrm{PSF}_{\mathrm{system}} = \mathrm{PSF}_{\mathrm{source}} \otimes \mathrm{PSF}_{\mathrm{gratings}} \otimes \mathrm{PSF}_{\mathrm{detector}}. \tag{2.11}$$

Line-Spread Function

Analog to a point-like input signal, the LSF describes the response of the imaging system to a line-shaped input signal of infinitesimal width. In the following, we consider a line-shaped object σ_{L} along the y-axis as

$$\sigma_{\mathrm{L}}(x, y) = \delta(x). \tag{2.12}$$

The LSF is defined by the convolution of the measured object with the PSF of the imaging system and results in

$$\mathrm{LSF}(x) = o_{\mathrm{L}}(x, y) = i_{\mathrm{L}}(x, y) \otimes \mathrm{PSF}(x, y) \tag{2.13}$$

$$= \iint_{-\infty}^{\infty} \mathrm{PSF}(x - x', y - y')\delta(x')\mathrm{d}x'\mathrm{d}y' \tag{2.14}$$

$$= \int_{-\infty}^{\infty} \mathrm{PSF}(x, y')dy'. \tag{2.15}$$

As one can see in Eq. 2.15, a projection of the PSF along the y-axis is equal to the LSF in x-direction.

Edge-Spread Function

Finally, the ESF describes the detector response to an edge-shaped function σ_E, which is considered to be parallel to the y-axis and can be defined by

$$\sigma_E(x, y) = \sigma_E(x) = \begin{cases} 0, & \text{for } x < 0, \\ 1, & \text{otherwise.} \end{cases} \tag{2.16}$$

Similar to the LSF, the ESF is given by the convolution of the edge-shaped object with the PSF as

$$\mathrm{ESF}(x) = o_{\mathrm{E}}(x, y) = i_{\mathrm{E}}(x, y) \otimes \mathrm{PSF}(x, y) \tag{2.17}$$

$$= \iint_{-\infty}^{\infty} \mathrm{PSF}(x - x', y - y')i_{\mathrm{E}}(x')\mathrm{d}x'\mathrm{d}y', \tag{2.18}$$

and with inserting the relation from Eq. 2.15, the ESF results in

$$\mathrm{ESF}(x) = \int_{\infty}^{\infty} \mathrm{LSF}(x') * i_{\mathrm{E}}(x - x')\mathrm{d}x', \tag{2.19}$$

where $*$ denotes a one-dimensional convolution. The derivative of a convolution product from two functions can be rewritten as the result of a convolution of one of the two functions with the derivative of the other. Consequently, the derivative of $\mathrm{ESF}(x)$ results in

$$\frac{\mathrm{d}}{\mathrm{d}x}\mathrm{ESF}(x) = \frac{\mathrm{d}}{\mathrm{d}x}[i_E(x) * \mathrm{LSF}(x)] = \delta(x) * \mathrm{LSF}(x) = \mathrm{LSF}(x). \tag{2.20}$$

2.1.3 X-ray Interactions with Matter

This section introduces the fundamental interaction processes of X-rays with matter. In the present energy range, X-rays interact mainly with electrons. On an atomic level, the interaction between an X-ray photon and matter takes place in two ways: they are absorbed photoelectrically or scattered. Figure 2.3 illustrates the basic interaction processes for X-rays with matter which will be explained in the following: Photoelectric absorption (A), elastic scattering (B), and inelastic (Compton) scattering (C). Though, there are additional interaction processes which are neglected in this description as they are not relevant at the present energy range: X-ray fluorescence, emission of Auger electrons, and pair production.

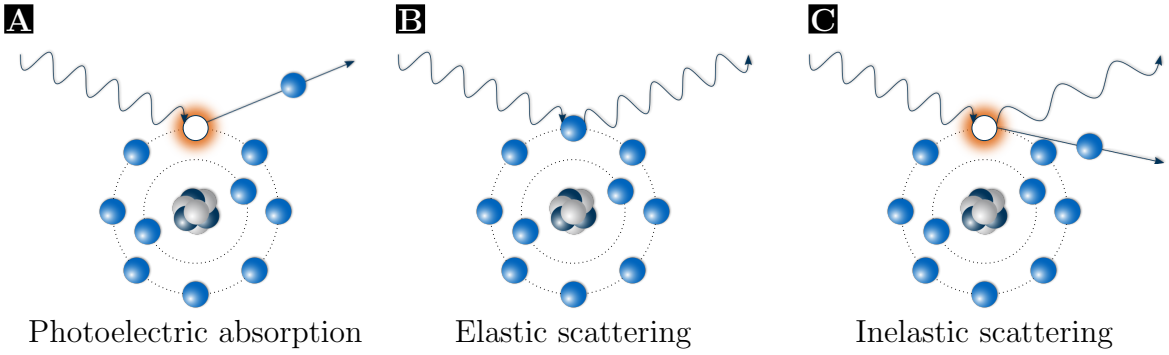

Figure 2.3: Interaction processes of X-rays with matter. A) An incoming X-ray photon is absorbed completely by an electron. B) The incoming X-ray photon scatters with an electron without energy transfer, i.e. no change in wavelength. C) The incoming photon interacts with an electron and transfers a part of its energy to the electron which results in a changed wavelength for the photon.

Photoelectric Effect

One main absorption process is the photoelectric effect. If the energy of the incoming X-ray photon is larger than the binding energy of an electron in an atomic shell, the photon can be completely absorbed, transferring all its energy to the electron which gets ejected from the atom. With an increasing photon energy, more electrons can be expelled instantaneously from one of the less tightly bound (outer) shells. These thresholds are called absorption edges. The hole in the electron configuration can be closed by an electron from a higher shell which emits a fluorescence photon or the excess energy can directly eject an additional electron which is called Auger electron. The cross section (and therefore the probability) of the photoelectric absorption $\sigma_{\mathrm{ph}}(E, Z)$ can be approximated as

$$\sigma_{\mathrm{ph}}(E, Z) \propto Z^{4-5} E^{-3}, \tag{2.21}$$

where Z is the atomic number and E the energy of the photon [White, 1977].

Elastic Scattering

For wavelengths of the X-ray photon being much larger than the diameter d of the object

$$\lambda \gg d \tag{2.22}$$

elastic scattering, which is also known as Rayleigh or Thomson scattering, may occur. Elastic scattering is a scatter process where the directions of the incident and scattered X-ray photons are different, but the wavelength and the momentum are equal. Therefore, the energy of the incident photon and the scattered photon remains unchanged [Buzug, 2008]. The differential cross-section for the Thomson scattering is given by

$$\sigma_{\mathrm{coh,e}} = \frac{8\pi}{3} r_0^2, \tag{2.23}$$

where $r_0 = 2.82 \cdot 10^{-15}\,\mathrm{m}$ is the classical electron radius.

Inelastic Scattering

Inelastic scattering, which is also known as Compton scattering, describes the scattering process in which the incident photon transfers kinetic energy to an electron, resulting in a shorter wavelength for the outgoing photon and an ejected electron. The change in wavelength $\Delta\lambda$ can be described as [AlsNielsen, 2011]

$$\Delta\lambda = \lambda_{\mathrm{c}}(1 - \cos\theta), \tag{2.24}$$

where $\lambda_c = h/m_e c$ is the Compton wavelength, θ denotes the angle between the incident and scattered photon, and m_e is the electron mass. The cross section of the Compton scattering can be approximated by the Klein-Nishina equation and depends roughly only on the atomic number

$$\sigma_{\text{incoh}} \propto Z. \tag{2.25}$$

2.1.4 Complex Refractive Index

Since X-rays are electromagnetic waves, interaction phenomena such as reflection, refraction, and absorption at interfaces between different media are expected on a more macroscopic level. In order to describe those effects, the media of interest are considered to be homogeneous with sharp boundaries, each matter having its own refractive index n. In general, the complex refractive index can be expressed as

$$n = 1 - \delta + i\beta, \tag{2.26}$$

where the parameter δ is called the refractive index decrement and the imaginary part β is related to the absorption and is called the absorption index. Both parameters depend on the energy of the radiation and the material of the respective media. An ideal electromagnetic wave propagating in z-direction within vacuum, with no polarization and no change in propagation direction, can be described as

$$\Psi(\vec{r}, t) = \Psi_0 e^{i(\vec{k}\cdot\vec{r}-\omega t)} = \Psi_0 e^{i(kz-\omega t)}, \tag{2.27}$$

with Ψ_0 denoting the wave's amplitude, $\vec{k}$ is the wave vector with $|\vec{k}| = \frac{2\pi}{\lambda}$, and ω is the angular frequency which is defined by the energy $E = \hbar\omega$. If the wavefront penetrates a medium with complex refractive index n, the wave vector k changes to kn. With Eq. 2.26, the wave propagation consequently results in

$$\Psi(z, t) = \Psi_0 \cdot e^{i(nkz-\omega t)} = \Psi_0 \underbrace{e^{i(kz-\omega t)}}_{\text{propagation}} \cdot \underbrace{e^{-\beta kz}}_{\text{attenuation}} \cdot \underbrace{e^{-i\delta kz}}_{\text{phase shift}}, \tag{2.28}$$

where the first term describes the unperturbed wave propagation, the second term the attenuation of the initial wave, and the last term describes the phase shift. The wave propagation is schematically depicted in Figure 2.4.

Attenuation and Beer-Lambert Law

When X-rays are passing through matter, the amplitude of the initial wave is reduced and the phase is shifted, as indicated in Eq. 2.28. The amplitude is related to the attenuation of X-rays by the object, which is an experimental quantity that can be

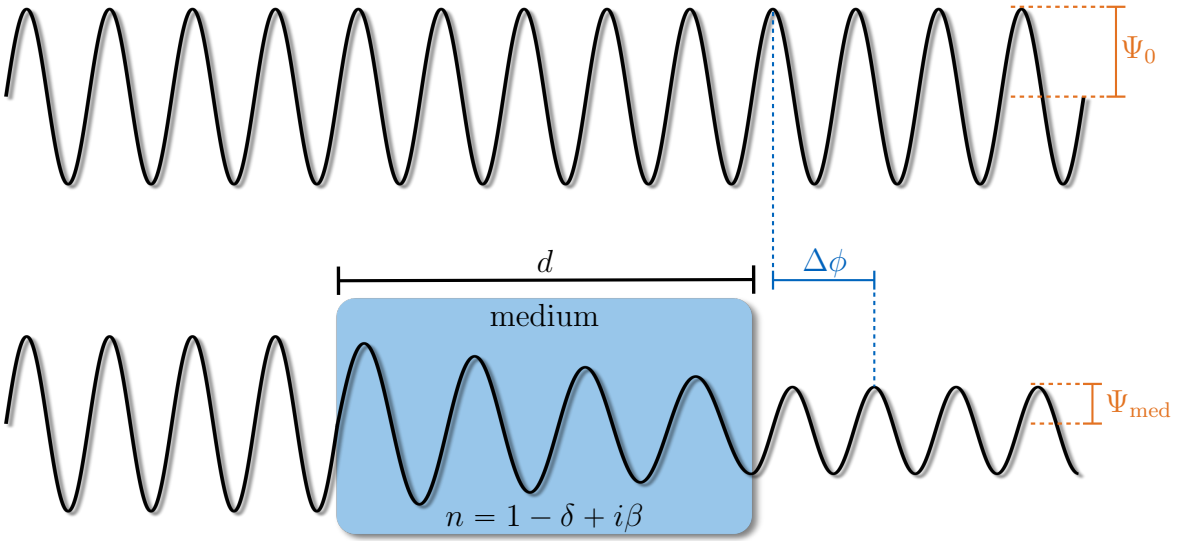

Figure 2.4: Illustration of attenuation and phase shift pf an electromagnetic wave. Monochromatic wave passing through vacuum (upper part) and through a medium of refractive index n (lower part). In comparison to the undisturbed wave in the vacuum, the object induces a phase shift $\Delta\phi$ and the amplitude decreases from Ψ_0 to Ψ_{med}.

measured directly. The ratio of the beam intensities before (I_0) and after passing a medium ($I(z)$) results in

$$\frac{I(z)}{I_0} = \frac{|\Psi_0 \cdot e^{i(kz-\omega t)} \cdot e^{-\beta kz} \cdot e^{-i\delta kz}|^2}{|\Psi_0 \cdot e^{i(kz-\omega t)}|^2} = e^{-2\beta kz}. \tag{2.29}$$

This exponential expression is known as the Beer-Lambert law, which describes the attenuation of an X-ray beam with initial intensity I_0 and linear attenuation coefficient μ via the exponential law as

$$\frac{I(z)}{I_0} = e^{-\mu z}, \tag{2.30}$$

where the known attenuation coefficient is defined as

$$\mu = 2k\beta = \frac{4\pi}{\lambda}\beta. \tag{2.31}$$

When dealing with a polychromatic X-ray source and an heterogeneous object, the Beer-Lambert law can be generalized to

$$I(z) = \int_{E_{\text{min}}}^{E_{\text{max}}} I_0(E) e^{-\int_0^z \mu(E,Z,z')\mathrm{d}z'} \mathrm{d}E, \tag{2.32}$$

where $\mu(E, Z, z')$ is the energy and material or rather atomic number Z dependent attenuation coefficient. Furthermore, the total attenuation coefficient relates to the scattering cross section $\sigma_{\text{tot}}(E, Z)$ as

$$\mu(E, Z) = \rho \frac{N_A}{A} \sigma_{\text{tot}}(E, Z), \tag{2.33}$$

where ρ is the mass density, N_A is the Avogadro's constant, and A is the atomic mass number. In the case of molecules with N atoms, the total energy-dependent attenuation coefficient results in

$$\mu(E) = \sum_{i}^{N} w_i \mu_i(E), \tag{2.34}$$

where w_i is the mass fraction of atom i and $\mu_i(E)$ is the respective attenuation coefficient.

X-ray phase-shift

In addition to the decreased amplitude, when a wave is passing through an object with a refractive index n, a phase shift $\Delta\phi$ with respect to the unperturbed wave in vacuum is induced and can be described related to Equation 2.28 as

$$\Delta\phi = k\delta z. \tag{2.35}$$

X-rays traversing through a medium with $\Delta\phi \neq 0$ are refracted. If the incoming wavefront is a plane wave, the wavefront after the object is slightly deflected by the angle α which is in the order of micro-radians. Furthermore, α is connected to the first derivative of the wavefront profile in the diffraction direction x by

$$\tan\alpha = \frac{\lambda}{2\pi} \frac{\partial\phi}{\partial x}. \tag{2.36}$$

Similar to the case of attenuation, we can extend the phase-shift to a more general case in a homogeneous material as

$$\Delta\phi = \int_{0}^{z} k\delta(E, z')\mathrm{d}z'. \tag{2.37}$$

2.1.5 Coherence

The derived refraction angle and absorption in the previous section are based on the assumption that the beam is monochromatic and point-like, and therefore in a perfect

plane wave state which can be fully determined. However, in reality the waves never propagate all in the same direction in space with the same wavelength. In order to extract the phase-contrast information with polychromatic radiation and extended source sizes of laboratory X-ray sources, coherence requirements have to be fulfilled. In the following, the concepts of transverse (spatial) and longitudinal (temporal) coherence are introduced.

Longitudinal coherence requirements

In Figure 2.5(A), two plane waves propagating in exactly the same direction but with slightly different wavelengths, λ and $\lambda - \Delta\lambda$ respectively, are shown. The vertical lines indicate the maxima of the respective wavefront. The overlap and the respective sine indicate that the two waves are exactly in phase at the beginning and consequently they are out of phase with a π-shift after travelling a certain distance. This distance defines the longitudinal coherence length L_L. Consequently, they will have the same phase again after travelling the distance $2L_L$ resulting in

$$2L_{\mathrm{L}} = N\lambda = (N+1)(\lambda - \Delta\lambda). \tag{2.38}$$

By converting the relation from Eq. 2.38 to $(N+1)\Delta\lambda = \lambda$, or $N \approx \lambda/\Delta\lambda$ the longitudinal coherence length can be expressed as

$$L_{\mathrm{L}} = \frac{1}{2}\frac{\lambda^2}{\Delta\lambda}. \tag{2.39}$$

Longitudinal coherence is required when working with polychromatic X-ray sources that emit radiation within a certain bandwidth. For a correlation length beneath the wavelength, phase-related phenomena are no longer visible [Russo, 2017].

Transverse coherence requirements

The second scenario needing consideration is the case when two waves have the same wavelength λ, but the directions of propagation diverge slightly by an angle of $\Delta\theta$. This case is depicted in Figure 2.5(B). Both wavefronts coincident at the points marked with the circles, whereas they are out of phase at half distance between those points. The distance between in-phase and out-phase wavefront is referred to as transverse coherence length L_{T}. For sufficiently small inclination angles $\Delta\theta$ between both wavefronts, the transverse coherence length is given by $2L_{\mathrm{T}}\Delta\theta = \lambda$. The angle can be approximated with the lateral extent D and distance R by $\Delta\theta \approx D/R$ resulting in a transverse coherence length of

$$L_{\mathrm{T}} = \frac{\lambda}{2\tan\Delta\theta} = \frac{\lambda R}{2D}. \tag{2.40}$$

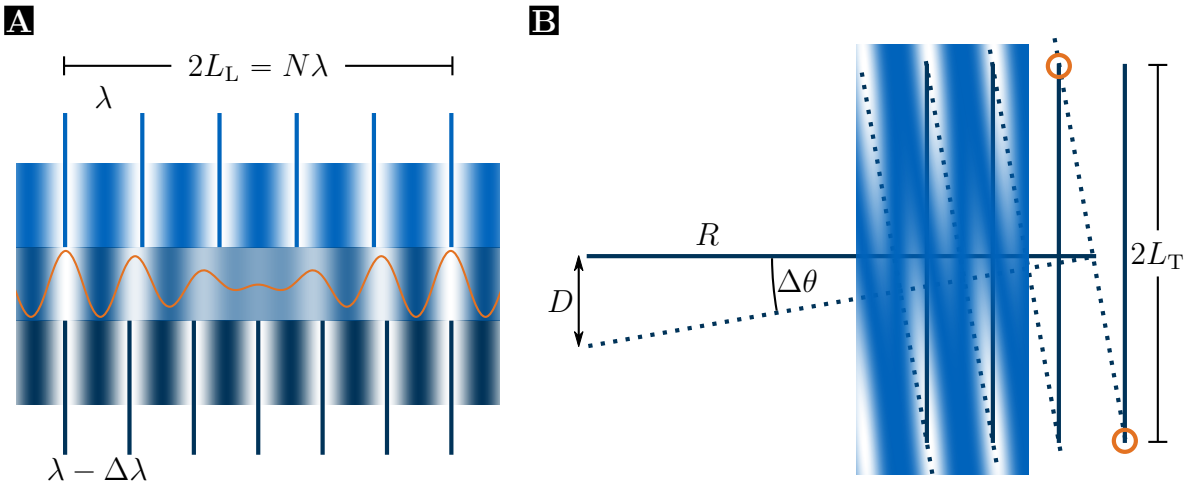

Figure 2.5: Longitudinal and transverse coherence lengths. (A) Two waves with two different wavelengths, λ and $\lambda - \Delta\lambda$, propagating in identical direction. After travelling the longitudinal coherence length L_L, the waves are completely out of phase. The longitudinal coherence length is determined by the monochromaticity of the source. (B) Two waves with an identical wavelength propagating from the ends of a finite sized source of width D, resulting in an angle θ between those waves. The waves are out of phase by a factor of π at transverse coherence length L_T, whereas they coincidence at doubled transverse coherence length marked with the orange circles.

Using this relation, it is clear that the transverse coherence length scale does not only depend on the wavelength but also on the ratio between propagation distance and lateral source size D.

2.2 Grating-Based Interferometry

In the field of visible light microscopy, there are a number of techniques to enhance the contrast properties of the specimen or to obtain additional information. Optical elements of the microscope allow to retrieve phase-contrast or dark-field images. In contrast, in the field of X-rays the use of phase information to resolve various biological soft tissues in the body is challenging as the development of X-ray optics is very demanding. In the last few decades, different approaches to obtain phase-contrast information have been reported. Those methods are based on a crystal interferometer [Bonse, 1965; Momose, 2003], free-space propagation [Snigirev, 1995; Wilkins, 1996; Cloetens, 1999], or various types of analyzers [Davis, 1995; Ingal, 1995]. Those techniques demand for a high spatial coherence, or require the high flux of a synchrotron source. The most promising method in order to introduce phase-contrast and dark-field

imaging using a low-brilliance lab-based X-ray source, enabling a wide use especially for medical applications in future, is the three grating interferometer [David, 2002; Weitkamp, 2005; Pfeiffer, 2007a]. As this approach was used to obtain the results presented in this thesis, and to permit a brief overview, this method will be introduced in the following in more detail.

2.2.1 Talbot Effect

The Talbot effect, introduced in 1836 by Henry Fox Talbot [Talbot, 1836], is essential for the operation of a grating interferometer. Talbot discovered that when a coherent wavefront of visible light illuminates a periodic object, a self image of the object is produced at multiple distances. The Talbot effect can be observed, as shown in Figure 2.6, in the propagation of a monochromatic wavefront through e.g. a grating. This periodic object reappears at Talbot distance d_{T} from an absorbing object

$$d_{\mathrm{T}} = \frac{2p^2}{\lambda} \tag{2.41}$$

and multiple integers m

$$d = m d_{\mathrm{T}} \tag{2.42}$$

of it, where p is the period of the grating and λ denotes the wavelength of the light ($\lambda \ll p$). A simulated Talbot carpet for an absorption grating with duty cycle of 0.5 is depicted in Figure 2.6(A). However, also a phase-shifting grating, where the phase of the wavefront is alternated instead of attenuating its intensity, can be used in order to create this effect. This does not result in an immediate change of the wave amplitude, but is converted into an intensity modulation downstream the propagation distance, resulting in intensity modulations for so-called fractional Talbot distances. In contrast to the full Talbot distance, which is only depending on the wavelength of the X-rays and the periodicity of the grating, the fractional Talbot distances also depend on other properties. This is illustrated for a π- and a $\frac{\pi}{2}$-shifting grating in Figure 2.6(B) and Figure 2.6(C), respectively. For the attenuation grating, the wavefront intensity repeats itself at half and full Talbot distance, [Talbot, 1836; Rayleigh, 1881; Cloetens, 1999], whereas the phase-shifting gratings also induce similar interference patterns at the fractional Talbot distances. The fractional Talbot distances are marked with the dashed lines and were determined to occur at

$$d_{\mathrm{T,f}} = m\eta\frac{2p^2}{\lambda}, \tag{2.43}$$

where $m = 1, 3, 5, ...$ is the order of the fractional Talbot distance and the magnitude of the phase-shift η being

$$\eta = \begin{cases} \frac{m}{4} & \text{for a } \frac{\pi}{2}\text{-phase grating,} \\ \frac{m}{16} & \text{for a } \pi\text{-phase grating.} \end{cases} \tag{2.44}$$

Consequently, an ideal $\frac{\pi}{2}$-phase-shifting grating has maximum intensity modulation at $\frac{1}{4}d_{\mathrm{T}}$ and $\frac{3}{4}d_{\mathrm{T}}$, whereas a π-phase-shifting grating induces multiple intensity modulation at $\frac{m}{16}d_{\mathrm{T}}$. The periodicity of the interference pattern behind the grating also depends on the induced phase shift. While absorption and $\frac{\pi}{2}$-phase grating have the same period, the period of the interference pattern of a π-shifting grating is halved.

2.2.2 X-ray Grating Interferometer

In order to realize X-ray phase-contrast measurements, a grating interferometer utilizes the Talbot effect as described above. Initially introduced at a synchrotron facility, two gratings (phase grating G_1 and analyzer grating G_2) are placed into the beam [David, 2002]. The wavefront is diffracted by the phase grating G_1 into distinct orders at different directions leading to interference and overlap of the individual beams. After propagating the Talbot distance, the distorted wavefront repeats itself. Since the detector pixels are much larger than the grating period, those perturbations cannot be resolved directly. An analyzer grating G_2 is therefore required and typically placed close to the detector. This grating serves as an analyzer and makes the refracting, scattering and attenuating effects of the sample resolvable. In order to fulfill the requirement of the spatial coherence, an additional grating G_0 upstream the beam is necessary when working with a conventional, low-brilliance lab source [Pfeiffer, 2006; Pfeiffer, 2007a; Pfeiffer, 2008]. This additional grating is called source grating and it divides the initial beam into an array of smaller sources, leading to an increased effective spatial coherence of the X-ray wavefront.
A scheme of a Talbot-Lau interferometer for a polychromatic X-ray source and the effects of different interactions processes are visualized in Figure 2.7. As mentioned before, a sample in the X-ray beam affects the interference pattern due to attenuation, refraction, and scattering. If the X-ray wavefront is purely attenuated by an object, this results in a reduced flux on G_2 and, hence, in a decreased intensity recorded at the detector as indicated in Figure 2.7(A). On the other hand, if a purely refracting object illustrated by way of example with a wedge in Figure 2.7(B) is present in the beam, the X-ray beam gets refracted. This results in a laterally shifted interference pattern, whereas the amplitude and the intensity of the sinusoidal are not affected. Finally, if we deal with a sample which does not absorb but scatters the beam uniformly in all directions, a diffuse scattering is registered. This diffuse scattering destroy the

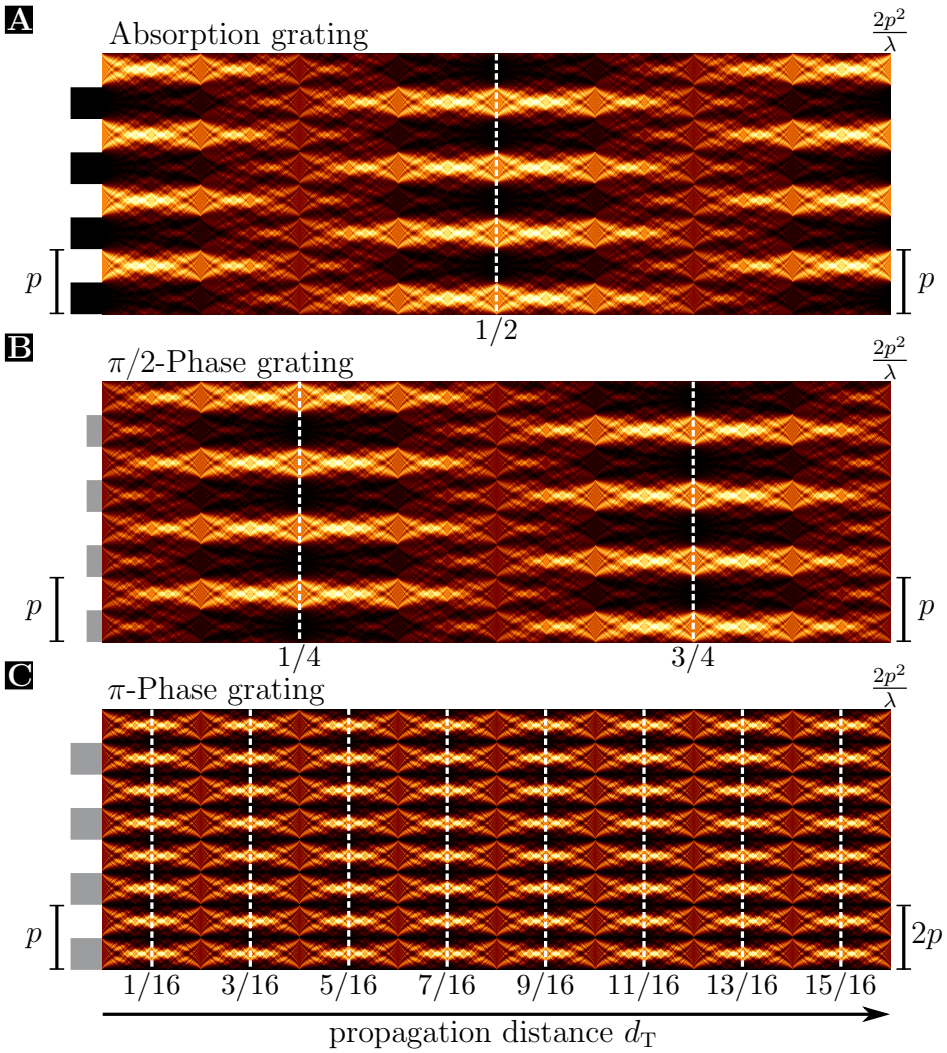

Figure 2.6: Talbot carpet of three different types of gratings. An absorption grating (A), a $\pi/2$-shifting phase grating (B), and a π-shifting phase grating (C) are illustrated for a full Talbot distance d_T using a monochromatic parallel beam geometry.

coherence and thus reduce the visibility. However, in experimental reality each object shows a combination of all three discussed properties.

2.2.3 Phase-Stepping and Image Extraction

To reveal the small deviations in the interference pattern induced by the sample in the beam, it is necessary to move one of the gratings perpendicular to the beam direction over one full grating period in a number of steps and record an image for each posi-

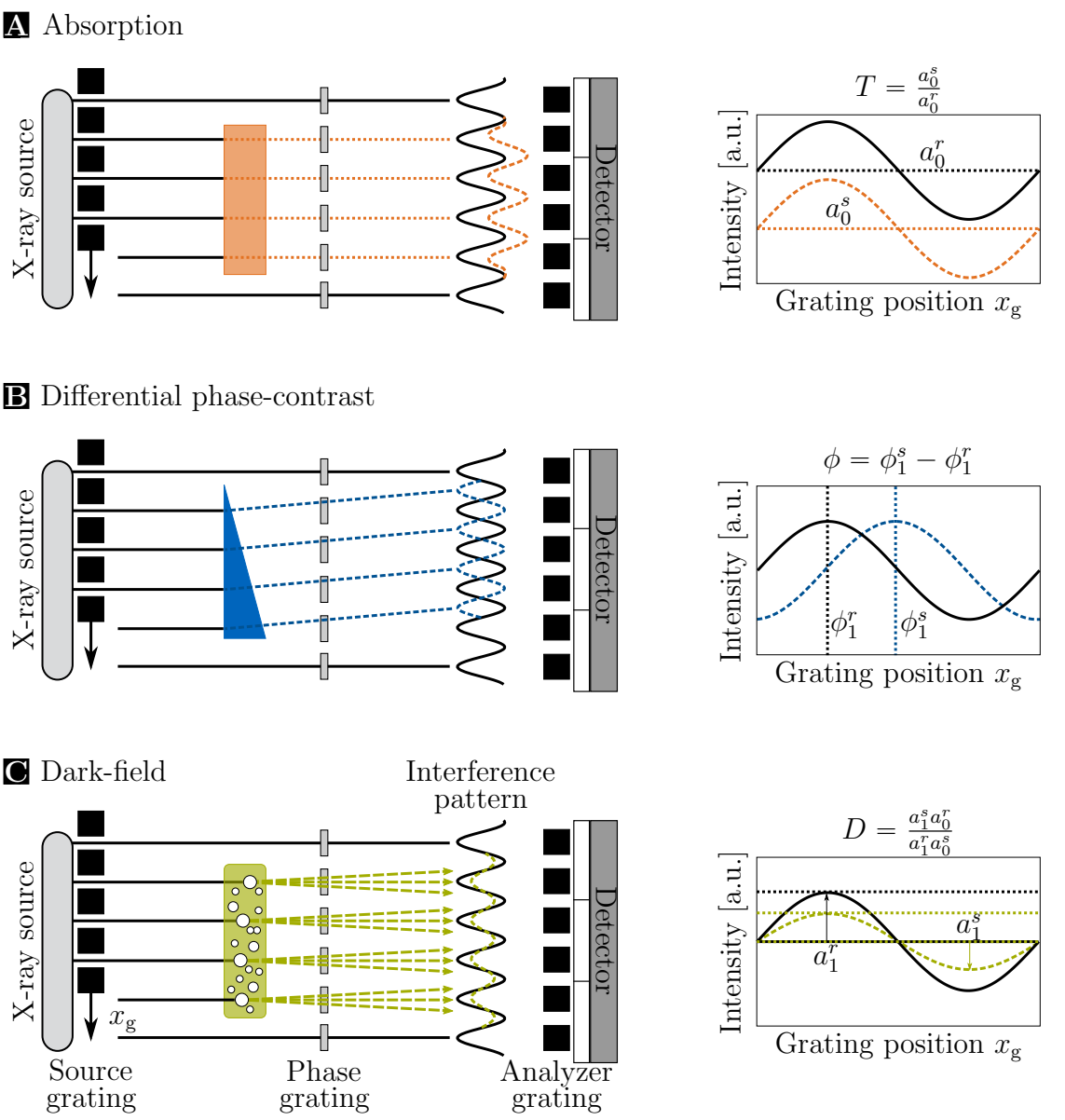

Figure 2.7: Working principle of a Talbot-Lau interferometer. (A) The absorption of X-rays of a purely attenuating object leads to a reduction of the mean intensity a_0 measured at the detector. (B) The lateral phase-shift φ of the interference pattern is caused by the refraction of an object, resulting in the phase-contrast signal. (C) Multiple scattering within an object reduces the amplitude a_1 of the interference pattern, leading to a destruction of coherence. This is referred to as dark-field signal. Figure partly adapted from [Birnbacher, 2018].

tion [Weitkamp, 2005]. In principle, it is irrelevant which grating is moved. From the convolution of the interference pattern and the transmission function of the analyzer

grating, the measured intensity in each pixel can be calculated as a function of the relative grating position, which is referred to as the "(phase-)stepping curve".
In an ideal case, the phase grating is illuminated with a coherent plane wave, resulting in a square wave from G_1 passing across the square-like structure of G_2, which consequently results in a triangular wavefront as a result of the convolution of two square waves. However, due to finite coherence, the spatially extended X-ray source, and the source blurring the observed shape in the experiments can be approximated by a sinusoidal curve. Please note that the typical pixel size of the detector is at least one order of magnitude lager than the period of the gratings, which finally leads to a measured intensity as the sum over several grating periods covering the detector.
In order to extract all three signals (attenuation, refraction, and scattering) from the stepping curve, various approaches exist. One of the fastest and simplest approach, however, is based on the description using a Fourier-series and Fourier decomposition. The intensity measured in each pixel for M phase steps in dependency of the grating position x_g can be described by

$$I(x, y, x_\mathrm{g}) = \sum_{i}^{M} a_i(x, y) \sin(2\pi i \frac{x_\mathrm{g}}{p} - \varphi_i(x, y)), \tag{2.45}$$

with a_i and φ_i being the amplitude and phase-coefficients, respectively. Assuming moderate coherence and a visibility below 50%, the Fourier series can be well approximated by neglecting all terms after the first order [Bech, 2009] to

$$I(x, y, x_\mathrm{g}) = a_0(x, y) + a_1(x, y) \sin(2\pi \frac{x_\mathrm{g}}{p} + \varphi_1(x, y)). \tag{2.46}$$

Thereby, the coefficient a_0 represents the average measured intensity, a_1 denotes the oscillation amplitude, and φ_1 is the phase shift of the interference pattern. Those parameters can be extracted from the fitted sine curve to the measured intensities.
In order to calculate the effect of the sample to the individual signals, it is mandatory to record a reference measurement, i.e. a stepping curve detected without the presence of the object in the beam. In the following values with superscript r and s represent the parameters calculated for the reference and sample scans, respectively. In Figure 2.8, the phase-retrieval process of an exemplary set is illustrated for reference and sample scans, acquired with the setup which will be introduced in Section 3.1.1. Here, the flatfield uncorrected images for all three contrast modalities (attenuation (ATT), dark-field (DFI), and differential phase contrast (DPC)), and the corresponding processed images are presented. In order to extract the images using the Fast-Fourier-Transform (FFT) algorithm, at least three phase-steps have to be acquired. However, to be less prone to artifacts, in this thesis, usually four or five phase-steps over one grating period were executed for the image acquisition. In the following, the calculation of the three different signals will be shortly introduced.

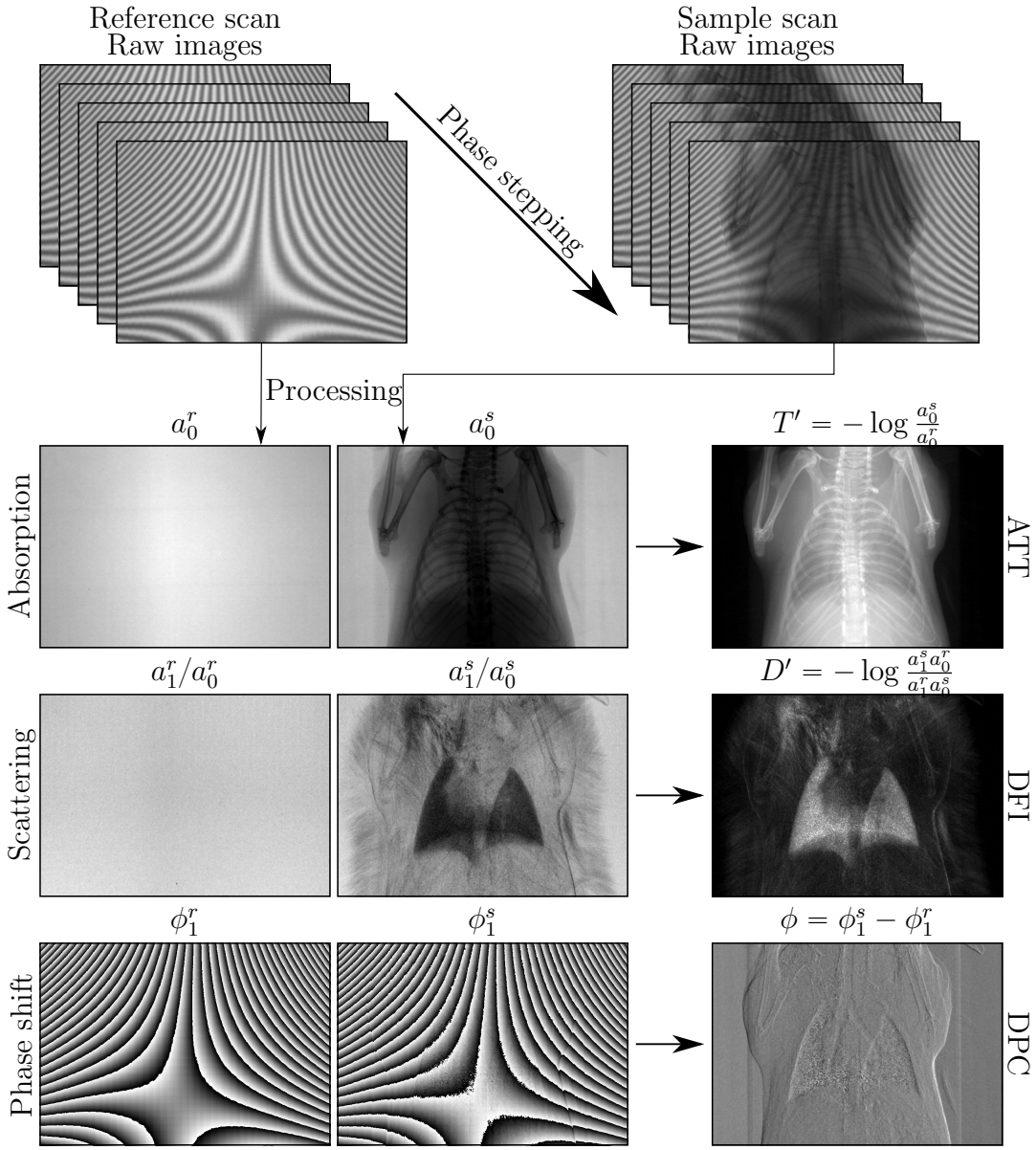

Figure 2.8: Processing chain for experimental phase-stepping data sets. Experimental raw images, acquired with five stepping positions over one period, with and without a mouse in the beam are shown on the top. For both data series, three respective image contrast signals a_0^i, a_1^i/a_0^i, and φ^i are obtained. The flatfield corrected images for the different signals ATT, DFI, and DPC are presented on the right. Figure adapted from [Birnbacher, 2018].

Transmission and Attenuation

The transmission T through an object is calculated by the ratio of the averaged mean intensity values for each pixel (x, y) acquired with and without an object in the beam

as

$$T = \frac{I(x,y)}{I_0(x,y)} = \frac{a_0^s(x,y)}{a_0^r(x,y)} = e^{-\int \mu(x,y,z)dz}. \tag{2.47}$$

The calculated transmission T can be related directly to the linear attenuation coefficient μ via Beer-Lambert law from Eq. 2.30. In clinical environment, the line integral, rather than the transmission image, is considered

$$T'(x,y) = -\log \frac{I}{I_0}. \tag{2.48}$$

Differential Phase-Contrast

As indicated in Figure 2.7(B), the phase-shifting property of an object leads to a phase offset between reference and sample scan. The difference between both stepping curves is the differential phase-contrast signal and can be calculated as

$$\varphi(x,y) = \varphi_1^s(x,y) - \varphi_1^r(x,y). \tag{2.49}$$

Due to the periodic nature of the phase-stepping curve, the phase shift is restricted to the interval $[0, 2\pi[$. In case of very strong phase gradients, the phase shift may exceed 2π, and an unwrapping algorithm has to be applied [Tapfer, 2013].

Dark-Field Contrast

Finally, the quality of an interferometer can be assessed by the visibility which is defined by the minimum and maximum intensity or the ratio between relative amplitude $a_1(x,y)$ and the mean intensity $a_0(x,y)$ as

$$V(x,y) = \frac{I_{\max} - I_{\min}}{I_{\max} + I_{\min}} = \frac{a_1(x,y)}{a_0(x,y)}. \tag{2.50}$$

A decrease in visibility of the stepping curve caused by the scattering property of the sample (see Figure 2.7(C)) is described by the dark-field signal as

$$D(x,y) = \frac{a_1^s a_0^r}{a_1^r a_0^s} = e^{-\frac{2\pi^2 d^2}{p_2^2}\int \epsilon(x,y,z)dz}, \tag{2.51}$$

with $\epsilon(x,y,z)$ denoting the linear diffusion coefficient and a setup dependent prefactor $\frac{2\pi^2 d^2}{p_2^2}$. In contrast to the conventional attenuation signal, the dark-field signal enables the visualization of small-angle scattering of features below the detector pixel size. However, also other phenomena can induce a dark-field signal. When performing measurements with a polychromatic source, a highly absorbing material causes beam

hardening, resulting in changes of the interference pattern and leading to a dark-field signal. This phenomena is independent on the scattering property of the respective material [Chabior, 2011]. Additionally, unresolvable, sharp edges in the FOV along the grating bars leading to a dark-field signal [Wolf, 2015; Yang, 2012; Yashiro, 2015]. Please note that grating interferometry with line gratings detect phase gradients only perpendicular to the lines. In order to further understand the theoretical basis of dark-field, several investigations were performed in the past [Pfeiffer, 2005; Yashiro, 2010; Lynch, 2011; Malecki, 2012; Strobl, 2014]. Nevertheless, the dominating origin for the dark-field signal was found to be small-angle X-ray scattering (SAXS), whereas the sensitivity of feature sizes is described by the autocorrelation length

$$\xi = \frac{\lambda d_{\mathrm{S,G_2}}}{p_2}, \tag{2.52}$$

where $d_{\mathrm{S,G_2}}$ is the distance between object and analyzer grating, and p_2 denotes the grating period of the analyzer grating [Prade, 2016].
As mentioned above, the fastest, simplest, and also most efficient approach to extract the parameters from the stepping curve is the FFT implementation. Alternatively, one could fit a sinusoidal to the measured data pixel-wise, and extract the parameters. A more advanced signal-extraction methods called "expectation-maximization algorithm" will be introduce in Section 3.1.2 in detail.

2.2.4 Imaging with Incoherent X-ray Sources

For the formation of an interference pattern at a certain distance from G_1, sufficient spatial coherence within the incident radiation must be present. As shown in Section 2.1.5, the spatial (or transverse) coherence directly depends on the lateral source size and the propagation distance. The requirement for spatial coherence is usually not met if a laboratory X-ray source with a larger focal spot size is used.
In order to describe the problem of spatial coherence with an extended X-ray source, the source can be considered to be a sum of separate, individual line sources located side by side [Bech, 2009]. One individual line induces an interference pattern at distance d from G_1. In contrast, an adjacent line shifted by ϵ introduces a slightly shifted interference pattern at a distance $\frac{\epsilon d}{l}$, where l is the distance between source and G_1, from the first interference pattern. Consequently, if $\frac{\epsilon d}{l} = \frac{p_2}{2}$, both interference patterns will interfere destructively and cancel out each other. This case is indicated in Figure 2.9(A). Based on this, the requirement for the source size s can be described as

$$s \leqslant \frac{p_2 l}{2d}, \tag{2.53}$$

where p_2 is the period of the analyzer grating. The superposition of many laterally displaced patterns causes the interference patter being smeared out or even vanished.

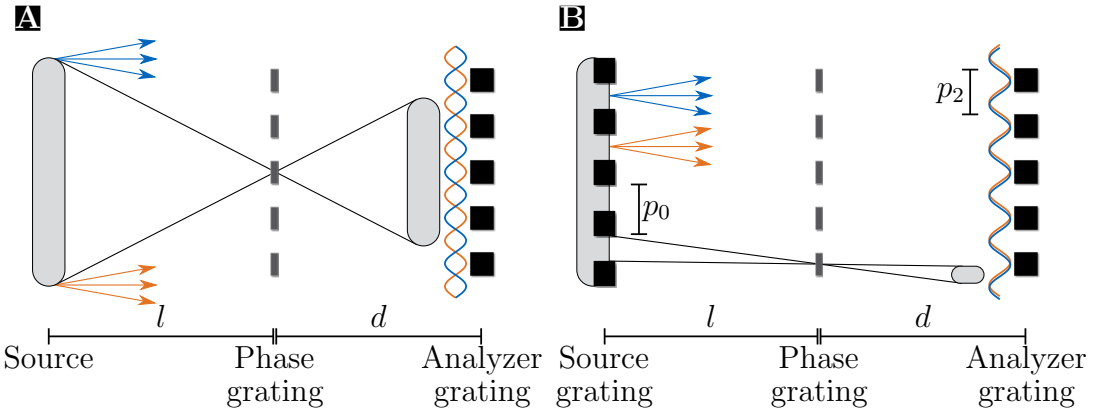

Figure 2.9: Spatial coherence with a extended X-ray source. (A) An extended source causes destructive interference and a cancellation of the interferometric pattern. This effect can be avoided by either increase to distance l between source grating and phase grating, or by inserting a source grating into the beam (B). Figure partly adapted from [Birnbacher, 2018].

In comparison to measurements at the synchrotron, where the source to phase grating distance is very large, and the requirement on transverse coherence is easily met, a conventional, laboratory X-ray source cannot fulfill this condition. As mentioned in Section 2.2.2, the solution to overcome this limitation was introduced by Pfeiffer et al. [Pfeiffer, 2006] by adding a third grating upstream from G_1. This so-called source grating G_0 acts as an array of slits for the extended X-ray source. The period of the source grating p_0 should be chosen as

$$p_0 = \frac{l}{d} p_2. \tag{2.54}$$

The case of inserted source grating can be seen in Figure 2.9(B).

2.2.5 Interferometer with Divergent Beam

Until now, it was assumed that there is a truly parallel beam and that a plane wave propagates through the interferometer. Apart from the synchrotron sources, where the beam can be assumed to be parallel as the source-to-sample distance is very large and the source size is very small, the divergence of the X-ray beam in lab cannot be neglected. More precisely, the magnification M

$$M = \frac{l + d}{l}, \tag{2.55}$$

has to be considered in the interferometer design. In Figure 2.10 a scheme of a setup with divergent beam is presented. Since the wavefront including interference pattern

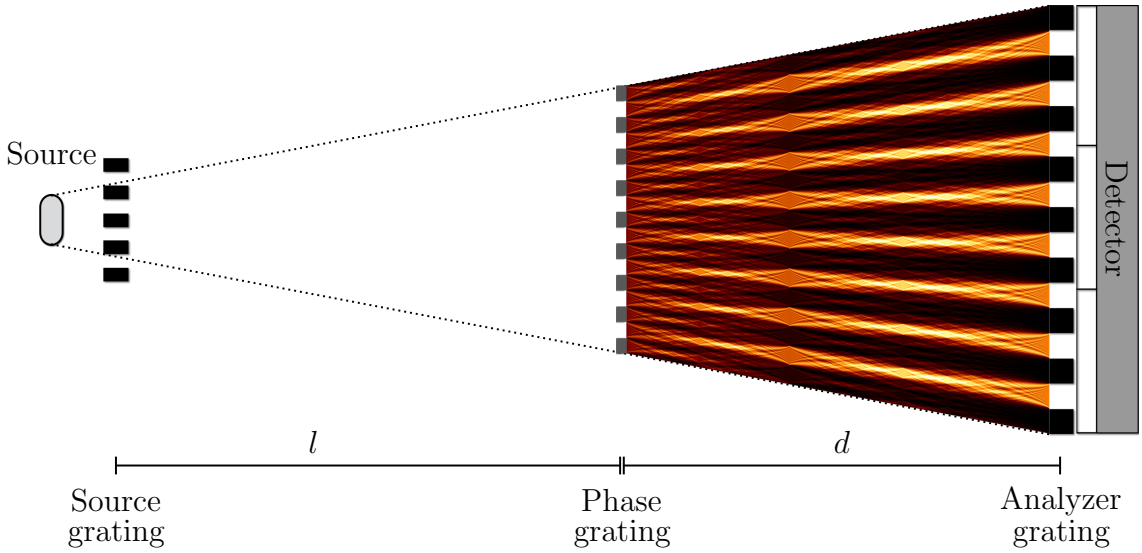

Figure 2.10: Magnification of the Talbot carpet. The magnification caused by the divergence of the X-ray beam causes a magnification of the interference pattern. Consequently, the grating periods and the respective grating distances have to be adapted accordingly. Figure partly adapted from [Bech, 2009].

is not travelling in parallel, the Talbot distance scales accordingly to

$$d'_{\mathrm{T}} = M d_{\mathrm{T}}. \tag{2.56}$$

As the period of the analyzer grating has to match the period of the interference pattern, it has to be adapted analogously to be

$$p'_2 = M p_2. \tag{2.57}$$

Consequently, the required period of the source grating changes to

$$p_0 = \frac{l}{d} M p_2. \tag{2.58}$$

In this case, only the global magnification of the wavefront was taken into account. In order to consider the local curvature of the wavefront, the gratings need to be bent according to their respective distance to the source. This will be described in Section 3.2.3.

2.2.6 Gratings

The X-ray optical gratings are the essential and decisive elements that enable the access to the phase-contrast and dark-field information when measuring with an X-ray interferometer. The source grating, which is an absorption grating, has to absorb

the X-rays emitted by the source in an adequate number to ensure a sufficient degree of coherence for the source. In contrast, the periodic grating structures of the phase grating cause a periodic modulation of the wavefront. In order to finally resolve the interference pattern on the detector, the use of an analyzer grating, which is also an absorption grating, is essential. In the following, the process of grating fabrication and the optimization of the grating configuration performed in the framework of this thesis will be described.

Grating Fabrication via LIGA Process

The grating production is one of the major challenges for grating-based interferometry as highly absorbing structures are required with high precision and accuracy. The fabrication approach of the gratings used is called LIGA process. The German acronym LIGA stands for "**Li**thographie, **G**alvanik, **A**bformung" and can be roughly divided into four parts, as visualized in Figure 2.11. In a first step, a thin titanium layer is sputtered to a standard silicon substrate in order to obtain a conductive basic layer. The titanium is oxidized, leading to a higher surface roughness and consequently improving the adhesion of the spin coated photosensitive resist. In the lithographic step, the grating structure is provided by a mask, consisting of a thin carrier membrane and an absorbing gold structure. This mask needed for the lithographic step is fabricated by electron beam lithography, direct laser beam lithography, or X-ray lithography, includes the desired grating layout, and can be used for the fabrication of both absorbing gratings and phase gratings [Koch, 2017]. The photoresist is irradiated at a low energy synchrotron, which provides a sufficient parallel and intense X-ray beam. The energy is in the range of $5 - 10\,\mathrm{keV}$ to guarantee a high penetration depth and avoid broadening of the illuminated structures due to secondary electron effects. As a consequence, the chemical structure of the irradiated area is changed and chemically cross-linked during a post exposure bake. Afterwards, the untreated photoresist can be removed via chemical development and wet-etching. As a final step, the gold absorber structures are electroplated into the removed structures [Becker, 1986; Kenntner, 2012]. Depending on the structure height, it might become necessary to further increase the stability of the lamellae to prevent them from deformation or collapsing. This can be achieved by including supportive structures into the grating design, with either the so-called bridges or the sunray design.

2.3 Principles of Computed Tomography

X-ray computed tomography is a non-destructive way to determine the 3D attenuation coefficient and therefore the interior of an object. Acquiring a series of projections from

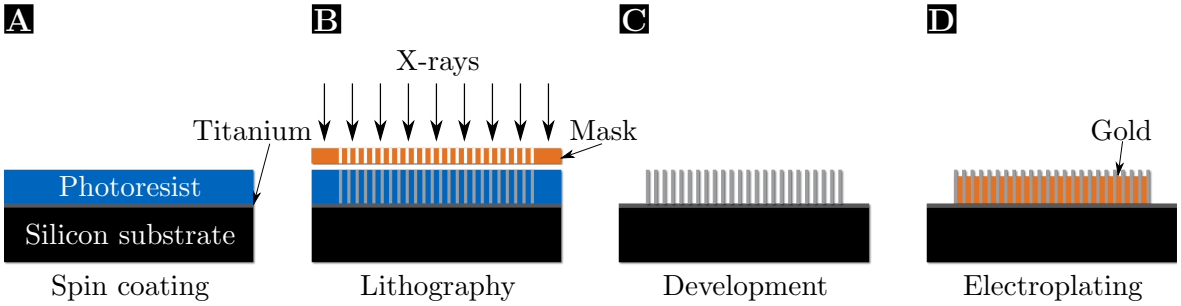

Figure 2.11: Schematic sequence of the LIGA process. (A) A previously with titanium sputtered and treated silicon substrate is spin coated with a photosensitive resist. (B) A binary absorption mask with the required grating structure is positioned in direct contact to the photoresist and illuminated with soft X-rays. (C) In this case, the negative photoresist is removed using chemical development. (D) By electroplating the remaining structure is filled by with an high absorbing material such as gold.

different angular views, one is able to reconstruct the inner composition of an object in all three dimensions. The most common and prominent approaches to reconstruct the data are filtered backprojection (FBP) and iterative reconstruction. The former is a reconstruction method which is fast and analytically well described, and as an example of the latter, a statistical iterative reconstruction (SIR) algorithm is presented. As the SIR algorithm includes prior knowledge of the object and statistical information in the reconstruction, the method is more complex and computationally more expensive. However, one is able to reduce the needed number of angular projections, and still obtain sufficient image quality [Buzug, 2008; Kak, 1988].

2.3.1 Radon Transform

CT systems nowadays work using a fan-beam geometry. However, for sake of simplicity, parallel beam geometry is assumed in the following. In Figure 2.12 the case of a single two-dimensional object $f(x, y)$ in a given plane $z = const.$ perpendicular to the axis of rotation is indicated. In that plane, we can consider a Cartesian (laboratory) coordinate system (x, y), and a second (gantry) coordinate system (s, t) with the same origin but rotated by an angle of θ

$$\begin{pmatrix} s \\ t \end{pmatrix} = \begin{pmatrix} \cos\theta & \sin\theta \\ -\sin\theta & \cos\theta \end{pmatrix} \begin{pmatrix} x \\ y \end{pmatrix}. \tag{2.59}$$

A straight line $l(\theta, s)$, which can be interpreted as X-ray photon path, under the fixed projection angle θ at a particular linear shift s from the origin can be described by

$$x\cos\theta + y\sin\theta = s. \tag{2.60}$$

The line integral of the object $f(x, y)$ along the straight line $l(\theta, s)$ in the laboratory coordinate systems can be rewritten as

$$p(s) := \iint_{-\infty}^{\infty} f(x, y)\delta(x\cos\theta + y\sin\theta - s)\mathrm{d}x\mathrm{d}y. \tag{2.61}$$

As the projection $p(s)$ varies with the projections angle θ, this parameter has to be included to the description to $p(s) = p(s, \theta) = p_\theta(s)$. The set of its line integrals $p_\theta(s)$, which is the two-dimensional Radon transform $\mathcal{R}_2$, is mapped to the entirety of all projections of the object $f(x, y)$

$$p_\theta(s) = \mathcal{R}_2[f(x, y)]. \tag{2.62}$$

However, a direct reconstruction of the object from the Radon transform would be computationally inefficient. The reconstruction can rather be accomplished using the Fourier slice theorem and filtered backprojection.

2.3.2 Fourier Slice Theorem

For the derivation of the Fourier slice theorem, a two-dimensional object $f(x, y)$ is considered, which is integrated along the y-axis under angle θ to generate a function defined by

$$p_\theta(x) = \int_{-\infty}^{\infty} f(x, y)\mathrm{d}y. \tag{2.63}$$

The one-dimensional Fourier transform of $p_\theta(x)$ is described by

$$P_\theta(u) = \int_{-\infty}^{\infty} p_\theta(x)e^{-2\pi i x u}\mathrm{d}x. \tag{2.64}$$

By definition, the two-dimensional Fourier transform of $f(x, y)$ leads to

$$F(u, v) = \iint_{-\infty}^{\infty} f(x, y)e^{-2\pi i(xu+yv)}\mathrm{d}x\mathrm{d}y. \tag{2.65}$$

If v is set to zero, the slice through $F(u,v)$ is given by

$$F(u,v=0) = \int_{-\infty}^{\infty} \left[\int_{-\infty}^{\infty} f(x,y)\mathrm{d}y \right] e^{-2\pi i x u}\mathrm{d}x. \tag{2.66}$$

Comparing Eq. 2.63 with the integral in the square brackets in Eq. 2.66, the basic idea of the Fourier slice theorem becomes obvious as

$$F(u,v=0) = \int_{-\infty}^{\infty} p_\theta(x) e^{-2\pi i x u}\mathrm{d}x = P_\theta(u). \tag{2.67}$$

The one-dimensional Fourier transform of the projection of a two-dimensional sample $f(x,y)$ taken at angle θ along a particular line correlates to a radial profile of the Fourier transform of $F(u,v)$ of the respective sample perpendicular to the direction of projection. Consequently, for sufficient dense sampling, the inner structure of an object function $f(x,y)$ can be determined via two-dimensional inverse Fourier transform of $F(u,v)$. The principles of the Fourier slice theorem are illustrated in Figure 2.12.

2.3.3 Filtered Backprojection

The algorithm of the FBP is currently being used most commonly for tomographic reconstruction as it is accurate and comparable easy to implement. For reconstruction purpose it uses directly the projection measurements $p_\theta(s)$, benefiting from the Fourier slice theorem.
Converting Eq. 2.65 and transforming the rectangular coordinate system to polar coordinates by substituting $u = \omega\cos\theta$ and $v = \omega\sin\theta$, and change the differentials by $\mathrm{d}u\mathrm{d}v = |\omega|\mathrm{d}\omega\mathrm{d}\theta$ we obtain

$$f(x,y) = \int_{0}^{\pi} \int_{-\infty}^{\infty} |\omega| F(u,v) e^{2\pi\omega i(ux+vy)}\mathrm{d}\omega\mathrm{d}\theta. \tag{2.68}$$

More details about the conversion and transformation can be found in Kak and Slaney [Kak, 1988]. According to the Fourier slice theorem, the two-dimensional Fourier transform $F(u,v)$ can be substituted by the Fourier transform of the projection $P_\theta(\omega)$ resulting in

$$f(x,y) = \int_{0}^{\pi} \left[\int_{-\infty}^{\infty} |\omega| P_\theta(\omega) e^{2\pi i\omega s}\mathrm{d}\omega \right] \mathrm{d}\theta. \tag{2.69}$$

The integral in the squared brackets represents a filtering operation in Fourier space on the measured projections, and therefore it is called “filtered projection”. The factor

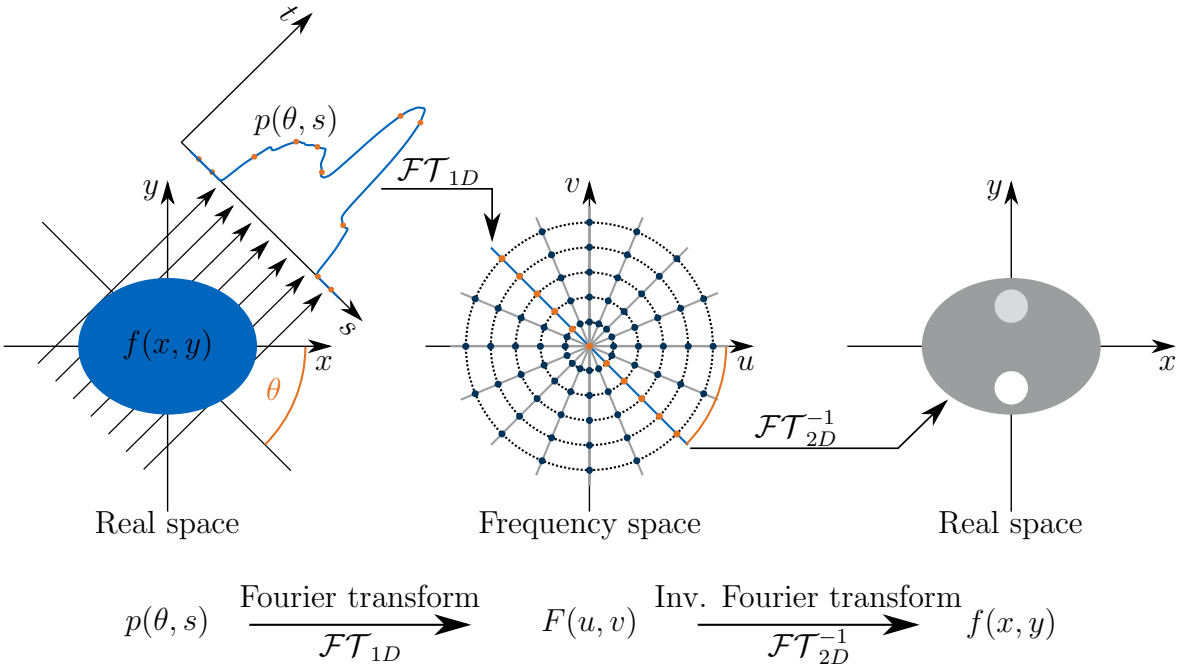

Figure 2.12: Illustration of the Fourier slice theorem. The measurement of the observed object under angle θ leads to the projection $p(\theta, s)$. The one-dimensional Fourier transform of $p(\theta, s)$ is equal to a line, at angle θ, through the object function in Fourier space. For sufficient dense sampling, the object function $f(x, y)$ can be determined via two-dimensional inverse Fourier transform of $F(u, v)$ and internal structures of the object can be identified (indicated with the two circles within the object).

$|\omega|$ corresponds to a filter as it accounts for the denser sampling towards the origin in Fourier space as indicated in Figure 2.12. The Fourier filter compensates the closer sampling by normalization with this factor and weighting the high-frequency components stronger than the low-frequency components. Thus, Eq. 2.68 can be rewritten as

$$f(x, y) = \int_0^{\pi} \mathcal{FT}^{-1}\{F(\omega)P_\theta(\omega)\}\mathrm{d}\theta. \tag{2.70}$$

The integral depicts the sum of the filtered projections over all angles θ. Finally, this represents the "backprojection" to the image plane. In practice, the number of angular projections is limited to a finite number. Consequently, as depicted in Figure 2.13 the Fourier transform $F(u, v)$ is known on a finite number of radial lines in the coordinate system. However, as the reconstructed sample is defined in a Cartesian coordinate system, whereas the sampling in Fourier space is done in a frequency domain, an interpolation between both grids is required.
The Nyquist criterion necessary for sufficient data sampling in the Fourier domain (also

in the outer regions)

$$\mathcal{N}_\theta = \frac{\pi}{2}\mathcal{N}_{\text{pix}} \tag{2.71}$$

has to be fulfilled for a correct representation of the reconstructed sample using FBP. $\mathcal{N}_\theta$ depicts the number of angular projections distributed over 360° acquired during CT measurement, and $\mathcal{N}_{\text{pix}}$ are the sampling points in horizontal direction in each projection. In general, the Nyquist sampling theorem states that a signal must be sampled at least twice during each cycle of the highest frequency of the signal [Kak, 1988; Natterer, 1986].

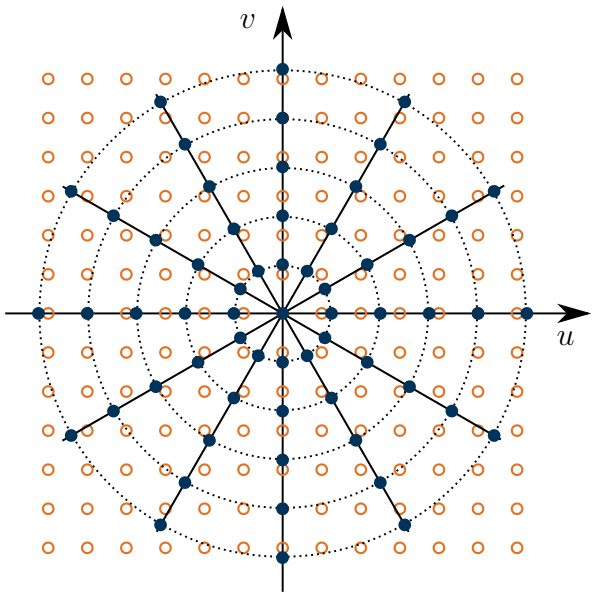

Figure 2.13: Data sampling in Fourier space. When acquiring various projections under several angles in real space the sampling is performed at radial lines in polar coordinates (black dots). Obviously, the lower the frequencies close to the origin the denser is the sampling. In contrast to that, at higher frequencies the sampling is more sparse. By using a discrete Fourier transform algorithm, the radial slices are filled by further projections and transformed to Cartesian coordinates u and v represented by the orange rings. Figure partly adapted from [Buzug, 2008].

As stated in Eq. 2.47, the transmission T under angle θ is related to the linear attenuation coefficient μ according to Beer-Lambert law and can be expressed in the rotated coordinate system as

$$T_\theta(s) = e^{-\int_0^D \mu(s,t)\mathrm{d}t}, \tag{2.72}$$

where the integration is performed along the t axis between 0 and the thickness D of the non-homogeneous sample with object function $\mu(s,t)$. A projection along the line

defined by the coordinates θ and s can be described with the object function and the negative logarithm of the calculated transmission as the line integral

$$p_\theta(s) = -\log(T_\theta(s)) \tag{2.73}$$

$$= \int_0^D \mu(s,t)\mathrm{d}t. \tag{2.74}$$

In analogy to the tomographic reconstruction of the conventional absorption signal, the volume of the dark-field signal can be calculated from the linear diffusion coefficient ϵ, which describes the local scattering ability of a sample exhibiting to X-rays. Here, the projection function is equal to the logarithm of the measured visibility as

$$p_\theta(s) = -\log\left(\frac{p^2}{2\pi^2 d^2} V_\theta(s)\right) \tag{2.75}$$

$$= \int_0^D \epsilon(s,t)\mathrm{d}t. \tag{2.76}$$

However, according to Pfeiffer *et al.* [Pfeiffer, 2007b] the reconstruction of the differential phase-contrast volumes needs the usage of the so-called Hilbert filter

$$H(\omega) = \frac{1}{2\pi i \,\mathrm{sgn}(\omega)}, \tag{2.77}$$

which is the equivalent to the ramp filter with an included integration because of the characteristics of the Fourier transform.

2.3.4 Statistical Iterative Reconstruction

Using fast algorithm of FBP requires a sufficient data sampling of the Fourier space according to the Nyquist criterion for a correct representation of the reconstructed volume. Besides this constraint, the data set must have minimal noise and no distorted projections or features that cause artifacts. As explained later on in this thesis, the total acquisition time is one limiting factor when measuring at the Skyscan 1190, since the overall time for a CT fulfilling the Nyquist criterion is limited by the anesthesia duration and the aim of not harming the animal. Furthermore, due to gold as absorbing structures of the gratings in the beam and the phase-stepping procedure with more than three images per angular projection, grating-based dark-field imaging inherently requires a higher dose per projection compared to conventional absorption imaging,

and the requirement to reduce acquisition time and hence radiation dose is even more important than with existing clinical CT imaging. Hence, CT volumes presented within this thesis are mainly reconstructed with a statistical iterative reconstruction (SIR) algorithm implemented by Hahn [Hahn, 2014]. SIR combines algebraic techniques, noise model and an iterative reconstruction which results in better handling with undersampled data compared to FBP. The following sections briefly summarize the principles of this algorithm limited to a 2D object and its projection measurements. For further reading and detailed description please refer to [Hahn, 2014] or [Hsieh, 2003].

In order to describe the iterative reconstruction algorithm, the volume of the object to be reconstructed is represented by vector $\mathbf{f}$, which is linked to the experimentally measured set of projections contained in the vector $\mathbf{p}$ via the system matrix A by

$$A\mathbf{f} + \mathbf{e} = \mathbf{p}. \tag{2.78}$$

For real systems, the matrix A is determined by geometrical and physical properties of the CT system, such as focal spot size and shape, or detector response. Moreover, an additional error vector $\mathbf{e}$ which accounts for any measurement bias or additive noise can be considered. For the reconstruction, the quantity of interest is the volume $\mathbf{f}$. An inversion of Eq. 2.78 leads to the inverse problem. Due to the enormous size and computational efforts, a numerical solution has to be found.
In a first step, similar to the FBP reconstruction the reconstructed volume is discretized. Next, prior knowledge of the sample as well as a forward model, which simulates the measurement from an initial estimate of $\mathbf{f}$ by summing up the voxel values along a particular ray path and assign it as the projection $\mathbf{p}'$ on the detector, and a data model are included to the reconstruction. In the following, these artificially generated projections $\mathbf{p}'$ are compared to the measured projections $\mathbf{p}$ by calculating the log-likelihood minimization. The log-likelihood minimization is then used to update the initial estimate of $\mathbf{f}$. This procedure is repeated in a loop, until a certain convergence criterion or a certain amount of iterations is reached. Using statistical iterative reconstruction, statistical models of the noise within the acquired data are additionally included into the reconstruction process. Therefore, a confidence map of the acquired projection data is created via statistical noise models, which finally leads to a weighting of the projection values for updating the objection function $\mathbf{f}$. This iterative reconstruction algorithm is intended to find the minimum of the log-likelihood function $\mathcal{L}$ which can be expressed as

$$\mathcal{L} = ||A\mathbf{f} - \mathbf{p}||_w^2, \tag{2.79}$$

with w denoting the statistical weights. However, since the minimization problem is ill-conditioned and results in too much noise due to many possible solutions, a

regularization term, in this case the Huber potential [Huber, 1992] defined as

$$\mathcal{R}_{\mathrm{H}}(\mathbf{f},\gamma) = \sum_i \sum_{j\in\mathcal{N}_i} m_{ij} \begin{cases} \frac{(f_i-f_j)^2}{2\gamma^2} & \text{for } |f_i - f_j| \leqslant \gamma, \\ \frac{|f_i-f_j|-\gamma/2}{\gamma} & \text{for } |f_i - f_j| \geqslant \gamma, \end{cases} \tag{2.80}$$

has to be included to $\mathcal{L}$, resulting in

$$\mathcal{L} = ||A\mathbf{f} - \mathbf{p}||_w^2 + \lambda \mathcal{R}_{\mathrm{H}}(\mathbf{f},\gamma). \tag{2.81}$$

The regularization strength parameter λ can be varied such that a trade-off between noise reduction and resulting spatial resolution has to be found. In contrast, the regularization parameter γ defines the threshold for linear or quadratic penalization of differences between neighboring pixels $\mathcal{N}_i$ with respect to pixel i and weights m_{ij}.

Experimental Setup and Scanner Optimization 3

This chapter describes the experimental in-vivo phase-contrast and dark-field setup which was used for imaging purposes during this thesis and the corresponding setup optimization. All presented images have been acquired with the prototype micro-CT scanner "Skyscan 1190" developed in collaboration with Bruker microCT (Kontich, Belgium) and which will be described in the first part of this chapter. Moreover, important technical components and the theory behind them are explained in more detail: The generation and detection of X-rays, as well as grating fabrication. Furthermore, peculiarities of the measurements with a Talbot-Lau interferometer will be explained. The second part of this chapter describes the optimization measures in order to increase the image quality and the performance of the setup. Please note that parts of the results of this section have been published in Umkehrer et al. [Umkehrer, 2019].

3.1 Materials and Methods

3.1.1 Experimental Setup

A photograph and a schematic drawing of the scanner are depicted in Figure 3.1. The scanner is a compact grating-based phase-contrast CT (GBPC-CT) system: it consists of a rotating gantry, a stationary sample stage allowing for *in-vivo* radiography and CT measurements, and a Talbot-Lau interferometer mounted to the gantry. This Talbot-Lau interferometer consists of three gratings, more precisely a source grating (G_0) with a period of 10 µm, a phase grating (G_1) with a period of 3.24 µm, and an analyzer grating (G_2) with a period of 4.8 µm, which all were fabricated by microworks GmbH (Karlsruhe, Germany). The source grating is mounted on a piezo positioner, in order to perform the phase-stepping, and can be rotated for grating alignment. Moreover, the phase grating is motorized to be moved in all of the three directions, to be tilted in two directions and rotated perpendicular to the beam path in order to allow for correct alignment of the gratings. The distance between source and phase grating is 30 cm, whereas the distance between analyzer and phase grating is 14.5 cm. The interferometer operates in the first fractional Talbot order and the design energy of the

interferometer is 23 keV. More details on the gratings can be found in Section 3.2.3. As already mentioned, the gantry, including source, gratings and detectors, rotates around the stationary sample bed, which can be positioned in one direction. As X-ray source, a fixed anode tungsten-target MCBM 65B-50W X-ray tube (RTW, Neuenhagen, Germany) is used. The methods about the generation of X-rays are described in detail in Section 2.1.1. Two different detectors are used within this thesis. The first is a Hamamatsu flat panel C9312SK-06 detector (Hamamatsu, Japan) with a gadolinium oxysulfide (GOS) scintillator and a cooled 12-bit CCD camera with a pixel size of 50 µm pixel size. The second is a Dexela flat panel detector (1512S-C90-H-100, Varex Imaging, USA) with a GOS scintillator and a CMOS image sensor with a pixel size of 74.8 µm. The source-to-sample distance is 27 cm, whereas the distance from the sample to the detector is 20 cm. Due to geometric magnification caused by the cone-beam geometry, the respective pixel sizes in the sample plane are approximately 30 µm and 45 µm. More details on X-ray detectors can be found in Sections 2.1.2 and 3.2.2.
The compact micro-CT includes different equipment features in order to monitor physiological functions. The breathing motion can be captured via a small video-camera. Furthermore, the heart beat and the body temperature can be measured for *in-vivo* experiments. A warm-air fan inside the scanning chamber can be used to prevent the *in-vivo* specimen against hypothermia. The raw images are acquired using the supplied control-software, which saves the raw projection images of the phase-stepping acquisition in the data type "Tagged Image File Format" (TIFF). In addition, scanner specifications and acquisition parameters such as exposure time are written into a text-based log file.
The design of the Talbot-Lau interferometer is decisive for the acquisition of phase-contrast and dark-field signals with a specific setup or a particular sample. More precisely, the aspect ratio, grating periods, and grating-to-grating distances have to be adapted to fit to the available gantry, the spectrum and the design energy, and the specimen to be investigated. The measurements in this thesis were taken with parameters optimized for the present setup, including the consideration of the sample and Talbot carpet magnification. In the following, the setup and the optimization steps will be explained in more detail, followed by the mechanism of data acquisition and image processing.

In order to evaluate the influence of several changes and improvements of the experimental setup, phantom measurements were performed. For this purpose, a 3D printed tube - with the dimensions of a mouse thorax - acts as dark-field phantom. Different features are inserted into this water filled phantom: In plastic foil wrapped earplugs in order to imitate the lungs, one rod of polyvinylchloride (PVC) which is highly absorptive and therefore is able to simulate the bones and spine, and one rod of polymethylmethacrylate (PMMA), which mimics phase-contrast information and simulates the absorption of soft tissue.

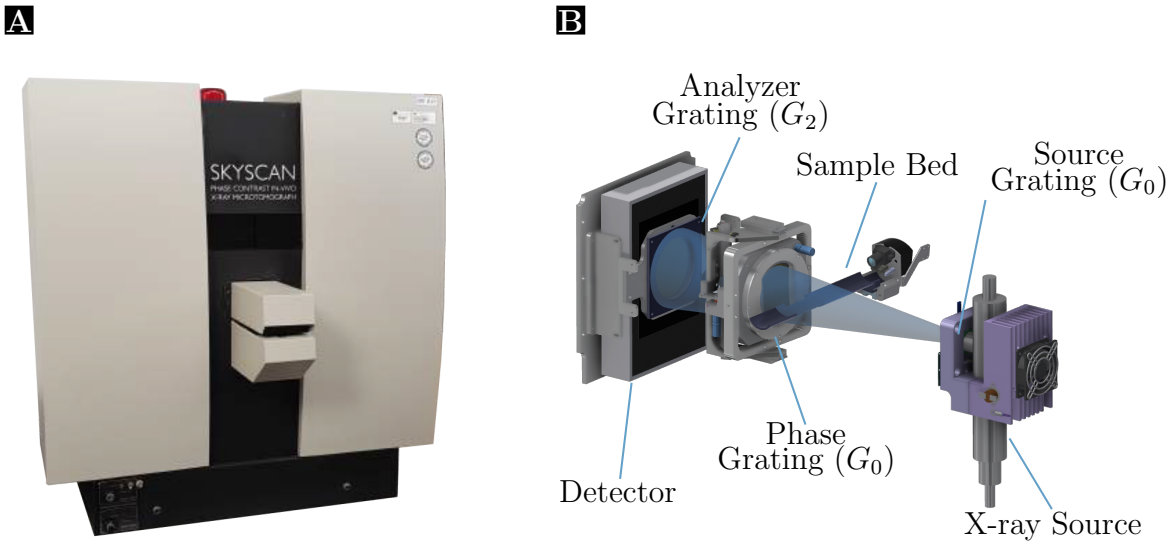

Figure 3.1: Photograph and sketch of the small-animal X-ray phase-contrast and dark-field CT scanner. Subfigure (A) shows a photograph of the compact micro-CT housing. In subfigure (B) a technical drawing of the source, the sample bed, the detector, and all gratings of the Talbot-Lau interferometer are depicted.

3.1.2 Signal Extraction

The processing to obtain the additional contrast information is not as straightforward as in conventional attenuation-based imaging. In addition to the standard processing using the Fast-Fourier-Transform as introduced in Section 2.2.3 and the phase-stepping for data acquisition as introduced by Weitkamp et al. [Weitkamp, 2005], there are more advanced algorithms or techniques in order to extract the attenuation, differential phase-contrast, and dark-field signal from measured raw images. In the following, the concept of processing using an expectation-maximization algorithm (EM) will be explained. Afterwards, more advanced and sophisticated image acquisition schemes will be shortly introduced.

Expectation-Maximization Processing

When using a Talbot-Lau interferometer on a rotating gantry, it is challenging to ensure the stability of the setup during the image acquisition. The exposed radiation can cause thermal expansion of the source grating or the mounting, resulting in a phase drift in the raw images. Additional mechanical fluctuations occur due to gravitational force and vibrations, which affects the grating alignment in dependency of the gantry angle [Tapfer, 2013]. Processing the raw images with the FFT implementation, residual fringe artifacts are probable to occur. This effect is caused by the systematic fluctu-

ations which contribute to the fitting parameters describing the stepping curve. To overcome this issue, a more advanced processing algorithm based on the expectation-maximization (EM) algorithm [Dempster, 1977; Do, 2008] can be used. According to Velroyen [Velroyen, 2015], the EM algorithm can be described in four steps, assuming that all measurements being independent and identically distributed:

1. A first estimation of the stepping position and respective fluctuation is made for each pixel independently. In an ideal measurement with equidistant steps, with the number of stepping positions n, the stepping position s_i, the intensity ΔI and the visibility ΔV should result in: $s_i = i\frac{p_2}{n}$, and $\Delta I = \Delta V = 1$.

2. Including the guessed parameters from step 1, which are assumed to be fix, and using a linear least-squares fit, the maximum-likelihood solution for the model is found and the parameters a_0, a_1, and φ_1 are calculated by solving a system of equations.

3. The parameters which were initially guessed in step 1 are optimized for each position by solving another linear system including the parameters a_0, a_1, and φ_1. This step ensures the consistency of the intensity variations across the pixels. The optimized parameters are the new estimation for the stepping position.

4. Steps 2 and 3 are repeated until the total variation of the stepping positions in the current iteration reaches a certain convergence.

For more details and information about the processing with the EM algorithm, the reader is referred to [Velroyen, 2015] and [De Marco, 2015].

Advanced Acquisition Schemes

As mentioned before, there are also alternative techniques and acquisition schemes for the extraction of the different signals compared to the phase-stepping approach, such as the Moiré analysis method or sliding window approach as single-shot techniques, [Momose, 2011; Bevins, 2012; Zanette, 2012] fringe-scanning [Kottler, 2007], or the so called intensity-based statistical iterative reconstruction (IBSIR) [vTeuffenbach, 2017]. The single-shot method of the sliding window approach requires the acquisition of a single interferogram per angular projection, but needs a different grating positions for each adjacent projection angle. By interpolating the absent interferograms from adjacent angle scans a recreation of a classical phase-stepping scan and processing the images works well for high number of angular projections. However, if the amount of projections is limited, the interpolation results in blurring and artifacts [vTeuffenbach, 2017]. The approach of IBSIR on the other hand does not extract the various signals,

but the phase-stepping image formation is included directly into the tomographic reconstruction.
Using this setup, and according to Teuffenbach et al., a combination of the concepts of sliding window and IBSIR, where the IBSIR reconstruction algorithm was applied to a data stack recorded with a sliding window pattern, was carried out. However, for stability and sensitivity reasons, the phase-stepping approach and the EM algorithm was used for all *in-vivo* measurements.

3.2 Setup Optimization

3.2.1 X-ray Source

The X-ray source used in this work is a RTW MCBM 65B-50W (RTW, Neuenhagen, Germany). The target is a fixed anode tungsten target with a focal spot size of $50 \times 50\,\mu m^2$. The maximum peak voltage, which can be adjusted, is 50 kV and the maximum current is 0.8 mA resulting in a maximum power of 40 W. Yet, the established source parameters for the measurements are 37 kV and 0.66 mA due to matching the mean energy of the spectrum for the design energy of the interferometer.

3.2.2 Detector Characterization

Within this work two different flat panel detectors were used to acquire the images: an initial Hamamatsu and a new Dexela detector. The main reason for changing the detector was to optimize the setup towards computed tomography measurements. In order to compare the performance of both detectors, resolution measurements were performed. In general, there are several ways to measure and evaluate the spatial resolution of an imaging device such as the knife-edge approach, where a dense sample with a sharp and straight edge is placed between source and detector, or the Siemens star approach. As the latter enables the access to a full two-dimensional information of the resolution, and as the Siemens star could easily be inserted into the grating mounting of the analzyer grating, this approach was chosen within this thesis. For this measurement the analyzer grating G_2 was removed and the Siemens star resolution pattern is placed directly in front of the detector. The Siemens star resolution pattern consists of 90 rays and a central solid round plate, both made of lead with a thickness of 0.05 mm. With this configuration, the blurring effect of the source as well as the geometrical magnification can be neglected so that the PSF of the detector can be determined directly. However, the desired information of the PSF cannot be measured directly using this approach. Therefore, the modulation transfer function (MTF), containing the resolution information of a detector in dependency of the spacial frequency, can be

used in order to calculate the PSF. The most important steps, which are executed by this script, are briefly introduced in the following, based on the description in Viermetz [Viermetz, 2015]:

- **Flatfield correction and normalization**
  In a first step, the raw Siemens star image gets cropped to the corresponding region of interest (ROI) and flatfield corrected. After a bad pixel interpolation, the intensity range of the pixel values is normalized between 0 and 1.

- **Siemens star center calculation**
  Starting from an user-selected seed in the center region, the segmentation approach is performed in order to identify and mask the central solid round plate. From the resulting mask, the center of mass is calculated in order to obtain the center of the Siemens star.

- **Analysis of radial line plots and MTF generation**
  For all pixels on a circle around the center plate, the alternating high and non-absorbing structures induce a fixed frequency modulation (frequency depends on radius ρ) which is overlayed by an angle-dependent modulation, defining a measure of the sharpness of the edge appearance. By calculating and plotting an upper envelope function $U_\mathrm{e}(\alpha, \rho)$ and a lower envelope function $L_\mathrm{e}(\alpha, \rho)$ the contrast c between the alternating intensities is obtained via

  $$c(\alpha, \rho) = \frac{U_\mathrm{e}(\alpha, \rho)}{L_\mathrm{e}(\alpha, \rho)}. \tag{3.1}$$

  From the radial intensity envelope functions, where different ρ represent different spatial frequencies, the modulation transfer function MTF is generated. Combining all analyzed radial plots for all possible values of ρ results in the angle-depend MTF.

- **PSF calculation**
  By transforming the obtained MTF into Cartesian coordinates and performing a Fourier transform according to

  $$\mathrm{PSF} = |\mathcal{FT}(\mathrm{MTF})|, \tag{3.2}$$

  the frequency information about the spatial resolution is converted into a function of space represented by the PSF. In a perfect imaging device, the MTF of all frequencies would produce full contrast and consequently the Fourier transformation would be point-like. In particular in the areas of high frequencies at the center-near pixels, the transformation, however, strongly depends on the resolution and the included noise.

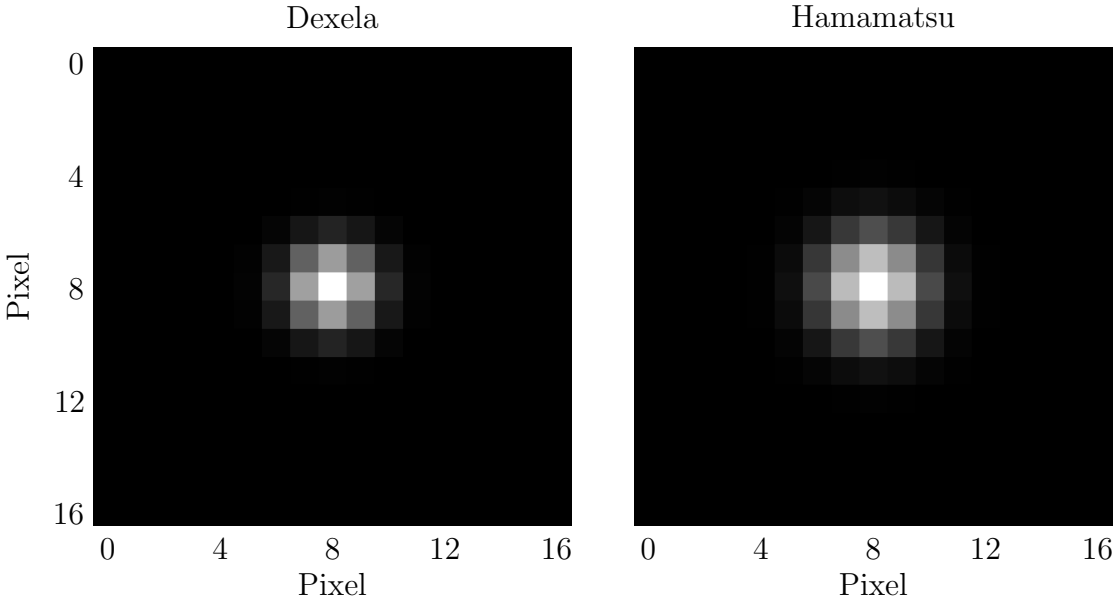

Figure 3.2: Determination of the respective detector PSFs. The PSFs of the different detectors were measured with the Siemens star directly in front of the respective detector without any significant geometric magnification. The resulted PSFs are Gaussian shaped.

The specification as well as the obtained PSF and LSF of both detectors are listed in Table 3.1. In Figure 3.2, the generated PSF of both imaging devices is shown. Figure 3.3 presents the LSF in vertical and horizontal direction. One can clearly see that the PSF of the Dexela detector is smaller in number of pixels compared to the Hamamatsu detector (0.98×0.95 vs. 1.25×1.26). However, for the quality of the images and the resolution which can be achieved, the minimum size of a resolvable feature is decisively. Furthermore, as the pixel size of the Hamamatsu detector is about one third smaller in each direction, quantitatively the variance of the LSF in real-space is smaller with $(73.6 \times 71.4)\,\mu m^2$ vs. $(62.4 \times 62.9)\,\mu m^2$, and therefore the spatial resolution of the Hamamatsu is slightly higher. Nevertheless, the variances of both detector systems are comparable which results in a similar resolution. Therefore, no significant loss of resolution is expected by the implementation of the new Dexela detector.

Two different approaches for the characterization of the spatial resolution of the Hamamatsu detector system have been performed by Müller [Müller, 2013]: A direct MTF measurement and an edge profile measurement. As the raw images of the scanner intrinsically feature a periodic fringe pattern, those were used for direct MTF measurement. However, an additional approach has been performed using the edge of the analyzer grating G_2 as a knife edge. Since the effective size of the grating is smaller than the active area of the detector, the borders of the gold structures and the surrounding silicon wafer of the grating could be observed in the raw images. The design

	Hamamatsu C9312SK-06	Dexela 1512S-C90-H-100
Type	Flat panel detector	Flat panel detector
Scintillator	Gadolinium oxysulfide	Gadolinium oxysulfide
Sensor	CMOS	CMOS
Resolution	2472 × 2184 pixel	1944 × 1536 pixel
(Effective)Pixel size	$50.0 \times 50.0\,\mu m^2$ $(28.7 \times 28.7\,\mu m^2)$	$74.8 \times 74.8\,\mu m^2$ $(43.0 \times 43.0\,\mu m^2)$
Photosensitive area	$124.8 \times 115.2\,mm^2$	$145.4 \times 114.9\,mm^2$
Data range	12 bit	14 bit
Frame rate	8 fps	86 fps
σ_{PSF}	$(62.4 \times 62.9)\,\mu m^2$ (1.25×1.26) pixel	$(73.6 \times 71.4)\,\mu m^2$ (0.98×0.95) pixel

Table 3.1: Specifications and properties of both imaging detectors used within this thesis.

of this grating includes sharp, staircase-arranged edges between highly absorbing gold bars and the wafer. Furthermore, since the gratings are produced with high precision, the borders could be assumed to be parallel. Due to the positioning of the grating right in front of the detector, the geometric magnification can be neglected as well. Moreover, the LSF was not determined within a single position, but by repeating this measurements at various points along the edge axis. The results are tabulated in Table 3.2.
As the function is considered to be Gaussian and therefore a normal distribution, the relationship between FWHM and σ accounts to

$$\mathrm{FWHM} = 2\sqrt{2\ln 2}\,\sigma. \tag{3.3}$$

Calculating the LSF from the tabulated FWHM results in $\sigma_{PSF} = 68.4\,\mu m$, which is consistent within the specified error value with the measurements of this thesis.
However, using laboratory systems, not solely the PSF of the detector system is crucial, but also the PSF of the source has to be considered. Moreover, also the positioning of the sample in the beam, which results in varying magnification factor has an effect on the resolution of the system. With an increasing distance from the source the magnification of the sample increases, resulting in a higher contribution of the source PSF to the system. By contrast, the effect of the PSF of the detector is decreasing

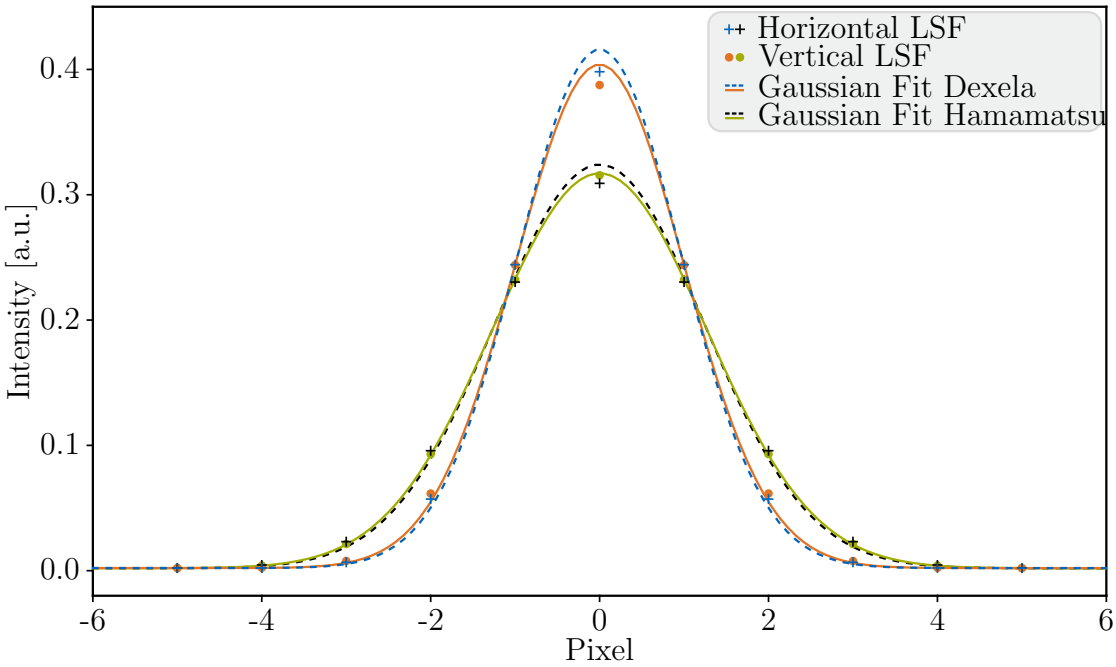

Figure 3.3: Determination of the detector LSFs. The horizontal (dashed lines) and vertical (solid lines) profiles of the PSFs of the Dexela (blue and orange) and the Hamamatsu (black and green) detectors result from the Fourier transform of the MTF. Both detectors' underlying Gaussians for horizontal and vertical LSFs.

with increasing magnification. Furthermore, movements or vibrations of the sample has an effect to the resolution of the image. With decreasing pixel size, the blurring caused by movements of the sample such as breathing motion increases. Nevertheless, it has been shown that the impact of the source profile can be neglected and hence, the system's PSF from Equation 2.11 can be approximated as detector PSF

$$\mathrm{PSF}_{\mathrm{system}} \approx \mathrm{PSF}_{\mathrm{detector}} \tag{3.4}$$

[Müller, 2013]. However, the isolation and quantitative assessment of the individual contributions is a very complex task, and would exceed the scope of this work. Therefore, it has not been included into this thesis.

Beside the spatial resolution, the noise performance and efficiency of the detector has an impact on the image quality. Features with signal intensities larger than the noise level in the image can be resolved, whereas others cannot be detected. Therefore, the ability of absorbing and detecting a large share of the incoming X-ray photons is decisive for detector systems. In order to compare the detected intensity, both detectors are exposed under the same conditions - i.e. the same grating configuration, current, and voltage - varying the exposure times. The analysis was performed by calculating

Resolution measure	Fringe pattern approach	G_2-Edge approach
FWHM of LSF [µm]	161 ± 10	161 ± 10
FWHM of LSF [pixel]	3.22 ± 0.20	3.22 ± 0.20

Table 3.2: Resolution for the Hamamatsu detector obtained from edge profile measurements at the edges of G_2 grating and the analysis of the Moiré pattern using the Fourier sum method. Results are summarized from [Müller, 2013].

the mean number of counts per pixel for a ROI in the centre of the FOV. In this case, the photon flux is assumed to be equal for both series of measurements. Figure 3.4 shows the signal intensity plotted as a function of the exposure time with a linear fit to compare the respective detectors. As one can see, the mean intensity follows a linear correlation with the exposure time. The Dexela detector follows the linear fit with a slope of 10.5×10^4 and an intercept of 160; in contrast the mean intensity of the Hamamatsu detector follows a slope of 4.0×10^4 with an intercept of 267. Obviously, the Dexela detector is more sensitive to incoming photons compared to the Hamamatsu detector. On the one hand, this can be explained by a higher quantum efficiency, and on the other hand, a larger area of one pixel leads to an increased number of photons per pixel. The relation between the area of one single pixel accounts to $A_{\mathrm{Dex}} \approx 2.2 A_{\mathrm{Ham}}$. Due to overexposure and the end of its dynamic range, the Dexela detector is limited to exposure times smaller than 1.9 s.

3.2.3 Optimization of Grating Configuration

Using a plane grating configuration with a fan-angle or a cone-beam geometry includes two major drawbacks: Increased shadowing as well as a mismatch in phase shift introduced at the offside regions of the analyzer grating due to a longer beam path within the interferometer. The X-rays impinge perpendicularly on the grating only in the optical axis. The angle of incidence α depends on the source-to-grating distance l and the distance x between the optical axis and the grating structures and can be expressed as

$$\alpha = \arctan(x/l). \tag{3.5}$$

As a consequence, X-rays impinging offside the optical axis get more and more absorbed by the grating bars which consequently leads to a decreased transmission. This effect is referred to as shadowing. Furthermore, offside the optical axis the inter-grating distance between phase grating and analyzer grating does not correspond to the Talbot distance. This results in an inappropriate phase shift applied to the wavefront and finally in a reduced visibility. Consequently, the gratings need to be bent according

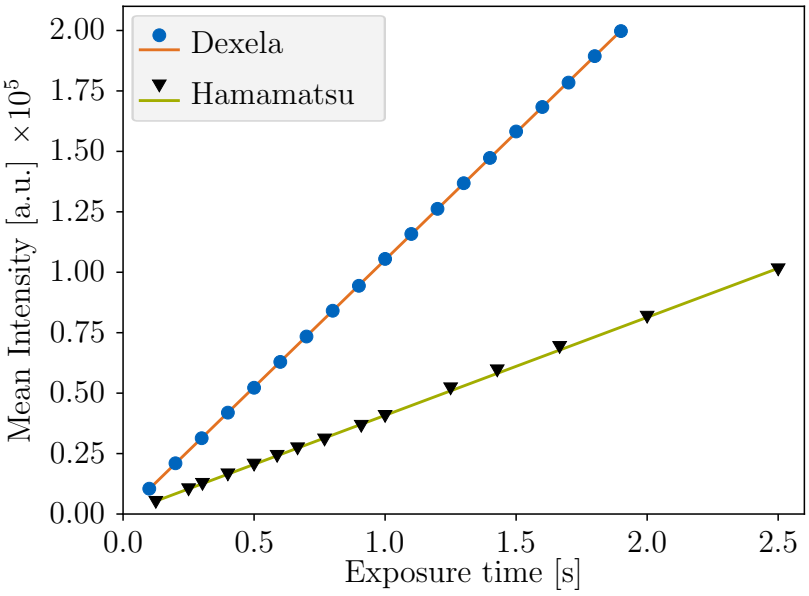

Figure 3.4: Correlation between detected mean intensity and exposure time for both detectors. Both detectors follow a linear behaviour with the exposure time. The Dexela detector is more sensitive to incoming photons, which can be explained on the one hand by the larger pixel size, and on the other hand by a higher quantum efficiency.

to their respective distance to the source in order to consider the local curvature of the wavefront and avoid those drawbacks. The feasibility of a curved grating geometry for the phase and the analyzer grating to decrease the drop of intensity at the outer areas of the grating and to increase the visibility at a compact setup was demonstrated by Revol et al. [Revol, 2011] and Thüring et al. [Thüring, 2011]. In this section, the implementation of a curved grating geometry for this setup is demonstrated and compared with the initial configuration.

Original Grating Configuration

The initial interferometer configuration consists of a source grating G_0 (period $p_0 = 10\,\mu\text{m}$; gold absorber height $h_0 = 35\,\mu\text{m}$), a phase grating G_1 ($p_1 = 3.24\,\mu\text{m}$; nickel height $h_1 = 4\,\mu\text{m}$; $\pi/2$ phase-shift), and an analyzer grating G_2 ($p_2 = 4.8\,\mu\text{m}$; $h_2 = 45\,\mu\text{m}$). The design energy of the system is 23 keV. The thickness of the silicon wafer for G_1 is $d_{\text{wafer},1} = 550\,\mu\text{m}$, whereas the substrate thickness of G_0 and G_2 are $d_{\text{wafer},0/2} = 200\,\mu\text{m}$ each.

Improved Grating Configuration

As a first step to improve the grating interferometer, a new phase grating G_1 was introduced, whereas the source grating G_0 and the analyzer grating G_2 remain with the same respective periods and gold heights. The new binary phase grating G_1, which still induces a phase-shift of $\pi/2$ and has a period of $p_1 = 3.24\,\mu m$, was changed to a grating with a gold height of $h_1 = 2.3\,\mu m$ fabricated on a silicon wafer with a thickness of $d_{\mathsf{wafer},1} = 200\,\mu m$. One of the advantages of a thinner substrate is the lower intensity loss due to absorption in the wafer. In addition, the thinner silicon wafer allows the phase grating to be forced on a radius of 30 cm, which corresponds to the distance between the grating and source. Furthermore, the analyzer grating is bent according to its distance to the source and has a curvature with a radius of approximately 44.5 cm. It should be noted that the handling of curved gratings on silicon substrates is rather demanding, as the bending process implies the risk of breaking the substrate or introduces local deformations to the grating which may cause artifacts in the images. As the distance between source and source grating is only 3 cm, this grating would require a very small bending radius. This small radius implies a very high risk of breaking the grating and therefore bending it poses a challenge. As a consequence, a plane grating is retained here. The interferometer is still operated in the first fractional Talbot order. Forcing phase and analyzer gratings on a radius corresponding to their respective distance to the source compensates the effects of shadowing and shifts the angle of incidence constantly to approximately zero over the full FOV. For this purpose the two mountings for phase grating and analyzer grating were adapted so that a curvature of the gratings could be achieved. A rendering of both grating mountings can be seen in Figure 3.5. A comparison of the plane and improved grating configurations will be presented in the following.

Grating Configurations Comparison

In order to evaluate the performance of the curved grating configuration compared to the plane gratings with respect to the visibility, an image acquisition procedure with four phase steps was carried out by stepping the source grating G_0 over one full period perpendicular to the grating bars. As explained in Section 2.2.3, the intensity is extracted as the mean value of the phase-stepping curve approximated by a sine, whereas the visibility is calculated as the amplitude of the phase-stepping curve divided by its mean. Measurements were executed with no object in the beam. In Figure 3.6, the results of the intensity (A) and the visibility (B) in dependency of the pixel column can be seen.

The orange lines represent the measurements acquired with the thicker, initial G_1 substrate, and plane G_1 and G_2. In contrast, the measurements with the thinner G_1

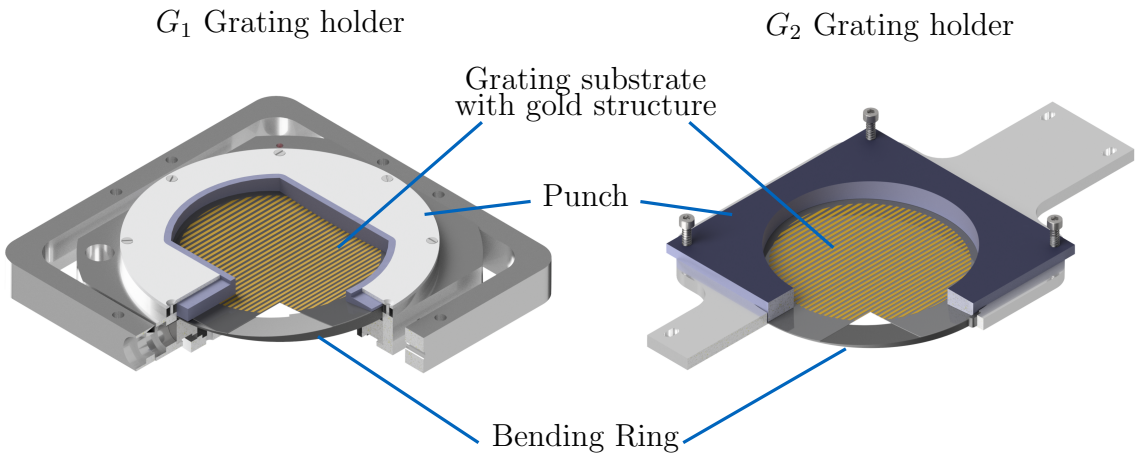

Figure 3.5: Rendering of G_1 (left) and G_2 (right) grating mounting. Both gratings are forced onto a curvature with a radius corresponding to their distance to the source - 30 cm and 45 cm respectively, using a bending ring, and an appropriate counterpart as punch.

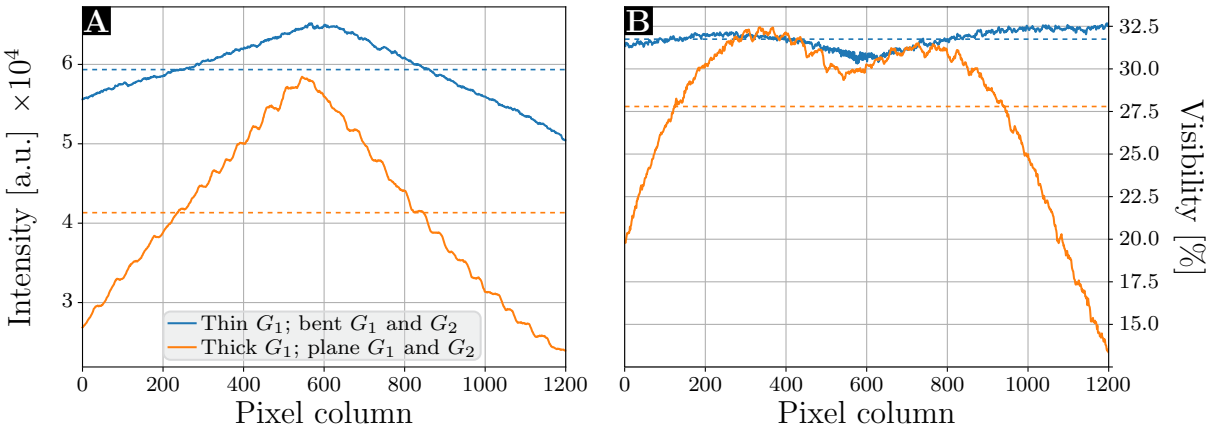

Figure 3.6: Comparison of the visibility and intensity using curved and plane grating configuration. (A) and (B) show the mean transmission and visibility through the interferometer measured at the detector pixel columns, respectively. The dashed lines indicate the mean value over the entire FOV, whereas the solid lines represent the value per column. The lines in blue represent the new and curved grating geometry, and the old plane gratings are represented in orange. The drop of intensity and visibility at the edges is clearly reduced by bending the phase and analyzer gratings. Figure adapted from [Umkehrer, 2019].

substrate and the curved G_1 and G_2 are represented by the blue lines. The solid lines indicate the average over the pixel columns perpendicular to the grating lines, while the dashed lines represent the mean value over the whole FOV. Moreover, all results are summarized in Table 3.3. For both, the plane as well as the bent grating configuration, the measured intensity drops as the distance to the optical axis increases. While the

	Plane	Bent
$I_{0,\mathrm{mean}} \times 10^4$ [a.u.]	4.13	5.94
$I_{0,\mathrm{min}} \times 10^4$ [a.u.]	2.39	5.05
$I_{0,\mathrm{max}} \times 10^4$ [a.u.]	5.82	6.53
$I_{0,\mathrm{min}}/I_{0,\mathrm{max}}$	0.41	0.77
V_{mean} [%]	27.9	31.7
V_{min} [%]	13.3	30.3
V_{max} [%]	32.5	32.6
$V_{\mathrm{min}}/V_{\mathrm{max}}$	0.41	0.93

Table 3.3: Results of the measurements performed with the two different grating configurations. Images were acquired with an exposure time of 1.43 s for each of the four grating steps.

intensity for the plane grating configuration is reduced to approximately 41% of the maximum, the intensity for the bent configuration drops just to 77%. The remaining drop of the intensity offside the optical axis can mainly be explained by the source grating G_0, which is still in plane configuration. Even though the distance from the optical axis is very limited, it contributes to the shadowing and to the drop of visibility by flattening the perfect rectangular profile. However, the intensity measured at the detector benefits from bending the gratings. Moreover, the thinner substrate of the phase grating G_1 contributes to an increased maximum transmission.

The advantage of curved gratings over flat gratings can also be seen in the visibility. The visibility at the edges of the grating reduces to approximately 41% of the maximum. In contrast, for the curved gratings the value for the visibility shows only slight variation and remains close to the value at the optical axis as shown in Figure 3.6. The minimum visibility still remains at 93% of the maximum value. However, both grating configurations show a local minimum of the visibility occurring at the optical axis. With increasing distance to the optical axis the visibility is increasing to the global maximum. This behaviour can be explained by the visibility dependency on the duty cycle. With an increasing duty cycle, which means more absorbing structures and less undisturbed beam path, the visibility increases towards an optimum which depends on the transmission factor [Chabior, 2011; Thuering, 2014]. As the measurements are performed using a conventional X-ray tube with a divergent beam, the effective duty

cycle of the plane source grating is increasing as the distance to the optical axis increases. Therefore, one would expect the visibility to increase to a maximum at the edges of the gratings. However, after the increase the visibility drops to a minimum at the edges - at least for the plane configuration. The explanation for this effect needs several factors to be considered. First, the visibility and therefore the performance of the interferometer depends on the energy of the X-rays. As we are dealing with a polychromatic X-ray source, the total visibility is the result of the spectral visibility. This implies that different X-ray energies contribute to differing extents to the total visibility. X-rays pass through the interferometer in plane configuration at the outermost position in the FOV incident approximately with an angle of $\alpha = 4.1°$ relative to the grating lamellae (see Eq. 3.5). With the specifications of the analyzer grating height, period, and duty cycle, the critical angle where X-rays are able to pass the grating undisturbed is $\alpha_C = 3.1°$. Consequently, the X-rays do not induce a binary intensity modulation but constant absorption with additive trapezoidal intensity modulation. This finally results on the one hand to a hardened X-ray spectrum due to strong absorption towards the edge, and on the other hand to a decreased visibility caused by the reduced intensity modulation. Additionally, the stabilizing resist bridges between the absorbing lines are leading to a reduction of the visibility. Finally, as mentioned earlier, the inappropriate phase shift caused by an increased distance between phase and analyzer grating results in a reduced visibility. All these drawbacks can be neglected for the curved grating geometry, resulting in a constantly high visibility over the entire FOV.

3.3 Data Acquisition and Image Processing

3.3.1 Data Acquisition

In general, the available measurement time for *in-vivo* experiments is limited due to dose delivery constraints and anesthesia. In order to obtain images of the highest achievable quality in this limited time, data acquisition must be as efficient as possible. The stepping of the grating or rotation of the gantry is very time consuming and takes up a large fraction of the total acquisition time, and consequently needs to be reduced to increase the efficiency of use of the available measurement time. The phase-stepping routine requires at least the image acquisition at three different grating positions for the processing. However, using three grating steps is prone to artifacts, and thus, measurements were executed at the lower limit for stable performance using $n = 4$ or $n = 5$ grating steps for plane or bent grating configuration, respectively. To ensure satisfying image quality and to reduce the effect of undersampling for the SIR algorithm, a sufficient number of angular projections N is needed. Considering filtered

backprojection, one would need at least 943 angular projections for a FOV of approximately 600 pixels in horizontal direction to satisfy the Nyquist criterion as stated in Eq. 2.71. However, using the SIR algorithm, the number of angular projections could be empirically reduced with still sufficient quality.
The image acquisition is performed in a step-and-shoot acquisition mode with the detector being operated in a continuous image read-out mode with fixed image frames. A scheme of the detector readout behavior for one angular projection without delay parameters can be seen in Figure 3.7. In previous software versions, several delay parameters were implemented to add a pause after movement and consequently to ensure the image acquisition without vibrating gratings and thus induced image artifacts. Due to a software update and the implementation of automatically skipped image frames when motion takes place, both delays (piezo delay and gantry delay) have in the meantime become obsolete. As an example, the image acquisition is depicted with three grating steps. The length of one image frame is defined by the integration time. Every image frame, which is affected by any movement of gantry or grating, or is influenced by a delay time, is skipped. In Table 3.4, the different data acquisition protocols are given for both the Hamamatsu and Dexela detector.

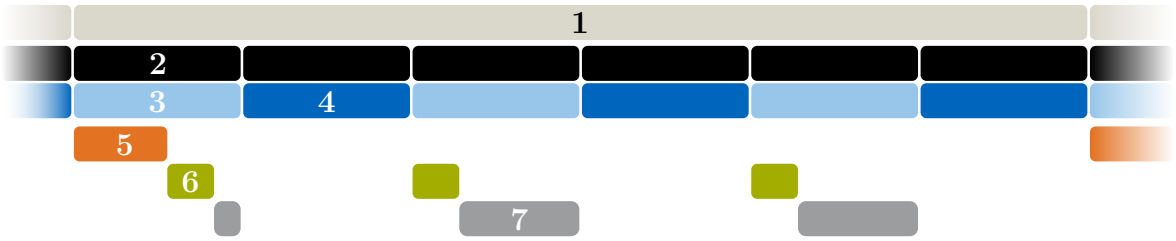

Figure 3.7: Scheme of the acquisition procedure for one single angular projection including three grating steps. 1. Full angular projection, 2. Detectors integration period, 3. Skipped image acquisition due to movement, 4. Image acquisition for measurements, 5. Gantry rotation, 6. Grating movement, 7. Dead time and waiting till next frame.

3.3.2 Scanner Performance

In order to investigate the upgrades and to evaluate the effect of the optimized setup, CT measurements with the previously introduced 3D printed mouse phantom were performed with plane and curved grating configurations. The data were acquired using the respective short-time acquisition protocols as introduced in Table 3.4 and was quantified with a ROI contrast-to-noise (CNR) analysis for different materials. Furthermore, the data acquisition with the Hamamatsu detector is acquired using a 2x2 binning mode in order to slightly accommodate undersampling, whereas the data of the Dexela

Detector	Mode	$t_{\mathbf{Exp}}$	N [#]	n [#]	$T_{\mathbf{Total}}$
Hamamatsu	Radiography	5.0	1	4	40 s
	Short-time CT	1.4	211	4	40 min 14 s
	Medium-time CT	1.4	315	4	60 min 02 s
	Long-time CT	1.4	421	4	80 min 14 s
Dexela	Radiography	1.8	1	5	18 s
	Short-time CT	0.7	303	5	38 min 54 s
	Medium-time CT	0.7	455	5	58 min 24 s
	Long-time CT	0.7	609	5	78 min 18 s

Table 3.4: Acquisition parameters for *in-vivo* X-ray radiography and CT executed with the small-animal prototype dark-field and phase-contrast CT setup. The acquisition parameters for both detectors are listed with the exposure time t_{exp}, the number of angular projections N, the number of grating steps n, and the total acquisition time T_{Total}.

is reconstructed unbinned. The image processing of the raw data was performed using the previously introduced EM algorithm. In order to guarantee equal reconstruction conditions and to solely investigate the influence of the changed hardware including adaptions to the acquisition protocol, the CNR analysis was done on FBP reconstructions instead of SIR. Exemplary axial slices of the reconstructed volumes of attenuation (top row) and dark-field signal (bottom row) for both grating configurations acquired with both detectors can be seen in Figure 3.8. In (A) and (B), the effect of undersampling can be observed at the outer areas of the sample and the sample bed. In contrast, as the number of angular projections could be increased using the Dexela detector, streak artifacts induced by undersampling can be neglected, as one can see in (C). Moreover, the homogeneity of the sample increases from (A) to (C), whereas no loss of resolution can be observed, even though the pixel size is increased with the Dexela detector. In addition, the visual appearance of the reconstructed volumes of the dark-field signal improves from (D) to (F). The positive effect of bending the analyzer and phase grating can be observed in (D) and (E). From those two images it is obvious that the images are still noisy which originates from the nature of the dark-field signal but in (E) the volume appears more homogeneous and edges appear sharper. Furthermore, the effect of the new detector allowing for an increased number of projections can be observed by comparing (E) and (F). The noise level of the reconstructed slice is further decreased, which significantly improves the visibility of small-angle scattering structures such as the earplug.

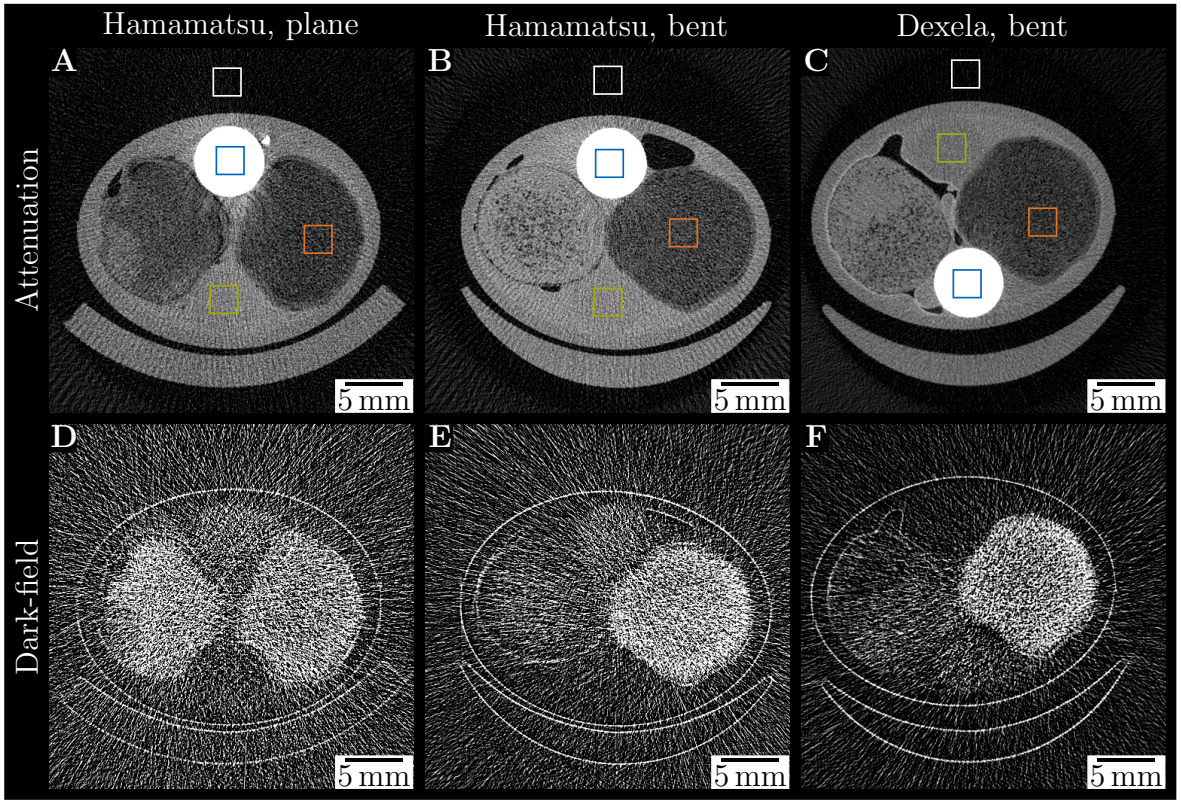

Figure 3.8: Comparison of the mouse phantom measurements. Phantom measurements were performed with the Hamamatsu detector (A, B, D, E) and the Dexela detector (C, F) using plane grating configuration (A, D) and curved grating configuration (B, C, E, F). The images are scaled consistently within the same modality and all images were scaled for maximum detail visibility. ROIs for the CNR analysis are indicated by the colored rectangles: PMMA rod (green), earplug (orange), PVC rod (blue), and the background intensity (white). The images were acquired using the respective short-time acquisition protocol introduced in Table 3.4.

In order to quantify those results, a CNR analysis is performed. The ROIs for the CNR analysis in the individual features (PVC rod (blue), PMMA rod (green), earplug (orange)) are indicated by the rectangles. The CNRs were calculated using the mean value (S_i) and standard deviation (σ_i) of the respective feature and the background (white rectangle) as reference using the conventional attenuation signal (ATT) as well as in dark-field image (DFI) according to

$$\mathrm{CNR} = \frac{|S_i - S_j|}{\sqrt{\sigma_i^2 + \sigma_j^2}}. \tag{3.6}$$

Material	Configuration	CNR_{ATT}	CNR_{DFI}
Earplug	Hamamatsu, plane	1.11	0.46
	Hamamatsu, bent	1.59	0.69
	Dexela, bent	2.12	0.90
PMMA	Hamamatsu, plane	12.88	0.19
	Hamamatsu, bent	14.75	0.22
	Dexela, bent	23.08	0.25
PVC	Hamamatsu, plane	2.91	0.09
	Hamamatsu, bent	3.53	0.04
	Dexela, bent	5.63	0.07

Table 3.5: Results of the CNR analysis, which was performed with the two different grating configurations and two different detectors. All images were acquired using the respective short-time data acquisition protocol.

To improve statistics, the mean and standard deviation were analyzed over the average of 90 adjacent slices. The results of the CNR analysis are listed in Table 3.5. The CNR presented values clearly demonstrate that the new grating configuration with the bent gratings represents an improvement over the plane gratings. When comparing in a first step the CNR_{ATT} values between the plane and bent grating configuration of the Hamamatsu detector clear improvements for all features can be observed. The CNR values for the earplug, PMMA rod, and PVC rod is increased by 43%, 14%, and 21%, respectively. Moreover, for the dark-field signal the most relevant CNR value is the value of the earplug, which is increased by 50% just by bending the gratings. The weak beam-hardening induced dark-field signals of the respective rods do not have much relevance in this context. By extending the consideration to the bent grating configuration with the Dexela detector the further improvement by changing the detector can be seen. Again, the CNR_{ATT} for the earplug, PMMA rod, and PVC rod increase by 33%, 56%, and 59%, respectively. In addition, the CNR_{DFI} value of the lung phantom is raised by 30%. This positive effects can be explained by the increased total flux and therefore a reduced effect of the constant readout noise especially at the edges of the angular projections and a homogeneous visibility over the whole ROI. Furthermore, the higher sensitivity to incoming photons as well as the slightly increased pixel size influences the CNR positively. As a result of the modifications, the crucial CNR values could be increased by a factor of two compared to the initial values.

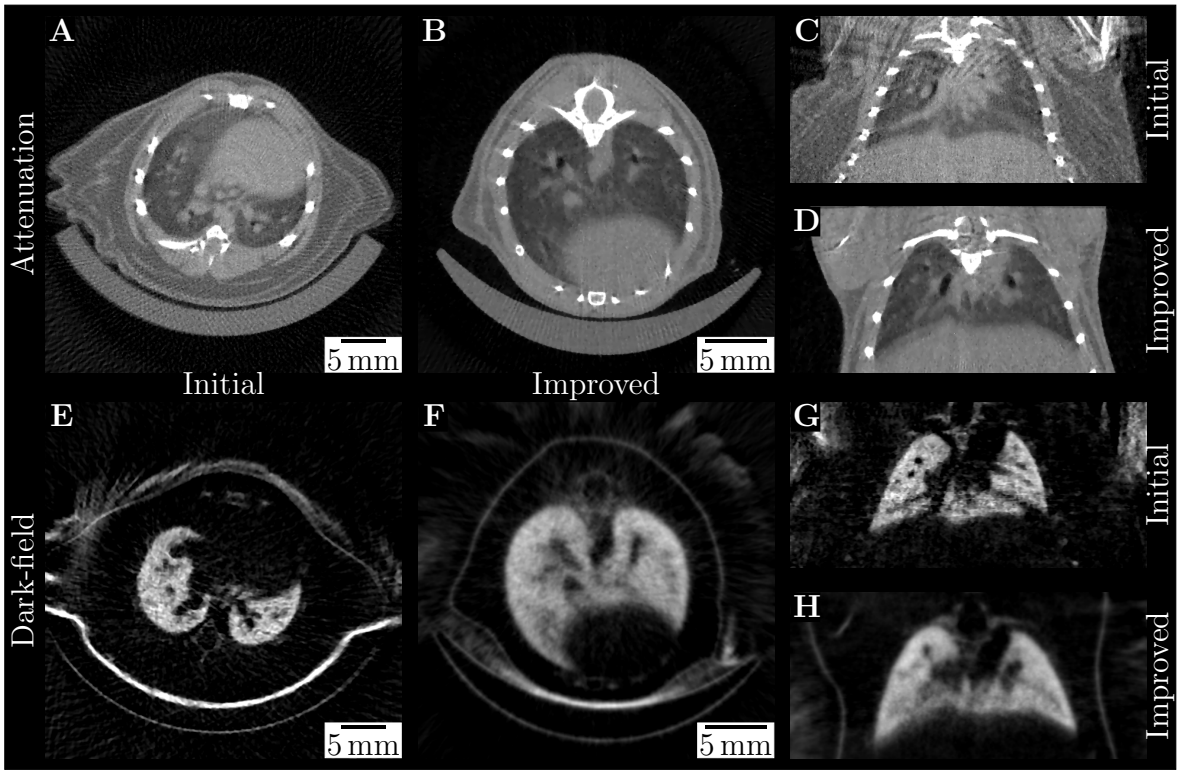

Figure 3.9: Comparison of the *in-vivo* measurements. Exemplary slices of attenuation (top row) and dark-field (bottom) CT using the initial (A, C, E, G) and improved (B, D, F, H) setup configuration. All figures are scaled for best visual appearance and consistent within the respective modality. The scalebars are valid for the respective setup configurations and contrast modalities. Figure partly adapted from [Umkehrer, 2019].

Furthermore, in order to illustrate the influence of breathing and heartbeat during image acquisition, which cannot be realized performing *ex-vivo, in-situ* or phantom measurements, a comparison of *in-vivo* measurements is also presented. These CT measurements were carried out within the framework of other animal studies and not with the purpose of emphasizing the optimization of the setup. Figure 3.9 provides an overview over representative CT reconstruction slices of healthy mice for the conventional attenuation (top row) and the dark-field signal (bottom row) in axial (A, B, E, F) and coronal (C, D, G, H) direction acquired with the initial (A, C, E, G) and the optimized (B, D, F, H) setup. The data were acquired with the respective short-time acquisition protocol as presented in Table 3.4. For comparison, both data sets were processed and reconstructed using the same parameters. Reconstruction was performed using the SIR algorithm with parameters optimized for each modality individually, but consistent within the data sets. As one can see, the optimized setup and adapted data acquisition protocol leads to a reduction of undersampling artifacts in the

conventional attenuation signal, without increasing the total exposure time or losing resolution. Compared to the reconstruction with the initial scanner configuration, the sharpness of the border is preserved whereas the volume appears much more homogeneous and less artifactual so that small features can be identified with high certainty. The improved image quality is also observable for the coronal slices. The grainy and noisy patterns could be considerably reduced using the optimized setup. The improvements are also clearly visible in the reconstructed volumes of the dark-field signal. The borders of the lungs appear much smoother, sharper, and the lung itself appears more homogeneous in the axial slice and coronal slice. Due to the significant improvements of the image quality using the upgraded setup, lung diseases can be diagnosed with a higher sensitivity and specificity, especially when exploiting the dark-field image.

3.4 Summary & Discussion

The aim of this section was to optimize the prototype dark-field and phase-contrast CT measurements. For this purpose, rebuilding measures on the hardware side of the scanner were accomplished. As a first step to optimize the setup, a Dexela flat panel detector replaced the initial Hamamatsu flat panel detector (Hamamatsu, Japan). Even though the new detector features a slightly higher pixel size, and the Siemens star measurements revealed a marginally lower resolution, this has no major negative effect on the image quality of the reconstruction volumes. This can be explained by the fact that during *in-vivo* data acquisition, the mice breath freely and the image is recorded over more than one breathing cycle and heart beat of the mouse. This natural movement of the thorax leads to a natural blurring of the lung anyway. In order to avoid this in future studies, the mice needs to be ventilated during the measurements, and the data acquisition must be triggered according to the ventilation. For this purpose, the installed airway connection could be used not only for the ventilation but also for the anesthesia. In addition, gas anaesthesia would reduce the restrictions in the application of the anaesthetic, allowing a longer total measurement time without increasing the risk of harming the animals. Moreover, the new detector systems allows the exposure time per projections to be halved. The shortened exposure time, additionally, allows for triggering the measurements in future studies. In addition to that, the gained time per projection could be used in order to improve the number of angular projections per CT measurements, this has a major benefit to the image quality of the reconstructed volumes.
As a second step to improve the existing setup, the configuration of the grating interferometer was optimized. The phase grating as well as the analyzer grating were bent with a radius of curvature according to their respective distance to the source to reduce the drop of intensity and visibility offside the optical axis. Bending the gratings

ensure a perpendicular angle of incidence of the X-rays over the whole FOV, which avoids the occurrence of this negative effect and finally leads to an improvement in the image quality. Furthermore, by the installation of a new phase grating, fabricated on a thinner silicon substrate, the flux recorded by the detector could be increased. Even though the interferometer could be improved by those measures, there are still some subjects which could be addressed: The bending of the remaining flat source grating. However, as the distance to the source is very short, this is very crucial. A solution to overcome this could be to use a grating substrate of a more flexible material, such as graphite or polyimide [Koch, 2017; Schröter, 2017]. Alternatively a plane grating with a divergent grating structure could be tested. This implies that during the fabrication of the grating no parallel beam but cone beam is used for irradiating the photosensitive resist. Consequently, a perpendicular angle of incidence over the whole FOV is guaranteed.
As *in-vivo* measurements includes a limited total measurement time due to injection-based anesthesia or dose restrictions, the data must be acquired in the most effective and reliable way. In this context effective means that the highest image quality is received after volume reconstruction, whereas reliable implies that the measurements are stable in the sense of avoiding artifacts, and reproducible. The modifications of the hardware of the setup allow for adaptions of the data acquisition protocol. The exposure time for each projection could be reduced by more than a factor of 2, whereas the number of grating steps per angular projections has to be increased from $n = 4$ to $n = 5$. In total, the the number of angular projections could be increased by approximately 50%. To bring this kind of measurements more towards clinical environment, further investigation on alternative (single-shot) acquisition and reconstruction schemes should be focused on. First approaches already showed the feasibility of single shot techniques, such as the sliding window or IBSIR approach. However, further investigations must be performed in order to estimate or forecast future issues.

X-ray Dark-Field and Phase-Contrast Imaging of Transplanted Lungs 4

X-ray dark-field radiography has already shown several promising preclinical applications for the diagnosis of pulmonary diseases like pulmonary emphysema or pulmonary carcinoma [Yaroshenko, 2013; Scherer, 2017]. In contrast, an assessment of the preclinical potential of using phase-contrast imaging has not yet been evaluated. For this purpose, in this chapter an in-vivo application of phase-contrast radiography for the detection of bronchial pathologies, such as bronchial stenosis or bronchial truncations, occurring after murine lung transplantation will be presented for the first time using a conventional X-ray source. Please note that this chapter has been published under Umkehrer et al. [Umkehrer, 2020a].

4.1 Motivation

Several pulmonary diseases such as mucoviscidosis, COPD, or idiopathic pulmonary fibrosis cause an irreversible destruction of the lung and alveolar structure in advanced stages. Lung transplantation is often the last remaining therapeutic option to improve quality of life, increase expectancy of life, or even saving a patient's life, especially when conservative therapeutic approaches such as medication promise no improvement. A differentiation has to be made between different types of lung transplantation: Lobe transplant, single lung transplantation, bilateral lung transplantation, or a combined heart and lung transplantation. As reported by the International Society for Heart and Lung Transplantation, the total number of adult lung transplants has increased continuously between 1985 and 2017 to a total number of 4452 in 2017 [Chambers, 2017; Chambers, 2019]. Compared to other solid-organ transplantation such as kidney, liver, or heart, lung transplantation has the poorest long-term survival rate, which can be explained by the development of chronic rejection processes [Royer, 2016]. Moreover, complications such as infection, graft failure, acute rejection, as well as bronchiolitis obliterans syndrome (BOS), are common after the transplantation affecting the short-term survival [Chambers, 2017]. Improvements in lung preservation, surgical technique, and perioperative management of the recipient have dramatically decreased the frequency of such complications [Hertz, 2002]. Nevertheless, difficulties such as

pneumo- or haemothoraces still occur immediately after surgery and complications affecting the respiratory system are frequent post-transplant risks. The most common airway complication besides anastomotic dehiscence, infections or fistulas is bronchial stenosis with a frequency varying between 3.5 to 32% [Santacruz, 2009; Kroegel, 2011; Mahajan, 2017; Samano, 2009]. Typical symptoms of a bronchial stenosis are cough, dyspnoea, or recurrent pneumonia, but also a decline in lung function. The standard of reference for the diagnosis in clinical routine is flexible bronchoscopy, which has some limitations, as it only provides limited information on the stenosis length and the patency of distal airways [Santacruz, 2009]. However, several studies have shown that CT imaging provides an accurate assessment of the anastomotic site, an accurate representation of bronchial stenosis, and an excellent assessment of stent positioning [Soyer, 1997], which in turn means increased radiation exposure for the patient.
A hypothetical approach to the identification and diagnostic of bronchial pathologies with reduced radiation exposure could by achieved by using a Talbot-Lau-interferometer. Both of the additional contrast modalities to the conventional absorption contrast provided during image acquisition has a benefit for thoracic imaging. Differential phase-contrast imaging is ideal for the depiction of different types of soft-tissues occurring at the interfaces around the airways and provides information about refraction in the sample. X-ray dark-field imaging is able to quantify the amount of small-angle scattering of sample structures below the physical pixel size which occurs in the lung at the interfaces between air and tissue. Consequently, grating-based dark-field imaging is ideal for imaging the thorax [Schleede, 2012; Bech, 2013] and allows for observation of structural damages in lung tissue caused by pulmonary disorders by changes in the signal intensity with high sensitivity. Recent studies with *in-vivo* mouse models demonstrated promising potential in detection of pulmonary disorders like emphysema or fibrosis and gain functional information about the ventilation of the lung using X-ray dark-field radiography [Yaroshenko, 2013; Meinel, 2014; Hellbach, 2015; Hellbach, 2017], whereas the value of the phase-contrast radiography, which has the potential to visualize and differentiate different kind of soft-tissues within a sample, has not been classified for examination of the lungs. In this chapter, a qualitative study on the phase-contrast signal using radiography was assessed for the first time with regard to its usability for imaging of the lungs and respiratory tract. The goal of the present study is to evaluate the diagnostic value of X-ray phase-contrast imaging for diagnosing of bronchial pathologies in mice. This would furthermore offer the opportunity to visualize pathologies of the bronchial system using conventional radiography and therefore potentially saving exposed dose compared to a CT measurement.

4.2 Small-Animal Left Lung Transplantation

All animal experiments were conducted under strict governmental and international guidelines and were approved by the local government for the administrative region of Upper Bavaria, Germany (project 55.2-1-54-2532.120.2015). The ethics committee reviewed the application according to §15 TSchG German Animal Welfare Law. This section describes the surgical procedure of the lung transplantation according to the publication of Smirnova et al. [Smirnova, 2019]. For the study, a total of $n = 102$ 8-12 weeks old male mice were used. Thereby $n = 51$ mice served as donors and $n = 51$ mice severed as recipients. Donors were anesthetized with an intraperitoneal injection of ketamine/xylazine. The bronchus, pulmonary vein, and pulmonary artery were carefully separated one from the other with blunted forceps, prior to cuffing with, respectively, 20-, 22- and 24-gauge cuffs. The recipient mice were anesthetized with a mixture of medetomidine, midazolam, and fentanyl, intubated and connected to a small-animal ventilator at a respiratory rate of 120 bpm and a tidal volume of 300 µL. After opening the chest on the left side between ribs 3 and 4, the native left lung was retracted with a clamp and the hilar structures were carefully separated one from the other with blunted forceps. After the blood and air flow to the left lung had stopped, the cuffed graft pulmonary artery, bronchus, and pulmonary vein were inserted into the recipient counterparts and sutured. After removing the native left lung and all potential air bubbles from the chest, the incision in the chest was closed. Antagonist was applied and the mice were extubated when showing signs of spontaneous breathing.

4.3 Data Acquisition and Processing

The images within this study were acquired with the setup presented in Section 3.1.1. As the measurements were performed before the setup optimization, the detector was the Hamamatsu flat panel detector (C9312SK-06), and the grating interferometer of the scanner consists of the initial grating configuration, i.e. with unbent geometry and the thicker substrate of the phase grating G_1. The images were acquired with four grating steps with an exposure time of 5 s per position, resulting in a total measurement time of approximately 40 s. Reference images were acquired separately with the sample removed from the beam. The X-ray source was operated with a peak voltage of 35 kV and power of 20 W. Subsequently, the images were processed with an EM algorithm as introduced in Chapter 3.1.2 to calculate all three modalities from the images acquired during the phase-stepping procedure. The imaging of all mice was performed shortly after lung transplantation (time point 1 / TP1). Moreover, a subgroup of 27 mice was imaged at a second time point approximately two months later (time point 2 / TP2). During the image acquisition the mice remained in supine position.

4.4 Analysis Measures

Quantitative Signal Analysis

In order to examine the diagnostic value of the phase contrast with this *in-vivo* prototype in detecting bronchial pathologies and correlate this to the decreased ventilation of the lung using the conventional attenuation and dark-field images, a quantitative signal analysis was performed on the respective signals. For this purpose, one mask each for transplanted and native lung were segmented for each mouse and measurement individually. In this study, the native lungs of the recipient mice, that did not undergo transplantation, served as control lungs. The masks were segmented on the basis of conventional absorption images using the software MATLAB and included the free accessible lung parenchyma without the overlaying mediastinum, heart or the diaphragm. Moreover, osseous structures such as the ribs and the spine were segmented automatically using binary erosion and dilation on pre-smoothed absorption images and were excluded from the masks in order to increase the classification accuracy. An exemplary mask of one mouse of the segmented and final ROI is presented in Figure 4.1. Identical masks were applied to the absorption and the dark-field radiography. To further quantify the condition of both lungs, the mean values for both segmented regions were calculated.

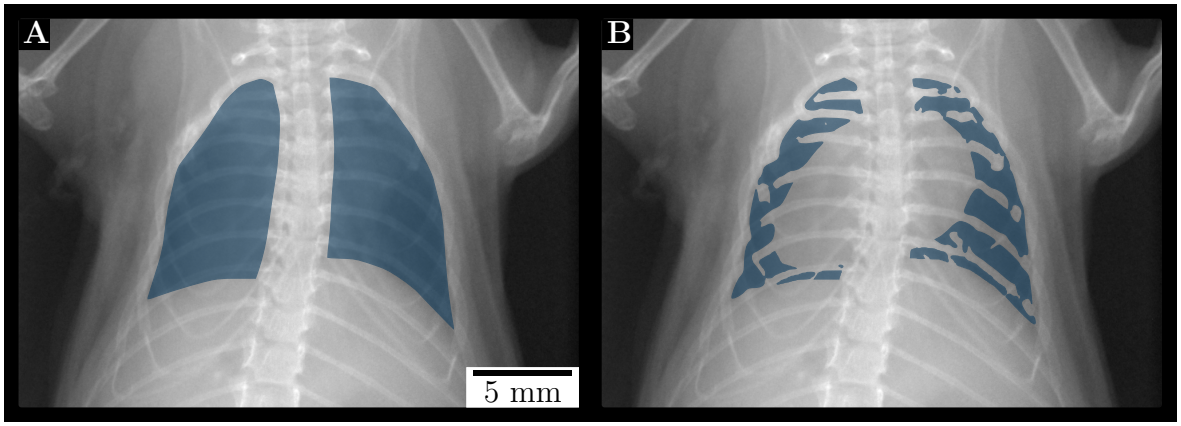

Figure 4.1: Representative example of a segmentation mask. Segmented (A) and final (B) masks with osseous structures and the shadow of the heart removed used for the quantification of absorption and dark-field signal. The pixel marked with blue are used for the calculations. Left and right lungs were quantified separately.

Statistical Analysis

In order to compare the intensities of both conventional transmission signal and dark-field signal of the transplanted and (native) control lungs, the mean values as well as the standard deviations of the signals were calculated. The means were tested for statistical significance using Student's t-test for paired samples.

4.5 Imaging Results

Quantitative Image Analysis – Transmission and Dark-Field Signal Measurements of Lung Parenchyma

This imaging study included the lungs of a total of 46 transplanted mice. All mice were measured for quantitative transmission and dark-field signal analysis at TP1. As four mice developed a left-sided pneumothorax, which can be seen by way of example in Figure 4.2, consequently those mice had to be excluded from the signal analysis.

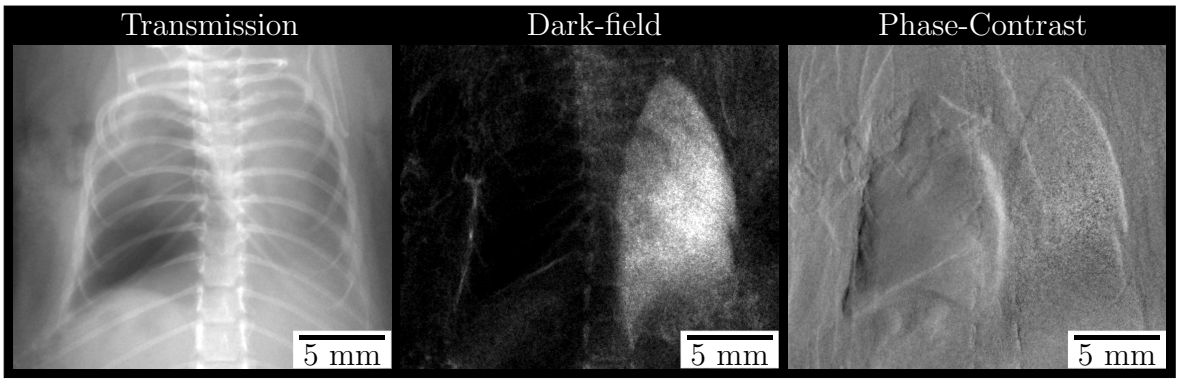

Figure 4.2: Mouse with a developed pneumothorax. Example of one mouse that presented with a unilateral, left-sided pneumothorax after lung transplantation. The pneumothorax is indicated by hypertransparency in the transmission image (left). In the corresponding dark-field image there is no dark-field signal observable (middle). Figure adapted from [Umkehrer, 2020a].

Comparing the dark-field signal of the transplanted (0.681 ± 0.215) with the (native) control lungs (1.475 ± 0.184), a significant loss of signal intensity for the transplanted lungs can be observed ($*p < 0.001$). A significant increase in absorption between the transplanted (0.943 ± 0.078) and control lungs (0.788 ± 0.069) was measured ($*p < 0.001$) for the transmission signal intensity. The comparison of both attenuation (left) and

dark-field signal (right) between transplanted (blue) and control lungs (orange) at TP1 is presented in Figure 4.3.

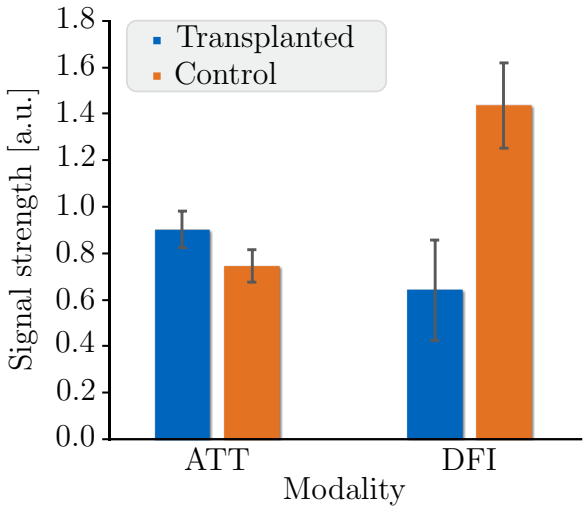

Figure 4.3: Comparison of the transplanted lungs with the control lungs. Comparing the transplanted lungs (blue bars) with the control lungs (orange bars) at TP1, a significant increase in absorption and decrease in dark-field signal intensities of the transplanted lungs could be observed. The signal strength accords to the respective negative logarithm of attenuation and dark-field.

In order to quantify the functionality of the lungs after lung transplantation and to investigate possible improvements, the lungs of a total of 27 mice underwent a second measurement for analysis. Subsequently, the signal derived by the lungs over time were compared between TP1 and TP2. For the transmission signal intensity there was no significant change for the transplanted lungs, comparing TP1 (0.947 ± 0.078) and TP2 (0.932 ± 0.066) ($p = 0.09$). By contrast, a slight but still significant increase ($*p = 0.04$) of dark-field signal intensity for the transplanted lungs could be observed between TP1 (0.656 ± 0.234) and TP2 (0.722 ± 0.251). What should be noted is that when evaluating the signal intensities of the control lungs, a slightly significant decrease in dark-field signal intensity (TP1: 1.507 ± 0.168; TP2: 1.442 ± 0.263; $*p < 0.05$) as well as increase of absorption in transmission images (TP1: 0.789 ± 0.075; TP2: $0,836 \pm 0.067$; $*p < 0.05$) could be observed. The development of the signal intensities over time is presented in Figure 4.4 for the attenuation (left) and dark-field (right) signal.

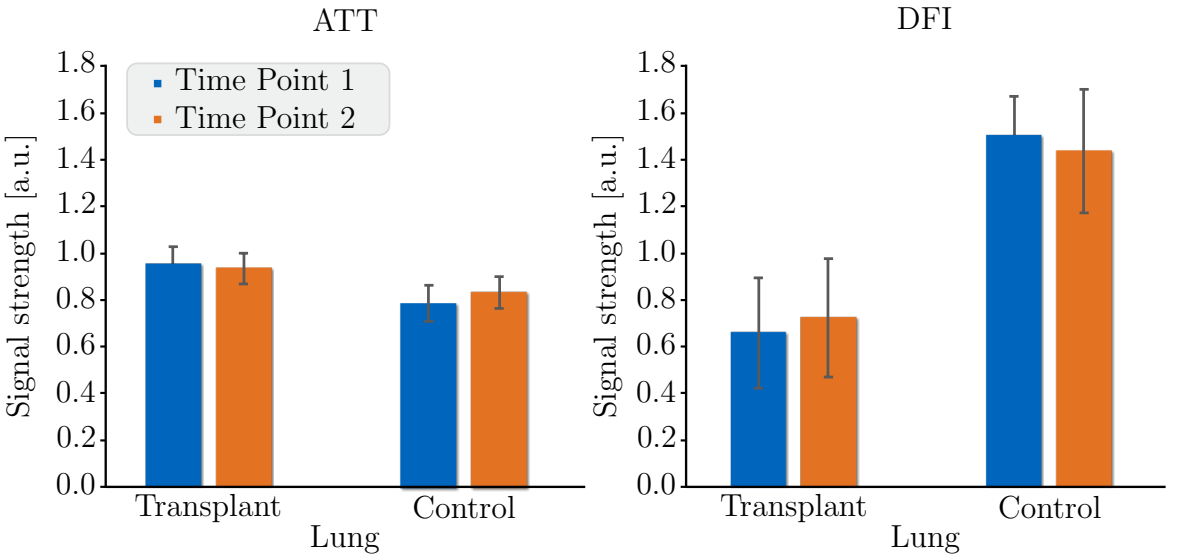

Figure 4.4: Development of signal intensities over time. When analyzing the signal intensities of the transplanted lungs, a slight but not yet significant decrease of absorption was found between TP1 (blue) and TP2 (orange) ($p = 0.09$). Dark-field signal showed a slight, statistically significant increase comparing TP2 with TP1 ($*p = 0.04$). Control lungs showed a statistically significant increase in absorption and decrease in dark-field signal intensities between TP2 and TP1 ($*p < 0.05$). The signal strength accords to the respective negative logarithm of attenuation and dark-field.

Qualitative Image Analysis – Phase-Contrast Imaging of Bronchial Stenosis

When carefully evaluating the phase-contrast images of the transplanted mice at TP1, 24 lungs out of 46 showed decreased ventilation. Moreover, 14 of those 24 lungs presented visible irregularities of the left main bronchus. These irregularities can be related to either a visible stenosis (Figure 4.5 bottom; 4 cases) of the bronchus or a visible bronchial truncation (Figure 4.5 middle; 10 cases). An exemplary bronchus with no pathological anomalies is shown in the top row of Figure 4.5.

A total of 8 mice showed improved ventilation of their transplanted lungs in transmission and dark-field image at TP2, compared to TP1. When taking a closer look at these animals, a decrease of left-sided bronchial irregularities over time could be observed in 6 mice: either were the bronchial parts (Figure 4.6) located distally the cuff visible again or was the degree of stenosis declining (Figure 4.7).

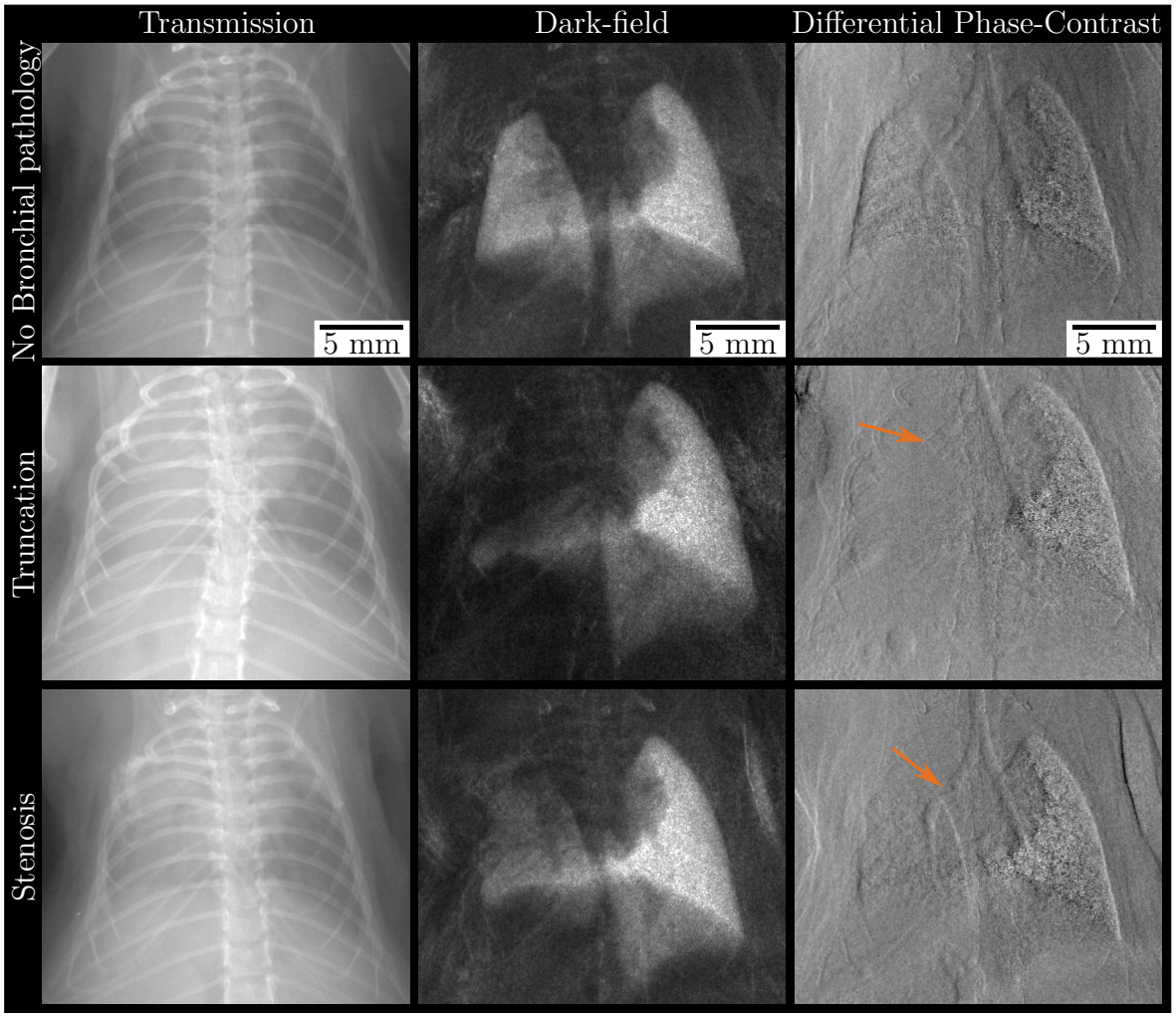

Figure 4.5: Different bronchial pathologies. Mouse without any visible bronchial pathology in the phase-contrast image after left-sided lung transplantation (upper row). Please note that the dark field as well as the transmission image present good ventilation of the transplanted lung. By contrast, the left main bronchus distal to the cuff cannot be identified on the phase-contrast image from the mouse below (orange arrow; middle row), consistent with bronchial truncation. The corresponding dark-field and transmission image of this mouse reveal total atelectasis of the middle and upper parts of the transplanted lung. In case of the third mouse (bottom row), the lumen of the bronchus narrows at the level of the cuff as indicated by the orange arrow. In contrast to truncation, the more distal parts of the bronchus remain present, indicating a stenosis. Ventilation of the left lung is constrained (dark-field image) but not as severe as in case of truncation. Figure adapted from [Umkehrer, 2020a].

4.6 Discussion

Large airway complications are the most important adverse events after lung transplantation, next to primary graft dysfunction, acute rejection, postoperative infection

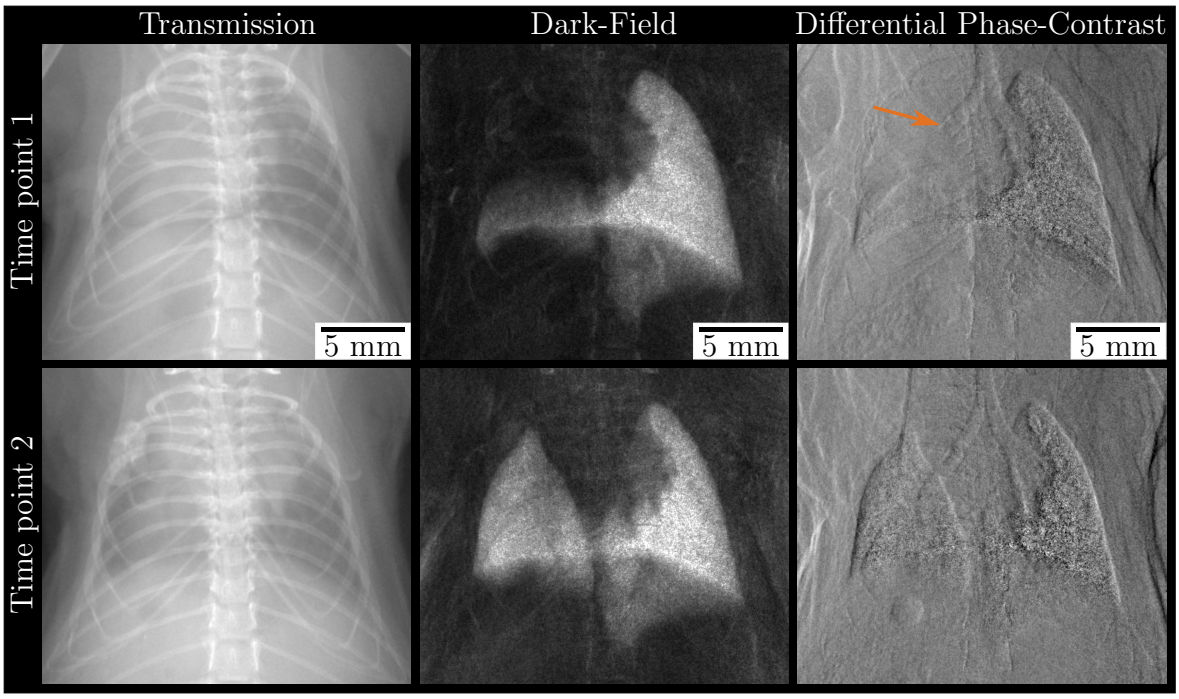

Figure 4.6: Example of improved bronchial truncation over time. A loss of ventilation can be seen in the transmission and much more obvious in the dark-field image at TP1. The corresponding differential phase-contrast image reveals the presence of a bronchial truncation at the level of the cuff. Two month later (TP2) the ventilation of the transplanted lung has increased and the left main bronchus is continuously visible again as the phase-contrast image reveals.

and hemorrhage, as well as vascular anastomotic complications [Kim, 2018]. A central airway stenosis, which may include the anastomosis region, is the most important cause for large airway complications. Within the first year after lung transplantation, up to 15% of all patients develop a central airway stenosis [Shofer, 2013]. Among the complications are bronchial dehiscence, exophytic excessive granulation tissue formation, and tracheo-bronchomalacia [Santacruz, 2009]. Most of these complications, including airway stenosis, can be diagnosed using CT [Semple, 2017]. In contrast to that, conventional transmission radiography presents alterations due to indirect changes of bronchial pathologies such as atelectasis, rather than visualizing the bronchial system itself. Therefore, within this study the hypothesis is proposed that phase-contrast imaging is a useful imaging modality for the diagnosis of pathologies in large airways after lung transplantation, as it strongly enhances the edges of the bronchial system, making it visible with a conventional two-dimensional radiography image for the first time.

When analyzing the signals derived by the transplanted lungs and comparing it with

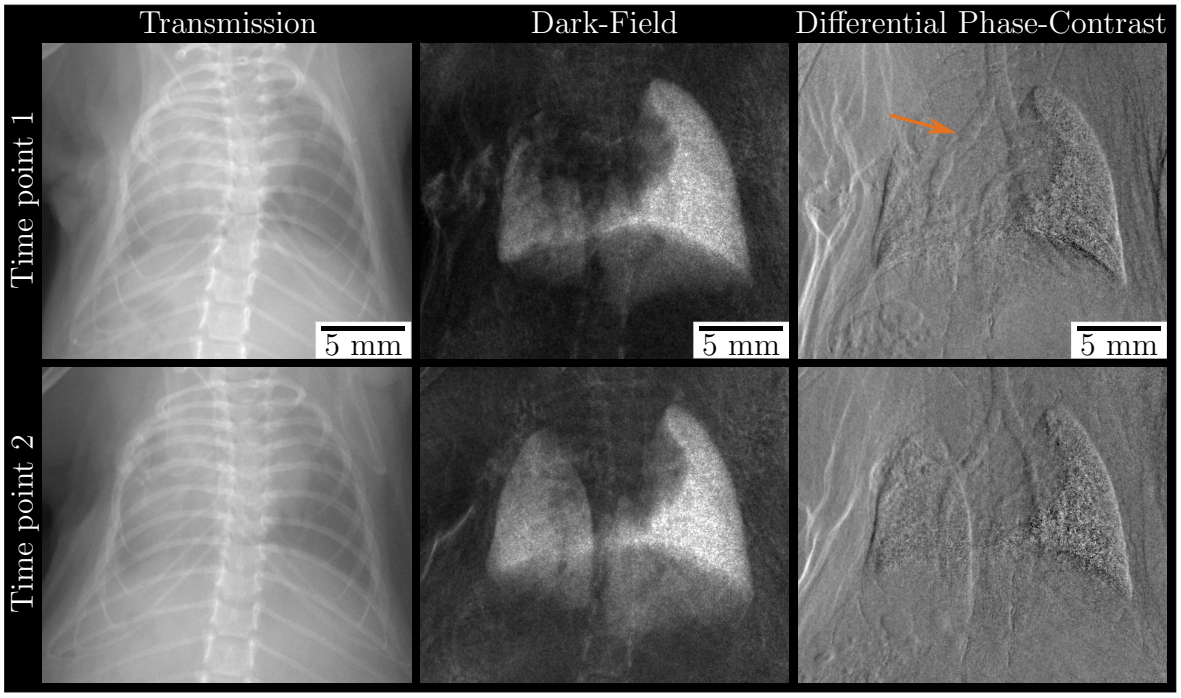

Figure 4.7: Example of decreasing bronchial stenosis over time. At TP1 the phase-contrast image reveals a stenosis of main bronchus at the level of the cuff. Please note that the bronchus distal of the cuff is slightly dilated (1.5 mm). Two months after lung transplantation (TP2) there is no stenosis of the bronchus visible anymore and the lumen of the bronchus distal of the cuff has normalized (1.1 mm). Corresponding transmission and dark-field images show slightly improved ventilation of the left lung compared to TP1.

those of the native (control) lungs, a significant change was detected in both dark-field and transmission images. While the transmission images showed an increase of absorption, the corresponding dark-field images revealed, as expected, a loss of signal intensity. This behaviour is consistent with a decreased proportion of ventilated pulmonary parenchyma within the transplanted lung, and might be caused by several post transplantational pathologies, such as atelectasis due to bronchial stenosis, pleural effusion and hemorrhage, as well as consolidations caused by pulmonary infiltrates. It is important to mention that the changes of signal intensities observed in the transplanted lungs is not necessarily directly linked to any pathology of the large airway, as complications are diverse and multiple pathologic changes may occur simultaneously: Besides large airway pathologies including thrombosis of a bronchial vein or artery, the most frequent and important postoperative complications in animal studies are respiratory infections, pleural effusion, pulmonary edema, and graft rejection. This possibly explains the fact that not all of the lungs revealing a loss of ventilation presented visible bronchial pathologies [Prop, 1984; Khan, 1999].

Two months after lung transplantation (TP2), an overall increase of dark-field signal intensity could be observed, which indicates an enhanced ventilation of the transplanted lungs compared to TP1. Even though no significant change of transmission signal intensity was observed, a slightly decreased amount of absorption was detected, implying better ventilation of the transplanted lungs as well. In the corresponding phase-contrast radiographs, several lungs presenting signal alterations as already described, revealed recurrent bronchial stenosis, which most likely accounts for the improved ventilation. Reversible bronchial stenosis might be caused by bronchial hemorrhage or mucus plugging. Development of scar tissue could rather be a reason for persisting bronchial stenosis, as well as a bronchial dehiscence, e.g. caused by displacement of the cuff. According to the literature, an undersized diameter of the cuff as well as foreign-body reactions caused by the cuff may occur, potentially resulting in a bronchial stenosis or truncation. Moreover, there is a potential risk of twisting of the bronchi after anastomosis, also leading in bronchial truncation [Reis, 1995].
When regarding the signal development over time of the native lungs, an interesting observation can be made: Transmission as well as dark-field images indicated signal changes similar to the transplanted lungs at TP1 - to a very discrete but nevertheless significant extend. One possible explanation for this finding might be that the control lung had to overcompensate for the poor condition of the transplanted lung at TP1 and was therefore hyper inflated. As the transplanted lungs slightly recovered over time, the recipients' native lungs returned to their natural physiological state of capacity [Reece, 2008].
Four animals had to be excluded from the signal analysis as they developed a large left-sided pneumothorax after lung transplantation. According to the literature, bronchial leaks most likely cause post transplantational pneumothoraces [Mizobuchi, 2004].
A major shortcoming of this study could be that there is no external reference standard, as there are neither CT images nor histological examinations of the large airways or the cuff region. However, from a diagnostic point of view it is less important to determine the reason for a bronchial pathology but to show the pathology in the first place. Further examinations based on CT and bronchoscopy would be necessary in any case. Nonetheless, investigations focusing on histopathological changes of the cuff region after lung transplantation are preferable. The conventional radiographs of the recipient's own right lung served as a control, both with regard to the degree of ventilation and the bronchial system. This might be critical, since - as shown with ventilation - the native organ can also be influenced by the transplantation. Further studies of the bronchial system with a strong reference standard are necessary.
Nevertheless, it could be shown that the differential phase-contrast signal is an appropriate and very well suited contrast modality in order to detect bronchial pathologies after lung transplantation, while the dark-field contrast allows for a quantification of the lung ventilation at the same time.

X-ray dark-field CT imaging 5

This chapter contains the preclinical application of dark-field CT imaging for the detection of pulmonary carcinoma. After motivating this topic, the mouse model as well as the sample preparation will be described. To further proof findings obtained by in-vivo measurements using the optimized Skyscan 1190, the results were verified by and correlated to ex-vivo high-resolution micro-CT as well as histology. In addition, a signal analysis was performed by an automated lung segmentation for evaluating the three-dimensional dark-field signal. Please note that parts of this chapter is under preparation to be submitted by Umkehrer et al. [Umkehrer, 2020b]. Figures and text passages in this section may appear identically.

5.1 Motivation

With an estimated amount of nearly 10 million deaths in 2018, cancer is one of the leading causes of death worldwide. Globally, about one in six deaths can be referred to cancer, where lung carcinoma is the leading cause of cancer-related death [WHO, 2018]. If treatment is not commenced in time, the malignant lung tumor, which is often characterized by fast and uncontrolled cell growth in the lung tissue, leads to metastasis in surrounding tissue or other organs. As lung cancer is mostly diagnosed at an advanced stage, the prognosis is usually poor which finally results in an average five-year survival rate of less than 15% in Europe [De Angelis, 2014; Travis, 2011]. In clinical routine, conventional chest radiography is the most common imaging method for the detection of pulmonary cancer or rather thoracal diagnosis in general. Due to overlying osseous structures and the shadow of the heart, or the limitation to two-dimensional information of the three-dimensional specimen, the sensitivity of detecting small nodules is particularly low. A study of the "Early lung cancer action project" in the USA demonstrated that low-dose CT lung screening as a mortality reducing screening program is more sensitive compared to radiography in detecting lung cancer at an early stage, whereas similar numbers of late-stage cancers are diagnosed [NLSTRT, 2013]. These findings are in agreement with several studies analyzing low-dose CT screening [Henschke, 1999; Swensen, 2003; Pastorino, 2003; Gohagan, 2005; IEL-

CAPI, 2006; Wilson, 2008; vKlaveren, 2009]. Nevertheless, it has also been shown that low-dose CT screening may increase the false-positive rate, which may lead to unnecessary further testing and cause patient anxiety [Ali, 2016; Kinsinger, 2017]
In preclinical research, genetically engineered mouse models play an import role for the investigation, treatment and imaging of lung cancer [Meuwissen, 2001; Olive, 2006; Takeda, 2007a; Takeda, 2007b; Kellar, 2015]. Not only new and innovative therapies to treat cancer in studies of lung carcinogenesis benefit from those models, but it is also possible to image the progress and research for new imaging techniques in order to increase the sensitivity [Bidola, 2019]. Currently, absorption-based micro-CT and conventional histology are used in order to track diseases in the lung and analyze changes post mortem. Histopathology is able to visualize structural changes within the tissue. Nevertheless, it is an invasive technique and therefore it is not suitable for longitudinal studies with multiple measurement points. In contrast to that, micro-CT imaging allows for the observation of structural changes over time by multiple imaging. However, using conventional absorption contrast, no information about the functionality of the lung is available.
For an improved assessment of lung cancer, and to compensate the mentioned deficiencies of radiography, a combination of the advantages of the X-ray dark-field imaging with the information about the ventilation and the CT imaging with three-dimensional information of the specimen is presented. Based on the optimization measures from Chapter 3 and the significantly improved image quality for CT reconstructions, the new setup specifications and acquisition protocol allow to investigate the feasibility of detecting tumor nodules with high accuracy. In order to do so, within this study 8 murine lungs were image days after Lewis lung carcinoma (LLC) cells application in addition to 4 control mice. Unfortunately, only one mouse developed lung tumors of resolvable size. This mouse was used to introduce a first specific case study of the correlation of morphological changes of lung tissue caused by tumor growth using *in-vivo* attenuation and dark-field CT measurements, *ex-vivo* attenuation micro-CT measurements, and histology. As a second part within this chapter and based on the CT measurements, an automated lung segmentation algorithm was developed in order to be able to perform signal analysis for different kind of diseases. Also within the LLC study the functionality of all murine lungs is investigated and a quantification of the dark-field signal is performed. Besides the one mouse with developed tumors, other just showed little pathological changes such as atelectasis or bleeding into the tissue which can be seen using a signal analysis.

5.2 Small-Animal Lung Tumor Model

The study included both *in-vivo* and *ex-vivo* imaging. All animal procedures and their care were conducted in accordance with national and international guidelines (EU 2010/63) with approval from the local government for the administrative region of of Upper Bavaria and supervised by the Animal Care and Use Committee of Klinikum rechts der Isar. Animals were housed in standard animal rooms (12 h light/dark cycle, 50-60% humidity, 18 °C - 23 °C temperature, bedding material) in individually ventilated cage systems (IVC Tecniplast, Buguggiate, Italy) under specific pathogen-free conditions with access to water and standard laboratory chow ad libitum. For this study, 12 female 10-14 weeks old C57BL/6N mice (Charles River, Sulzfeld, Germany) were used. Lung tumors were induced using murine LLC cells (ATCC, Virgina, USA) according to literature [Takeda, 2007a; Takeda, 2007b]. For this purpose 1×10^6 LLC cells were injected intravenously in 5 ml/kg body weight 1×Dulbecco's phosphate-buffered saline (DPBS; Gibco, Germany) via the tail vein. For imaging, the mice were anesthetized by injection anesthesia using medetomidine (0.5 ml/kg), midazolam (5 mg/kg), and fentanyl (0.05 mg/kg). The mice were euthanized under deep anesthesia directly after the imaging, and the lungs were excised for *ex-vivo* micro-CT imaging and histological sectioning.

5.3 Histology and Sample Preparation

The staining of the lungs for three dimensional virtual histology was carried out as described in Busse et al. [Busse, 2018]. The freshly excised lungs are placed in a 50 mL Falcon centrifuge tube (neoLab Migge GmbH, Heidelberg, Germany), which is filled with a fixative solution containing 9.5 mL of 4% (vol/vol) formaldehyd solution (Carl Roth GmbH + Co. KG, Karlsruhe, Germany). The formaldehyd solution was derived from a 37% acid-free formaldehyd solution diluted with DPBS (Thermo Fisher Scientific) and 0.5 mL glacial acetic acid (Alfa Aesar, Ward Hill, Massachusetts, USA). The samples are refrigerated for 24 hours and then washed with DPBS for one hour. Each lung is then placed into the staining solution of eosin y (30% (wt/vol); E4382, Sigma Aldrich) for another 24 hours. The lungs were covered completely with the staining solution and could move freely within the sample container. During the incubation time the lungs were kept on an horizontal shaking plate with a rocking of 60 rpm. After staining, the lungs were removed from the sample container and excess staining solution was patted dry by a cellulose paper. The samples were then embedded in 4% agarose in aqua dest. (B. Braun Melsungen AG, Melsungen, Germany) in sample containers.
The stained mouse lungs were dehydrated and embedded in paraffin corresponding

to standard procedures of histological sectioning. First, the samples were dehydrated within several steps. Dehydration began with storing the samples over night in 70% ethanol. On the next day the samples were transferred into 96% ethanol for one hour and cleared in xylol twice for one hour. In order to embed the sample completely in a block of paraffin wax, the lungs were incubated overnight in paraffin wax at 65 °C. The slicing of histological sections was performed using a microtome (Thermo Scientific). Paraffin slices of 5 µm thickness were extracted on histological specimen holders and counterstained with Mayer's sour haematoxylin (Morphisto) according to the manufacturer's staining routine protocol (H&E). All slices were scanned using the Aperio AT2 scanner (Leica) and imaged using the Aperio Image Scope software (Leica).

5.4 Correlation of *in-vivo* Dark-Field CT and stained *ex-vivo* High Resolution CT

The correlation of morphological changes caused by tumor growth after the application of LLC with changes in the signal intensity was investigated using two techniques and setups. First, *in-vivo* dark-field radiography and CT measurements were performed, followed by the acquisition of *ex-vivo* micro-CT analysis of the excised and eosin stained lungs. Finally, the images were verified with histology of serial sections to prove findings.
The *in-vivo* imaging was acquired using the small-animal dark-field and phase-contrast CT Skyscan 1190, as introduced and optimized in Section 3.1.1. Within this study, the setup was used to acquire radiography as well as CT images. As *in-vivo* measurements were performed, the temperature of the mice was tracked, and the warm-air fan was used to heat the body if necessary via the physiological monitoring system. Furthermore, fresh air was pumped into the system via an external air connection. The image acquisition protocol is listed in Table 5.1.
For the *ex-vivo* measurements of the lungs, the commercial laboratory micro-CT system Xradia Versa 500 (ZEISS, Oberkochen, Germany) was used. It is equipped with a tungsten X-ray micro-focus source with a focal spot size which varies according to the current but is below 5 µm. The detector system consists of a cooled CCD camera, coupled to several objective lenses which are switchable based on the requirements. The pixel size of the CCD camera is 13.5 µm and the active area consists of 2048 × 2048 pixel. All measurements were performed using the 0.39× -objective lens with a voltage of 50 kV and a current of 74 µA. The source-to-sample and sample-to-detector distances were adapted to position the entire sample in the optimal FOV. A total amount of 1601 projections were acquired over 360 degrees in each scan. A binning of 2 × 2 pixels was used to enable an image acquisition with a reasonably short exposure time of 5 s per projection, whereas the image reconstruction was performed without additional bin-

ning. The effective pixel size resultes in 22.1 µm. For more details on the micro-CT setup the reader is referred to read [Bidola, 2017].

	Projections [#]	Steps [#]	Exposure time [s]	Scan time
Radiography	1	5	1.8	17 s
In-vivo CT	303	5	0.7	39 min

Table 5.1: Acquisition parameters for the *in-vivo* X-ray radiography and CT measurements performed with the small-animal prototype dark-field and phase-contrast CT setup

In-vivo Dark-Field Radiography

Exemplary absorption and dark-field radiographies of a murine thorax with a pulmonary carcinoma, recorded with the acquisition parameters listed in Table 5.1 labeled with "Radiography", are presented in Figure 5.1. The investigated mouse was imaged 11 days after the application of the LLC cells. Unfortunately, this was the only mouse with tumor cell clusters with a resolvable size. However, in case of the conventional transmission radiography, structural changes caused by tumor growth within the lung are difficult to localize and differentiate due to overlying structures like the ribcage, spine, heart, and diaphragm. In contrast, the influence of overlying osseous structures or the heart in dark-field imaging is much smaller, since the signal from the lungs dominates in the thoracic region. Despite this, the dark-field signal induced by the fur of the mouse superimposes the signal obtained by the lungs. In dark-field radiographies, tumors appear as dark voids - caused by poor scattering ability - within the homogeneous strongly scattering lung signal. As indicated in Figure 5.2, multiple scattering at the interfaces between tissue and air cause a strong dark-field signal within healthy lung tissue. In contrast, structural pathological changes such as tumor growth lead to a reduction of the interfaces, resulting in a decreased dark-field signal. A decreased dark-field signal could be observed in the upper part of the left lobe by a dark-field experienced radiologist, as indicated by the respective left arrows. However, it cannot be determined with certainty whether this is solely caused by the shadow of the heart or whether there is some additional pulmonary pathology. As presented in the following, this mouse developed a tumor nodule in the middle of the lobus caudalis (Figure 5.1: respective right arrows). As shown in Scherer et al. [Scherer, 2017], small tumor lesions induce only small deviations to the optical density compared to the surrounding healthy lung tissue, which renders a clear identification of small nodules extremely challenging. Moreover, several issues render the unambiguous diagnosis and detection of the developed tumors with a high sensitivity using dark-field radiography impossible:

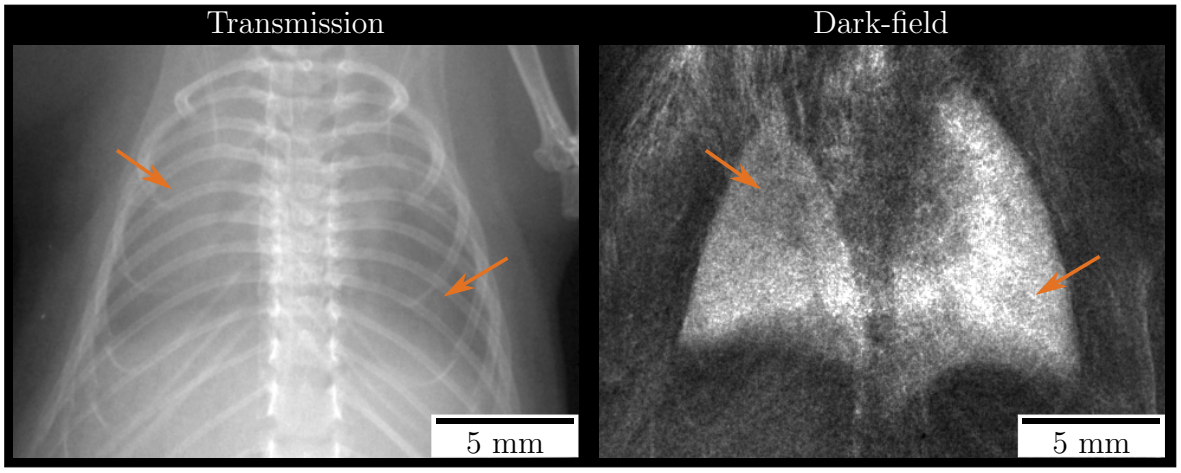

Figure 5.1: Typical radiography of *in-vivo* transmission and dark-field imaging for the detection of lung nodules. Overlying structures like the bones, spine, diaphragm, heart (left, transmission), and the fur (right, dark-field) impede the diagnosis and a localization of the tumors, which are indicated by the arrows, with high sensitivity is not possible. Both figures are color-scaled for best visual appearance.

1. **Small amount of developed tumor nodules.** In contrast to the already mentioned tumor study using K-ras line, where all mice developed numerous tumor nodules, here only a few solid tumors on one mouse could be identified.

2. **Limited spatial expansion of the tumor nodule.** The presented tumors in the advanced stages of the disease partly showed a diameter of 5 mm in width which corresponds to more than the half width of the lobe. In contrast, the tumors in this study had a diameter of below 2 mm.

3. **Unfavorable location of the tumor.** Moreover, the location of the tumor in this study is very unfavorable for a radiography study. The biggest tumor is located in the middle of lobus caudalis, whose projected depth for a coronal direction radiography is the maximum of the lung.

All together, the strong dark-field signal induced by the surrounding healthy tissue overlaps the reduced dark-field signal caused by the tumor nodules.

Analysis of Lung Tumors using Multi-Modality CT Imaging

Following the acquired radiography, an *in-vivo* CT measurement was performed. The acquisition parameters are presented in Table 5.1 labeled with "*In-vivo* CT". From

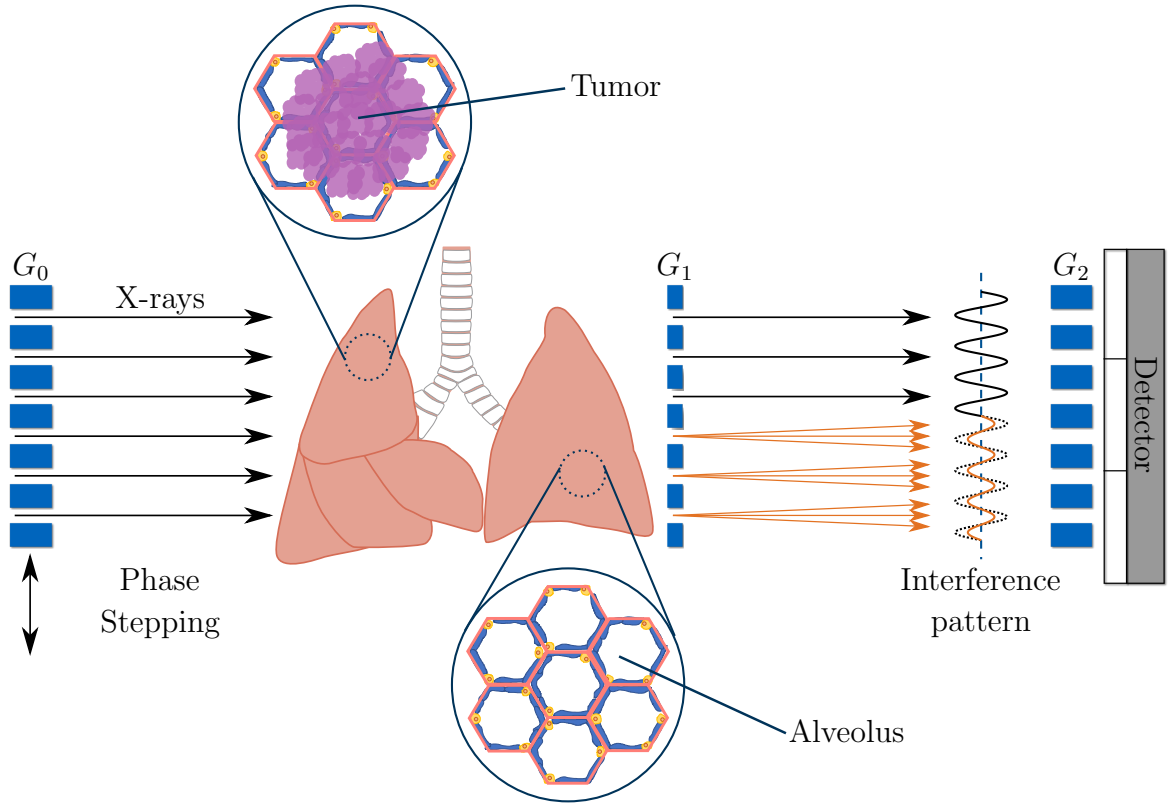

Figure 5.2: Scheme of *in-vivo* small-animal dark-field imaging with an tumor inside the lung. Due to multiple scattering at the interfaces of tissue and air, the healthy alveolar lung tissue causes a strong dark-field signal (bottom). Structural pathological changes in the lung tissue, e.g. caused by a reduction of the number of alveoli or invaded alveoli are observable by a decreased dark-field signal (top) [Scherer, 2017]. The information of the small-angle scattering can be retrieved by imaging at several phase-steps and process the raw images.

three different levels representative slices of the *in-vivo* attenuation and *in-vivo* dark-field measurements, eosin-stained high resolution *ex-vivo* measurement, and histology of H&E stained sections are presented in Figures 5.3, 5.4, and 5.5, respectively. The images on the bottom represent the region of interest marked with the blue box on the respective overview image of the top row. Starting from Figure 5.3 to Figure 5.5, the axial slices from cranial to caudal direction is presented.

Figure 5.3 shows the upper region of the left lung which is marked with the blue boxes. A conspicuousness is detectable in the *in-vivo* images. In the dark-field CT image, a region with extensive loss of signal intensity can be found (Figure 5.3(A, E)) indicating an increase in tissue density. In the corresponding attenuation image, an increase in signal intensity is observable in the same region (Figure 5.3(B, F)). As in the attenuation image highly absorbing ribs get blurred over the weak absorbing lungs

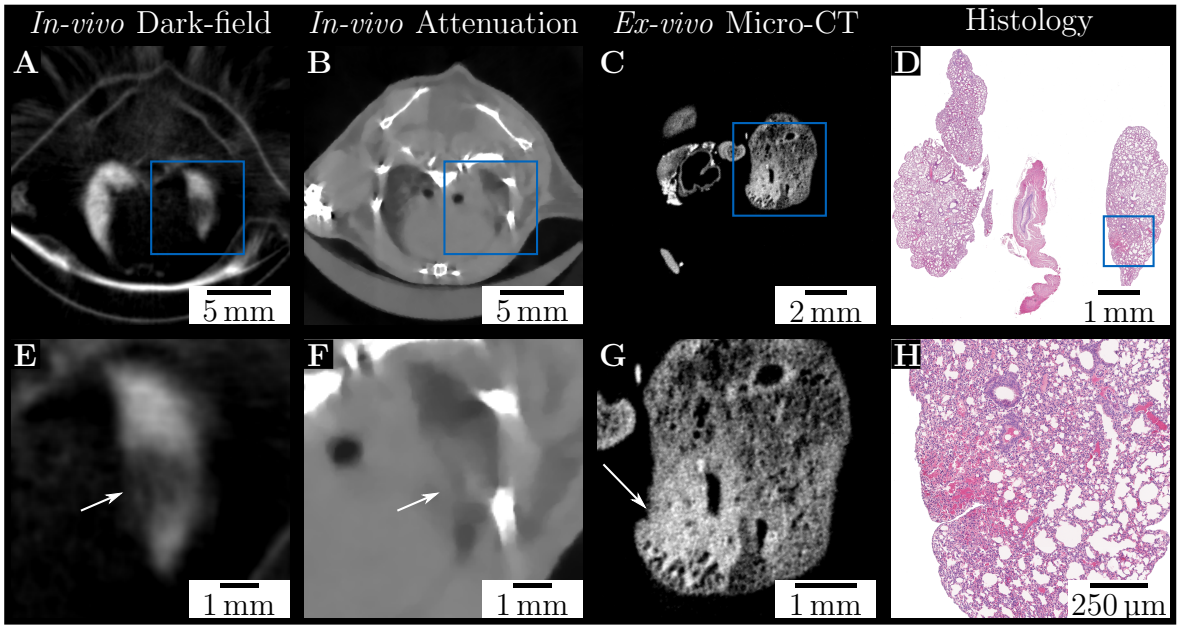

Figure 5.3: Multimodal image analysis in an upper level of the lung. Representative slices of *in-vivo* dark-field (A, E) and transmission (B, F) measurements, *ex-vivo* measurements (C, G), and histological sectioning (D, H) are presented. The blue boxes correspond to the area of the image at the bottom (E-H). The developed atelectasis with bleeding into the tissue in the left lobe of the lung can be seen in each modality. The gray values are windowed for the best visual appearance and scaled identically within their respective modality.

this modality is more prone to motion artifacts due to breathing the structures in the lung tissue are not as sharp as the ones in the dark-field image. The corresponding *ex-vivo* micro-CT slice of the eosin-stained lung verifies that in this region, the tissue is denser and morphological different to the normal lung tissue (Figure 5.3(C, G)) and is depicted within the blue box and marked with the white arrow in the bottom row. Here, the alveolar structure is destroyed around the airway. Analyzing the consecutive section counterstained with hematoxylin revealed the appearance of an atelectasis with bleeding into the tissue in this area (Figure 5.3(D, H)), as indicated by the pink color. In this region, the alveolar structure collapsed which leads to a denser tissue. Due to this, a changed dark-field signal is conspicuous in this area representing an inferior ventilation in the lung.

In Figure 5.4 the left lung, the lobus cranialis, lobus medius, and lobus caudalis of the right lung are visible. In the *ex-vivo* micro-CT image of the eosin-stained lung (Figure 5.4(C, G)) changes within the lung tissue of the left lobe can be observed. The brighter area marked with the blue box and the white arrow, respectively, around the

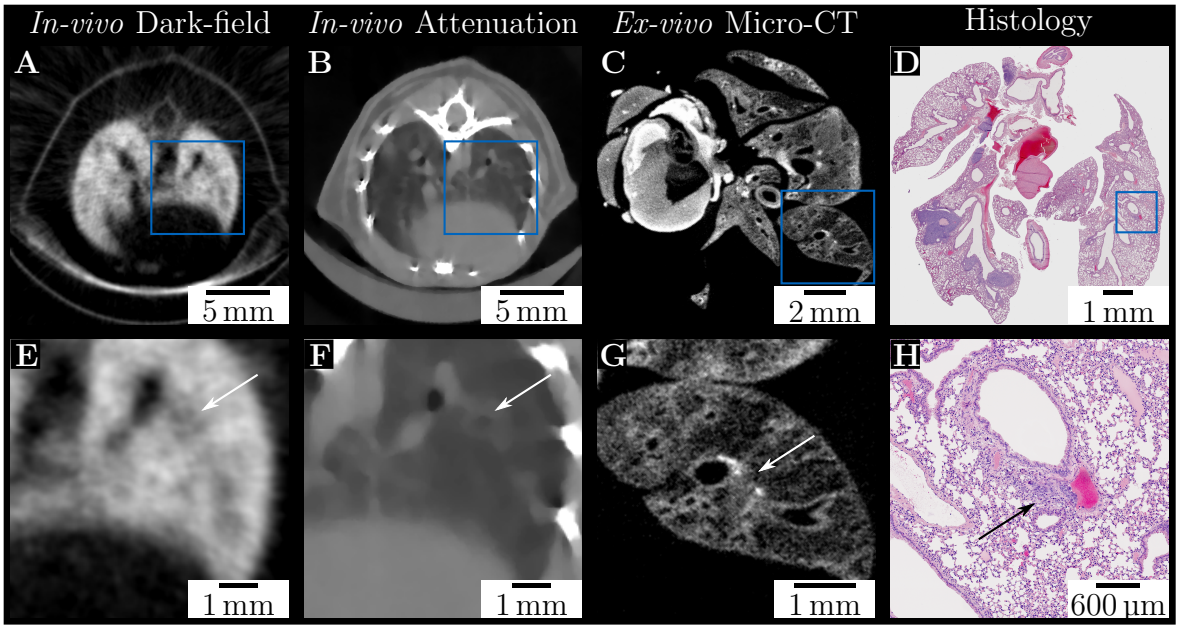

Figure 5.4: Multimodal image analysis in a middle level of the lung. Representative slices of *in-vivo* dark-field (A, E) and transmission (B, F) measurements, *ex-vivo* measurements (C, G), and histological sectioning (D, H) are presented. The blue boxes correspond to the area of the image at the bottom (E-H). Two conspicuous features can be detected for those slices and are indicated with the white arrows. The gray values are windowed for the best visual appearance and scaled identically within their respective modality.

airways caused by the strong eosin stain indicate for the occurrence of tumorous tissue. The comparison with the corresponding slices from the *in-vivo* dark-field measurement revealed again a small area with a loss of signal intensity in the same location of the lung parenchyma (Figure 5.4(A, E)). In addition to that, also the signal intensity and hence the tissue density can be identified in the corresponding *in-vivo* attenuation image (Figure 5.4(B, F)). Correlating this area to the histological section verifies the presence of tumorous tissue around the airway (Figure 5.4(D, H)).

The largest tumor nodule was detected in the third imaging level presented in Figure 5.5. In the middle of the lobus caudalis (Figure 5.5(A, E)) reveals a round area with a significant decrease in signal strength. Furthermore, as indicated by the white arrow, several smaller changes in tissue morphology can be identified in the tip of lobus medius. Distortions in the homogeneous (strongly scattering) lung pattern caused by the growth of a tumor are easily identified in the slice of the dark-field signal. Compared to the conventional *in-vivo* attenuation signal (Figure 5.5(B, F)), the lung tumor is more easily recognized and appears as a black void in the dark-field image. As the border

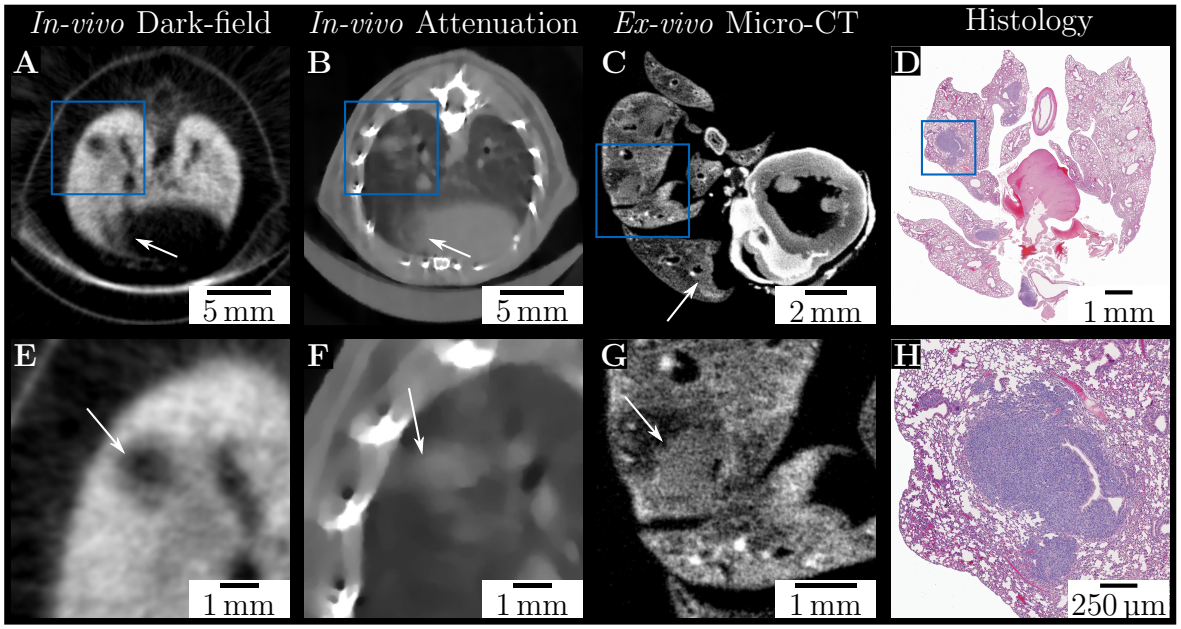

Figure 5.5: Multimodal image analysis in a lower level of the lung. Representative slices of *in-vivo* dark-field (A, E) and transmission (B, F) measurements, *ex-vivo* measurements (C, G), and histological sectioning (D, H) are presented. The blue boxes correspond to the area of the image at the bottom (E-H). A solitary tumor nodule in the middle of the right caudal lobe was detected (A: blue box, E: white arrow). The three-dimensional reconstruction allows for an information of the spatial distribution of the tumor. The boundary of the changes at the tip of the right caudal lobe was also sharper in the dark-field signal (A: white arrow) than in the attenuation image (B: white arrow). The gray values are windowed for best visual appearance and scaled identically within their respective modality.

of the lung tumor was sharper in the *in-vivo* dark-field image, this modality was used for a precise tumor volume quantification. For this purpose, all layers containing the detected tumor were included into the quantification. In total, the tumor had a volume of 1.17 mm^3 with a maximum expansion of 1.72 mm in length, 1.29 mm in width and 1.12 mm in height. In the *ex-vivo* micro-CT image of the eosin-stained lung (Figure 5.5(C, G)), the tumor can also be identified by changes within the lung tissue and the eosin stain. The morphological changes in the lung parenchyma caused by the tumor are verified by the corresponding histological section (Figure 5.5(D, H)). The purple color in those image indicates the occurrence of cell nuclei which is typically for tumorous tissue.
In order to obtain a better impression about the spatial distribution of the lung and the tumor, a volume rendering of the measured data was created and is illustrated in Figure 5.6 for different views. The bones, which are depicted semi-transparent, were extracted from the volume of the attenuation signal, whereas the lung tissue as well

as the tumors, which are represented in salmon and light yellow respectively, were segmented from the volume of the dark-field CT. The volume rendering allows for a clear representation of the tumor size and shape within the volume of the lungs. The previously described occurrence of tumor clusters and regions with atelectasis are confirmed by the segmentation. A small tumor is located in the inner part of the left lung parenchyma which could be well observed in the reconstructed volume in Figure 5.3 and also with minor confidence using the radiography of Figure 5.1. Moreover, the solid tumor which was missed in the 2D radiography but diagnosed in Figure 5.5 as a broad distribution in the middle of lobus caudalis.

5.5 Automated Lung Segmentation and Signal Analysis

Section 5.2 described this tumor study including not only one mouse but in total 8 treated and 4 control mice. As the described case study indicates the mouse introduced previously was the only one to develop a resolvable tumor cluster, whereas in histology only small tumor spots of a few cells could be observed. Nevertheless, histology revealed the occurrence of regions with collapsed or incomplete extension of the pulmonary parenchyma, described as lung atelectasis. Lung atelectasis in general can be distinctive very severe locally, but also spread globally over the whole lung volume and is characterized by a collapsed alveoli which finally results in a decreased dark-field signal. In general, there is not only atelectasis resulting in a decreased dark-field signal, but also diseases like COPD or pulmonary fibrosis leading to a similar result. In all of those diseases the alveoli structure is collapsed (atelectasis), inflated (COPD), or scarred (fibrosis) leading to a significant loss of scatter signal. At least for the two latest, animal studies using dark-field radiography confirmed that those changes can be detected very early and classified into stages [Hellbach, 2015; Hellbach, 2017; Yaroshenko, 2013]. In contrast to the radiographies, where the masks can easily segmented by hand, the effort of manually segmenting the lung would be enormous as the lungs spreads over several hundreds of slices. For analysis purpose whether the consequences of an atelectasis can be diagnosed using dark-field CT and to further quantify the signal intensities of the lung for attenuation and dark-field signal, here a lung segmentation algorithm based on the CT volume is introduced. For this purpose all three image modalities were used in order to segment a binary mask of the lung for each CT volume automatically, even though the phase-contrast volume has not been considered yet. The procedure will be shortly introduced in the following.

- **Bilateral filtering**
  As a first step, the input volume of the dark-field and the phase-contrast signal is

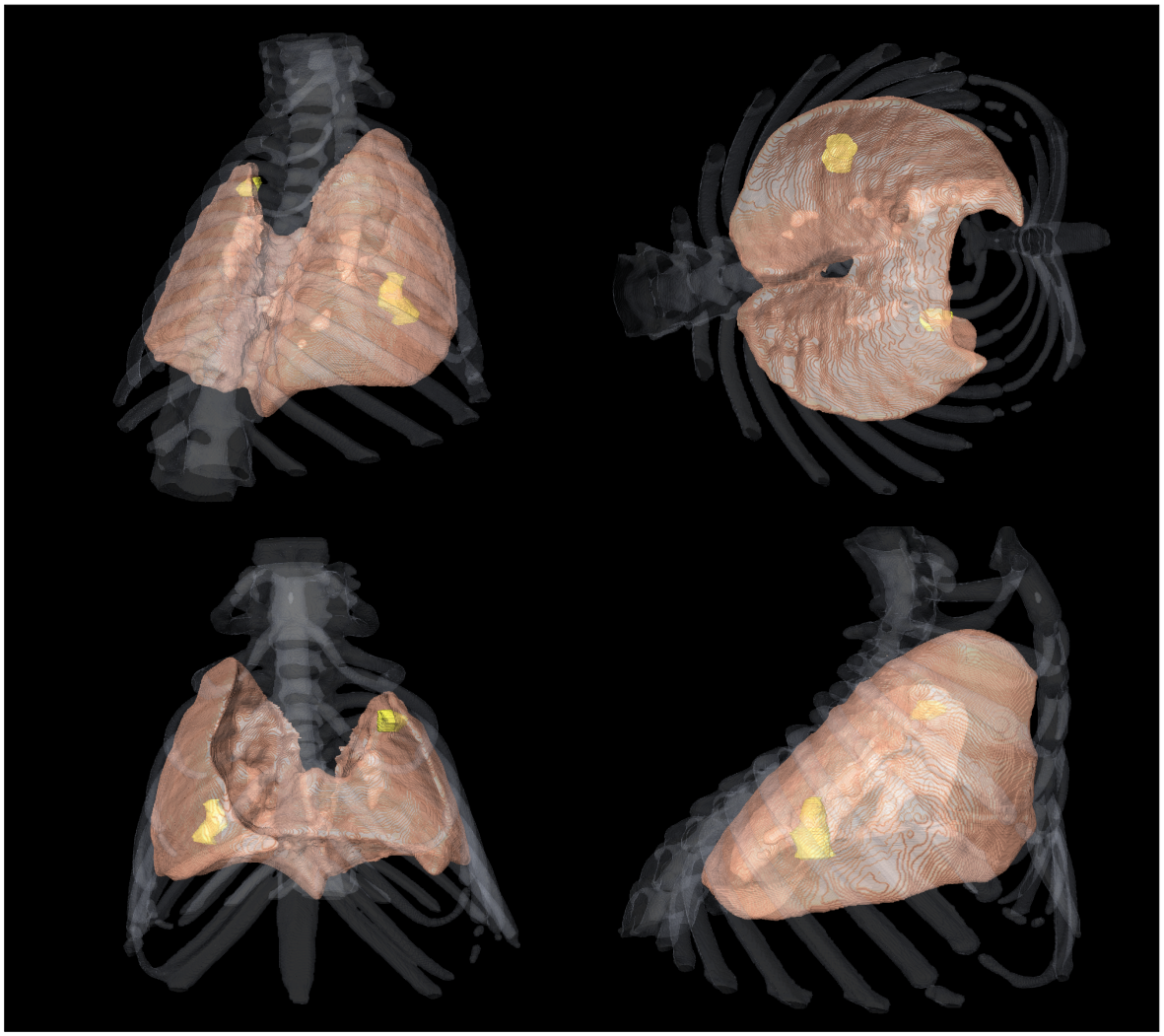

Figure 5.6: Volume rendering of the mouse with lung tumor from four different views. The bones were extracted using the attenuation CT, whereas the lung tissue (salmon) as well as the tumors (yellow) were segmented using the dark-field CT reconstructions. The shape and the size of the tumor nodules are very representable using a volume rendering of the thorax.

bilateraly filtered in order to obtain a smoothed and homogeneous signal over the lung [Tomasi, 1998]. In contrast to other noise-reducing filters, such as Gaussian blur, median filter, or averaging filters, the bilateral filter preserves the edges in the volume. Furthermore, the bilateral filtering is applied for every slice in axial, coronal, and sagittal direction, and the mean value for the volume is calculated as the output. Moreover, an erosion and dilation algorithm (opening operation), where a kernel slides through the image, is used to obtain homogeneous edges of

the lung volume [Gonzales, 2002].

- **Thresholding and logical combination**
  As we deal with three mutually independent signals, thresholding is applied in order to obtain binary masks. This is depicted for an exemplary slice in Figure 5.7. As all signals are perfectly co-registered, and a volume transfer from one signal modality to the other is allowed, it is possible to combine logically the three obtained masks. In this case, the mask of the conventional attenuation signal (Figure 5.7(A)) helps to differentiate all absorbing structures, such as the torso of the mouse, and the animal bed. The thresholding of the dark-field signal (Figure 5.7(B)) selects highly scattering structures, such as the lung and the fur, but also beam-hardening induced dark-field signal of the spine. The osseous structures can be excluded by thresholding the phase-contrast volume (Figure 5.7(C)), and using a NOT-operator to the previously obtained binary masks combined with the AND-operator.

- **Residual structure removal**
  Using thresholds and logical combination, it is possible to segment the lung automatically. However, as depicted in Figure 5.7(D), some residual structures, induced by the animal bed and the fur of the mouse are segmented. A slice-wise application of a binary opening operation is used in order to remove those additional structures, resulting in the final binary mask as shown in Figure 5.7(E). Those masks can now be applied to the respective volume in order to quantify the signal intensities.

As the volume of the calculated mask is perfectly co-registered to the reconstructed volumes of conventional attenuation, dark-field, and phase-contrast signal, those masks can be applied to the reconstructed volumes. Consequently, it is possible to extract the lung volume and do a quantitative signal analysis. This was done for all 8 LLC treated and 4 control mice of this study, and a scatterplot of the attenuation and the dark-field signal is depicted in Figure 5.8. As one can see, a clear differentiation between LLC treated mice (blue dots) and control mice (orange stars) is not possible. Nevertheless, the mean values of the dark-field signal of the control mice tend to be higher than those of the treated mice, whereas the values of the attenuation signal tend to be lower for the control mice, which could be expected. The reason for the missing clear differentiation between LLC and control mice can be explained by the fact, that also several control mice developed regions of atelectasis, whereas lungs treated with LLC cells remains unchanged. The developed atelectasis also for control lungs might be explained by the circumstance that immediately before the CT measurements, further experiments were performed on another setup, where the mice had already been anaesthetized. As a result of the long anaesthesia, atelectases may have formed in the control mice as well.

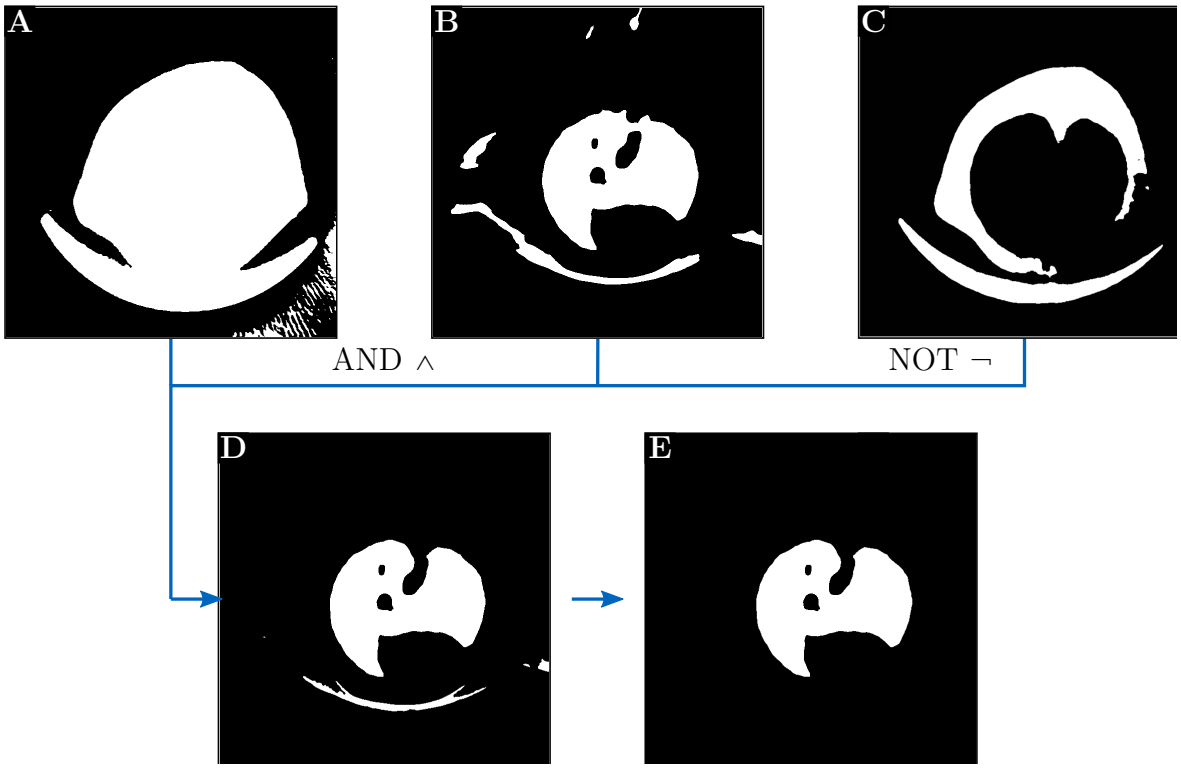

Figure 5.7: Segmentation of a binary lung mask. Thresholding of attenuation (A), dark-field (B), and phase-contrast (C) leading to three binary masks. By logical combination (AND and NOT operator) of those three, a mask with segmented lung and additional residual structures is obtained (D). The final mask (E) is obtained after removing the structures via slice-wise application of a binary opening operation.

In order to demonstrate the different states of ventilation, Figure 5.9 shows a fusion image of the conventional attenuation image in gray values and color-coded dark-field CT of *in-vivo* mice with different pathological stages of the lung. The fusion images are created for three different stages of ventilation in order to enhance the visualization of the decreased dark-field signal, caused by atelectasis, analogous to Velroyen et al. [Velroyen, 2015] and inspired by the obtained images from the combination of positron emission tomography and conventional absorption-based CT (PET-CT). However, in contrast to PET-CT, where a radioactive tracer is introduced into the body and the simultaneous detection of two gamma rays in opposite direction hints at the concentration of the radioligand in metabolic tissue, here, brighter color indicates for stronger scattering, and therefore for a healthy lung tissue. The fusion images are able to provide an overview of anatomy contributed by the attenuation CT, and functional information provided by dark-field CT at the same time. The corresponding fusion CT images of gray value coded attenuation with overlying hot color coded dark-field signal of three

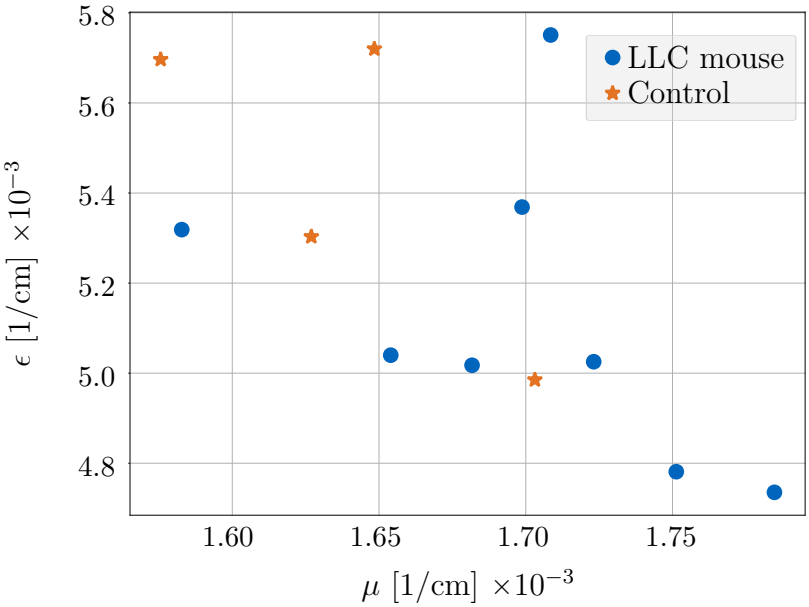

Figure 5.8: Signal quantification of *in-vivo* CT measurements. The x-axis represents the mean value of the attenuation coefficient μ, while the y-axis represents the mean value of the dark-field signal. The values of the LLC treated mice are presented by the blue dots, the control mice are depicted with the orange stars. A clear differentiation between LLC mice and control mice is not possible. Nevertheless, the dark-field signal of the control mice tend to be higher than those of the treated mice, whereas the values of the attenuation signal tend to be lower for the control mice.

different degrees of ventilation can be seen in Figure 5.9. Strong dark-field signals are indicated in yellow, whereas low-signal is visualized in red. Here, the images are depicted for three different strengths of the dark-field signal: severely reduced (Figure 5.9(A, E)), reduced (Figure 5.9(B, D)), and control (Figure 5.9(C, F)). As one can see in the color-coded fusion images, the mouse without any atelectasis or conspicuous features exhibit a stronger overall dark-field signal. In contrast, due to the collapse of several alveolar structures, and the bleeding into the lung tissue, the functionality as well as the scattering ability of the lung is decreased, which finally results in a loss of dark-field signal strength. Figure 5.9(G) shows that not only the treated LLC mice exhibit a decreased dark-field signal, but also the lung of control mice show a reduced dark-field signal strength. This can be explained by the development of atelectasis or rather less inflated lung tissue. Due to some technical issues prior to the measurement, the measurement was delayed while the mouse was under anaesthesia on the sample bed. This may have favored a worse ventilation of the lungs, which ultimately leads to a reduction of the dark-field signal.

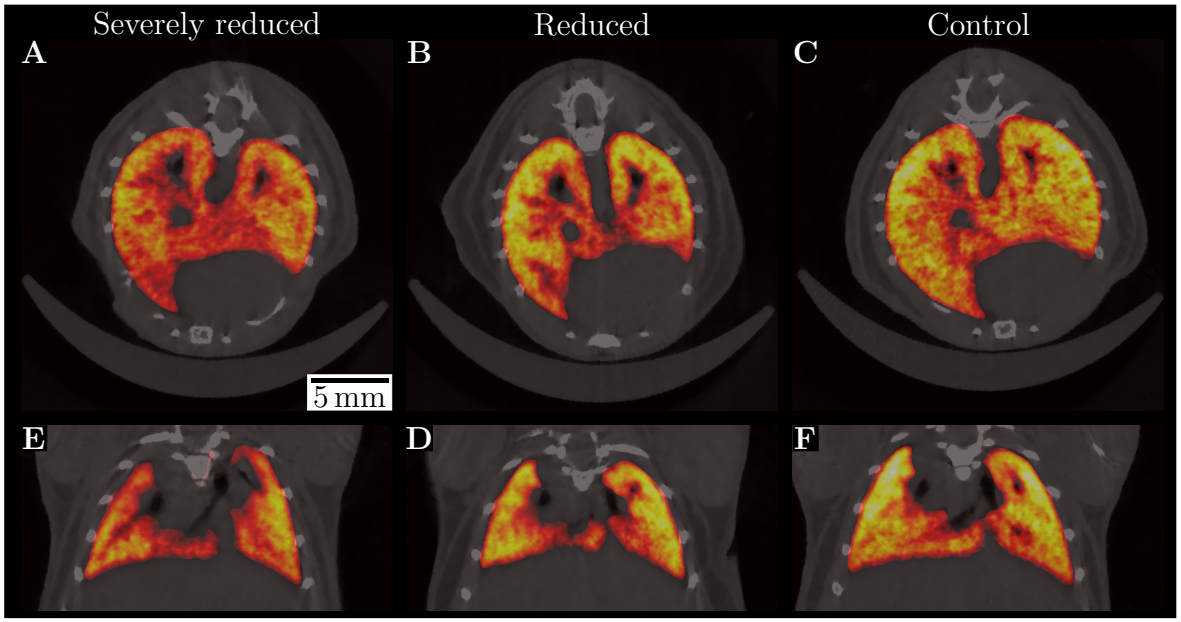

Figure 5.9: Fusion images of conventional attenuation in gray values and color-coded dark-field CT of *in-vivo* mice with different pathological stages of the lung. Images (A-C) represent comparable cranial to caudal axial slices of the lung volume, whereas the images (D-F) show coronal slices. Red regions indicate a tissue with strongly reduced scattering abilities, whereas yellow areas exhibit an increased scattering ability. The lungs without any salience (C, F) appear brighter than those with mild (B, E) or severe (A, D) changes of the lung tissue.

5.6 Discussion

Within this chapter, the diagnostic potential of a prototype grating-based dark-field CT scanner, with a conventional, polychromatic X-ray source, using *in-vivo* dark-field CT measurement of a mouse with pulmonary carcinoma was demonstrated. It has been shown that it is possible to detect tumors earlier and more easily using three-dimensional dark-field CT measurements compared to the two-dimensional attenuation and dark-field radiography. Additionally, it was demonstrated that it is possible to correlate the absent or decreased dark-field signal, e.g. caused by the growth of a lung tumor or a developed atelectasis, to the morphological changes within the lung tissue detected with *ex-vivo* micro-CT measurements and histology. As the contrast in soft tissue is rather low in absorption-based micro-CT, the contrast for the *ex-vivo* measurements was enhanced using a staining agent described by Busse et al. [Busse, 2018]. Despite the significant reduction of volume, caused by shrinkage and deformation during histological processing [Kirsch, 2010; Gallastegui, 2018], and the increased volume, resulting from respiratory motion, a correlation of conspicuous features between *in-vivo*

and *ex-vivo* measurements was demonstrated.
A well-established mouse model for pulmonary cancer was used. LLC cells are applied intravenously to the tail vein and the tumor metastasize into the lungs within a few days. As the aim was to investigate and detect the tumors at an early stage, the time between cell injection and final measurements, unfortunately, was not sufficient for tumor cells to form in adequate numbers and size in all mice. In order to avoid this happening in future studies different strategies can be pursued. First, dark-field radiography could already be used for monitoring between cell injection and CT measurement, in order to detect small deviations after cell injection and estimate the tumor growth. Second, as a trade-off between dose and three-dimensional information, dark-field tomosynthesis measurements could be used for the monitoring. Finally, longitudinal CT studies would allow to directly track the tumor growth within the lung tissue, but at a significantly higher dose.
During the *in-vivo* image acquisition, the mouse was breathing freely, inducing blurring of the images. As the resolution of the system is approximately one third of the natural motion amplitude of the thorax, which lies typically in the range of 200 µm [Chang, 2015], the artifacts are clearly visible for radiography and CT, respectively. Due to small movement of the specimen during in-vivo CT acquisition, however, this blur was further amplified affecting mainly the conventional transmission signal as highly absorbing bones get blurred over the soft tissue and the lungs with a high contrast. These movements may partly be caused by the resting position of the mouse. During the acquisition the animal was in its natural prone position. The respiratory movement of the thorax causes smaller movements of the area to be imaged, which finally leads to smearing in the image. To counteract this, future studies should include a supine position of the mice, or the measurements should be triggered with the breathing. In order to achieve the latter, however, a shorter exposure time is necessary, which requires either a more powerful X-ray source or a more sensitive detector system.
Despite this, the 3D information of the CT reconstructions of both modalities under consideration allows for a clear diagnosis of the tumors and their respective spatial distribution. However, it is necessary to perform studies with larger sample sizes and different stages of the disease in order to receive a detailed analysis of the advantage of dark-field imaging over conventional CT in terms of increased sensitivity and specificity for the diagnosis of e.g. pulmonary carcinoma. Different stages would also provide information about the feasibility of pulmonary carcinoma detection at a very early stage by using dark-field CT. Moreover, increasing statistics by performing a study with a sufficient sample size, or even multiple measurements at several time points, enables the realization of a conclusive reader study or a precise analysis of the minimum size of conspicuous features to be detected.
Furthermore, an automated lung segmentation approach has been introduced. For this purpose, the properties of the three mutually independent but perfectly co-registered

signals of attenuation, dark-field, and phase-contrast are used. Doing so, the attenuation signal helps to segment absorbing structures, such as the torso or the sample bed, the dark-field signal segments highly scattering tissue, and the phase-contrast signal extracts bony structures from the volume. Using this automated segmentation approach, a detailed signal intensity evaluation could be performed. While this is not of utmost importance for locally very limited diseases, e.g. lung tumours, it could play a more important role for diseases like pulmonary fibrosis or COPD. In clinical routine with respect to application it is more important to determine and localize tumor nodules within the lung than evaluate the signal strength provided by the lung. In contrast, in diseases like COPD the lung tissue and alveoli are damaged overall. Therefore, an examination of the tissue at an very early stage would help to treat the disease and prevent its progression. Previous studies using dark-field radiography already showed that a classification into stages of diseases [Hellbach, 2015] or a discrimination between different kinds of diseases is possible [Burkhardt, 2015]. The advantage of the three-dimensional CT reconstructions in early detection via classification has to be evaluated in future animal studies.

Conclusion and Outlook 6

This chapter summarizes the main results of the work carried out within this thesis and potential further steps are pointed out and discussed.

Optimization of the Skyscan 1190

The aim of this work was to optimize the prototype dark-field and phase-contrast CT scanner Skyscan 1190 in order to improve the image quality of the reconstructed volumes and thereby increase the range of preclinical application and investigation of dark-field CT. As *in-vivo* measurements imply a limited time due to anesthesia and dose restrictions, the available total measurement time should be used in the most effective and reliable way. The measures were focused on optimizing the hardware as well as the data acquisition for *in-vivo* CT measurements, as the reconstructed volumes suffered from long exposure times and consequently undersampling artifacts. To overcome this issues, the grating interferometer was improved by bending the gratings, a new detector was installed, and the data acquisition protocol was adapted to the new configurations.

Grating interferometer

As a first step to improve the setup, optimization on the grating interferometer was accomplished. A plane grating geometry induces a reduction of visibility and intensity of pixels offside the optical axis. To counteract this, the phase grating and the analyzer grating were curved with a radius of curvature according to their respective distance to the source. By bending the gratings, a perpendicular angle of incidence of the X-rays to the gratings over the whole field of view is reached. Consequently, this reduces the drop of visibility from 41% to 93%, and of the intensity from 41% to just 77% especially at the sample border leading to improvements in image quality. Additionally, the flux over the whole image could be increased by the installation of a new phase grating on a thinner substrate by 44%. The grating interferometer could be further improved

in two ways: either by using a source grating substrate which allows for a bending radius of 3 cm, or by using plane gratings with a divergent grating substrate. The latter means that during the grating fabrication no parallel beam but a cone beam is used to irradiate the photosensitive resist. This would lead to a perpendicular angle of incidence to the absorbing structures over the whole FOV and would avoid the drop of visibility and intensity in absence of bent gratings. Furthermore, the masks could be positioned to the required distance to the source, so that even grating adaptions to small distances could be achieved. The flux itself could be further increased using less-absorbing grating substrates such as graphite or polymide [Schröter, 2017]. However, when using those substrates the design energy of the grating interferometer still has to be considered. As less absorbency would shift the mean energy of the polychromatic spectrum passing through the interferometer to lower values, the maximum voltage most probably would require to be lower which in the end leads to a reduced current. Finally, the balance between absorbance, voltage, and current with this setup has to be investigated.

Detector

A new detector with different specification has been implemented and characterized. The initial detector was a Hamamatsu flat panel detector with a pixel size of $50 \times 50\,\mu m^2$, whereas the new one is a Dexela 1512 with a slightly increased pixel size of $74.8 \times 74.8\,\mu m^2$. For both detectors the resolution was investigated using a Siemens star as resolution pattern. We could show that the spatial resolution in real-space is almost similar for the Dexela detector, while both detectors exhibit an approximately radially symmetric spatial system response. However, the number of detected photons per pixel of the incoming beam is increased by a factor of approximately 2.6 by using the Dexela detector. On the one hand this could be explained by the larger area per single pixel with the factor of 2.2, and on the other hand this can be explained by a slightly thicker scintillator and therefore a higher quantum efficiency. The new detector systems allows for shorten the exposure time per image significantly, which finally leads to the possibility of performing CT measurements with more angular projections in the same time. Possible future improvements can be achieved by implementing a detector which allows to reduce the exposure time even more, but at the same time increase the spatial resolution. By further decreasing the exposure time further, breath-hold triggered and ventilated measurements would be enabled leading to a reduced natural blurring in the reconstructed volumes.

Data acquisition

The previous modifications of the hardware of the scanner enable for adaptions of the data acquisition protocol, defined by exposure time, grating steps, and angular projections. To guarantee the best possible image quality of the reconstructed volumes, the acquisition protocol was modified in two ways. First, the exposure time for each image acquired could be reduced by more than factor of 2 from $t_{\mathrm{Exp,ini}} = 1.43\,\mathrm{s}$ to $t_{\mathrm{Exp,new}} = 0.70\,\mathrm{s}$. The gained time by the reduction could be used in order to increase the amount of angular projections N for CT measurements, which was increased from $N_{\mathrm{ini}} = 211$ to $N_{\mathrm{new}} = 303$. Also, the number of grating positions per angular projection was increased from $n = 4$ to $n = 5$, which of course affects the number of projections. With this optimizing measures, instabilities during the processing and reconstruction routine could be compensated and occurring residual artifacts could be avoided. By performing phantom measurements it was shown that the modifications on the hardware and on the data acquisition protocol leads to a decrease of undersampling artifacts, whereas the homogeneity and the total image quality increases. In order to quantify these findings, a CNR analysis of different features on FBP reconstructions was performed. The important CNR values for the respective features and modality could be improved by a factor of two by both adapting the grating configuration and implementing the Dexela detector.
The improved scanner performance was successfully verified by additional in-vivo measurements of mice. Since, in-vivo measurements imply the occurrence of breathing and heartbeat moving artifacts, these CT measurements were carried out within the framework of other animal studies and not expressly to emphasize the optimization of the setup. Nevertheless, also here the upgraded hardware showed great improvements regarding image quality such as sharpness, homogeneity, or occurrence of artifacts.
In the future some different approaches of data acquisition schemes could be tested. The data acquisition is performed in a step-and-shoot phase-stepping mode, which means that the phase stepping and the gantry rotation are performed one after the other. However, first experiments showed the feasibility of performing single-shot techniques such as sliding-window or intensity-based statistical iterative reconstruction [vTeuffenbach, 2017]. Using single-shot techniques one is able to combine phase-stepping with the gantry rotation and decrease the number of steps per angular projection to one. This allows to sample the specimen from more projections, decreasing the amount of undersampling.
Although the optimization could be implemented successfully, there is still some room left for improvements and investigation in the future. The most significant influence on the sharpness and the image quality is probably by including mechanical ventilation and breath-hold during image acquisition via an intubation. The ventilation setup could send a trigger signal to the imaging software, to acquire an image in the breath-hold of

each cycle. In addition, the ventilation could be used in order to use a gas-anesthesia. However, a number of preconditions still need to be established. Without harming the animals, the breath-hold could be extended to approximately 200 ms. This would also require an exposure time of approximately 200 ms. To obtain a noise-free within this short time, a more powerful X-ray source is needed. Since a large share of the emitted X-rays is already absorbed by the grating substrates, a more powerful source would lead to a higher incoming flux at the detector, which finally could lead to a reduction of the exposure time per image. Moreover, the software of the setup must be prepared in order to allow an external trigger signal to acquire an image. Nevertheless, some heart-induced blurring or gasping movements is to be expected even with given artificial respiration.

Diagnostic value of *in-vivo* phase-contrast imaging

So far, several *in-vivo* studies have been conducted on the imaging of lung diseases in mice using grating-based radiography. Thereby, the focus lied primarily on the dark-field information in comparison with conventional transmission images. Within this thesis, for the first time investigations on the value of *in-vivo* phase-contrast imaging were accomplished and it was demonstrated that this contrast modality significantly improves the diagnostic value of conventional chest X-ray for the detection of major respiratory pathologies in living mice undergoing single lung transplantation. Moreover, the potential of grating-based X-ray imaging to detect multiple organ-specific pathologies was demonstrated, since information on transmission (bones, mediastinal structures), dark-field (lung parenchyma) and phase contrast (bronchial system) is perfectly co-registered and available simultaneously. This radiographic imaging technique will most likely not replace CT or bronchoscopy in possible major respiratory diseases because of the missing three-dimensional information. However, considering future clinical applications, it could be considered for earlier detection of bronchial stenosis and thus help to move the patient to a specific respiratory diagnostic within a tight time frame. Nevertheless, the implementation of grating-based phase-contrast imaging to clinical environment is far from being trivial. Different kinds of technical requirements have to be met, such as the fabrication of higher grating structures needed due to higher energies, the increased field-of-view, or the completely different setup design. Moreover, the limited active area and stitching of several grating tiles leading to issues during processing procedure due to various gradients and offset for each tile. In order to investigate and address the technical challenges and requirements of transferring grating-based interferometry to humans, research has been extended to larger in-vivo animals and post-mortem human in recent years [Gromann, 2017; Hellbach, 2018; Willer, 2018; Fingerle, 2019]. Finally, the investigations on imaging have been suc-

cessfully extended to human in the clinic at a prototype dark-field radiography setup where first studies investigating COPD are going on and publications are expected in the very near future.

Dark-field CT imaging

In contrast to the phase-contrast signal, the dark-field imaging is highly promising for clinical implementation and application. The realization of a clinical prototype is the first step towards widely use in clinical routine. Moreover, also research is going on of extending the fields of application of the dark-field signal by accessing it for clinical CT setups. Within the framework of this thesis, the fundamental research of possible applications in clinical usage was conducted. The improved scanner performance allowed for the verification of *in-vivo* measurements of mice and have enabled satisfying image quality for time-limited *in-vivo* attenuation and dark-field CT measurements. Therefore, dark-field CT measurements were investigated for the evaluation of *in-vivo* lung imaging using the example of lung cancer induced by the application of the Lewis-Lung-Cell carcinoma murine model. In this study, the development of detectable tumor nodules after cell application was restricted to one specimen. It was demonstrated that dark-field CT measurements allow for an earlier and easier detection of pulmonary carcinoma compared to two-dimensional dark-field radiography. Moreover, the absent dark-field signal caused by poorly scattering ability of tumor nodules could be correlated to morphological changes detected with *ex-vivo* micro CT and histological sectioning. In order to avoid studies with low statistics in the future, more reliable mouse models should be used and multiple measurements should be carried out in longitudinal studies. This could yield some interesting facts. First, the medical-diagnostic advantage of dark-field CT over conventional attenuation CT could be investigated in more detail. On the other hand, it would be possible to compare, examine and analyze the two complementary contrast modalities for their use in early detection. In addition, longitudinal studies would make it possible to observe the development of a tumor and to get an impression of the required size in order to detect it by imaging. At best, the number of experimental animals should be increased in order to obtain better statistics on the one hand, and on the other hand to counteract unforeseeable complications in individual animals, during the experiment or between individual measurements, and thus not to endanger the purpose of the experiments.
In addition, an automated lung segmentation approach has been introduced successfully. For this purpose, the three mutually independent but perfectly co-registered signals of attenuation, dark-field, and phase-contrast are used to calculate a binary mask of the lung volume. Applying the mask to the reconstruction volumes allow for a signal analysis and quantification. This could help in the detection and classification

of diseases like pulmonary fibrosis or COPD in future animal CT studies according to radiography studies [Hellbach, 2015; Burkhardt, 2015].

Bibliography

[Ali, 2016] Ali, M. U. *et al.* Screening for lung cancer: a systematic review and meta-analysis. *Preventive medicine* **89,** 301–314 (2016) (Cited on page 74).

[AlsNielsen, 2011] Als-Nielsen, J. & McMorrow, D. *Elements of modern X-ray Physics* (John Wiley & Sons, 2011) (Cited on pages 5, 6, 13).

[Bech, 2009] Bech, M. *X-ray Imaging with a Grating Interferometer* PhD thesis (University of Copenhagen, 2009) (Cited on pages 23, 26, 28).

[Bech, 2013] Bech, M. *et al. In-vivo* Dark-Field and Phase-Contrast X-ray Imaging. *Scientific Reports* **3,** 3209 (2013) (Cited on page 62).

[Becker, 1986] Becker, E., Ehrfeld, W., Hagmann, P., Maner, A. & Münchmeyer, D. Fabrication of Microstructures with high Aspect Ratios and great Structural Heights by Synchrotron Radiation Lithography, Galvanoforming, and Plastic Moulding (LIGA Process). *Microelectronic Engineering* **4,** 35–56 (1986) (Cited on page 29).

[Behling, 2015] Behling, R. *Modern Diagnostic X-Ray Sources: Technology, Manufacturing, Reliability* (CRC Press, 2015) (Cited on page 9).

[Bevins, 2012] Bevins, N., Zambelli, J., Li, K., Qi, Z. & Chen, G.-H. Multi-Contrast X-ray Computed Tomography Imaging using Talbot-Lau Interferometry without Phase stepping. *Medical Physics* **39,** 424–428 (2012) (Cited on page 42).

[Bidola, 2017] Bidola, P. M. *Characterization and Application of High Resolution Phase-Contrast LaboRatory Micro-CT Setups* PhD thesis (Technical University of Munich, 2017) (Cited on page 77).

[Bidola, 2019] Bidola, P. *et al.* A step towards valid Detection and Quantification of Lung Cancer Volume in experimental Mice with Contrast agent-based X-ray microTomography. *Scientific Reports* **9,** 1325 (2019) (Cited on page 74).

[Birnbacher, 2018] Birnbacher, L. *High-Sensitivity Grating-Based Phase-Contrast Computed Tomography with Incoherent Sources* PhD thesis (Technical University of Munich, 2018) (Cited on pages 22, 24, 27).

[Bonse, 1965] Bonse, U. & Hart, M. An X-ray Interferometer. *Applied Physics Letters* **6,** 155–156 (1965) (Cited on pages 2, 18).

[Boreman, 2001] Boreman, G. D. *Modulation transfer function in optical and electro-optical systems* **3.419857** (SPIE press Bellingham, WA, 2001) (Cited on page 9).

[Burkhardt, 2015] Burkhardt, R. *Optimization and Application of Prototype X-ray Phase Contrast and Dark-Field Small-Animal CT scanner* MA thesis (Technical University of Munich, 2015) (Cited on pages 90, 96).

[Busse, 2018] Busse, M. *et al.* Three-dimensional virtual Histology enabled through Cytoplasm-specific X-ray Stain for Microscopic and Nanoscopic Computed Tomography. *Proceedings of the National Academy of Sciences* **115,** 2293–2298 (2018) (Cited on pages 75, 88).

[Buzug, 2008] Buzug, T. M. *Computed Tomography* (Springer Berlin Heidelberg, 2008) (Cited on pages 5, 9, 13, 30, 34).

[Chabior, 2011] Chabior, M. *Contributions to the Characterization of Grating-based X-ray Phase-Contrast Imaging* PhD thesis (Technical University of Dresden, 2011) (Cited on pages 26, 52).

[Chambers, 2019] Chambers, D. C. *et al.* The International Thoracic Organ Transplant Registry of the International Society for Heart and Lung Transplantation: Thirty-sixth adult Lung and Heart-Lung Transplantation Report—2019; Focus Theme: Donor and Recipient Size Match. *The Journal of Heart and Lung Transplantation* **38,** 1042–1055 (2019) (Cited on page 61).

[Chambers, 2017] Chambers, D. C. *et al.* The Registry of the International Society for Heart and Lung Transplantation: thirty-fourth Adult Lung and Heart-Lung Transplantation Report—2017; Focus Theme: Allograft Ischemic Time. *The Journal of Heart and Lung Transplantation* **36,** 1047–1059 (2017) (Cited on page 61).

[Chang, 2015] Chang, S. *et al.* Synchrotron X-ray Imaging of Pulmonary Alveoli in RespiRation in live intact Mice. *Scientific Reports* **5,** 8760 (2015) (Cited on page 89).

[Chapman, 1997] Chapman, D. *et al.* Diffraction enhanced X-ray Imaging. *Physics in Medicine & Biology* **42,** 2015 (1997) (Cited on page 2).

[Cloetens, 1999] Cloetens, P. *et al.* HoloTomography: Quantitative Phase Tomography with micrometer resolution using hard Synchrotron Radiation X-rays. *Applied Physics Letters* **75,** 2912–2914 (1999) (Cited on pages 2, 18, 19).

[David, 2002] David, C., Nöhammer, B., Solak, H. H. & Ziegler, E. Differential X-ray Phase Contrast Imaging using a Shearing Interferometer. *Applied Physics Letters* **81,** 3287–3289 (2002) (Cited on pages 2, 19, 20).

[Davis, 1995] Davis, T., Gao, D., Gureyev, T., Stevenson, A. & Wilkins, S. Phase-Contrast Imaging of weakly absorbing Materials using hard X-rays. *Nature* **373,** 595 (1995) (Cited on pages 2, 18).

[De Angelis, 2014] De Angelis, R. *et al.* Cancer Survival in Europe 1999–2007 by Country and Age: Results of EUROCARE-5—a population-based Study. *The Lancet Oncology* **15,** 23–34 (2014) (Cited on page 73).

[De Marco, 2015] De Marco, F. *Optimizing Data Processing for Grating-Based X-ray Phase-Contrast Computed Tomography* MA thesis (Technical University of Munich, 2015) (Cited on page 42).

[Dempster, 1977] Dempster, A. P., Laird, N. M. & Rubin, D. B. Maximum Likelihood from incomplete Data via the EM Algorithm. *Journal of the Royal Statistical Society: Series B (Methodological)* **39,** 1–22 (1977) (Cited on page 42).

[Do, 2008] Do, C. B. & Batzoglou, S. What is the Expectation Maximization Algorithm? *Nature Biotechnology* **26,** 897 (2008) (Cited on page 42).

[Eggl, 2017] Eggl, E. *Biomedical X-ray Imaging at the Munich Compact Light Source* PhD thesis (Technical University of Munich, 2017) (Cited on page 8).

[Eggl, 2016] Eggl, E. *et al.* The Munich Compact Light Source: initial Performance Measures. *Journal of Synchrotron Radiation* **23,** 1137–1142 (2016) (Cited on page 8).

[Ehn, 2017] Ehn, S. *Photon-counting Hybrid-Pixel Detectors for Spectral X-ray Imaging Applications* PhD thesis (Technical University of Munich, 2017) (Cited on page 9).

[Fingerle, 2019] Fingerle, A. A. *et al.* Imaging features in post-mortem x-ray dark-field chest radiographs and correlation with conventional x-ray and CT. *European radiology experimental* **3,** 25 (2019) (Cited on page 94).

[Gallastegui, 2018] Gallastegui, A., Cheung, J., Southard, T. & Hume, K. R. Volumetric and linear Measurements of Lung Tumor burden from non-gated micro-CT Imaging correlate with histological Analysis in a genetically engineered Mouse Model of non-small Cell Lung Cancer. *LaboRatory Animals* **52,** 457–469 (2018) (Cited on page 88).

[Gohagan, 2005] Gohagan, J. K. *et al.* Final Results of the Lung Screening Study, a randomized feasibility Study of spiral CT versus chest X-ray Screening for Lung Cancer. *Lung Cancer* **47,** 9–15 (2005) (Cited on page 73).

[Gonzales, 2002] Gonzales, R., Woods, R. & Eddins, S. Digital Image Processing, Prentice Hall. *New Jersey* (2002) (Cited on page 85).

[Gromann, 2017] Gromann, L. *Development of a Large-Animal X-ray Dark-Field Scanner* PhD thesis (Technical University of Munich, 2017) (Cited on page 3).

[Gromann, 2017] Gromann, L. B. *et al.* In-vivo x-ray dark-field chest radiography of a pig. *Scientific Reports* **7,** 1–7 (2017) (Cited on page 94).

[Hahn, 2014] Hahn, D. *Statistical IteRative Reconstruction for X-ray Phase-Contrast Computed Tomography* PhD thesis (Technical University of Munich, 2014) (Cited on page 36).

[Hellbach, 2018] Hellbach, K. *et al.* Depiction of pneumothoraces in a large animal model using x-ray dark-field radiography. *Scientific reports* **8,** 1–8 (2018) (Cited on page 94).

[Hellbach, 2016] Hellbach, K. *et al.* Facilitated Diagnosis of Pneumothoraces in newborn Mice using X-ray Dark-Field Radiography. *Investigative Radiology* **51,** 597–601 (2016) (Cited on page 3).

[Hellbach, 2015] Hellbach, K. *et al. In vivo* Dark-Field Radiography for Early Diagnosis and Staging of Pulmonary Emphysema. *Investigative Radiology* **50,** 430–435 (2015) (Cited on pages 3, 62, 83, 90, 96).

[Hellbach, 2017] Hellbach, K. *et al.* X-ray Dark-Field Radiography Facilitates the Diagnosis of Pulmonary Fibrosis in a Mouse Model. *Scientific Reports* **7,** 340 (2017) (Cited on pages 3, 62, 83).

[Hemberg, 2003] Hemberg, O., Otendal, M. & Hertz, H. Liquid-metal-jet Anode Electron-impact X-ray Source. *Applied Physics Letters* **83,** 1483–1485 (2003) (Cited on page 7).

[Henschke, 1999] Henschke, C. I. *et al.* Early Lung Cancer Action Project: overall Design and Findings from baseline Screening. *The Lancet* **354,** 99–105 (1999) (Cited on page 73).

[Hertz, 2002] Hertz, M. I. *et al.* The Registry of the International Society for Heart and Lung Transplantation: nineteenth official Report - 2002. *The Journal of Heart and Lung Transplantation* **21,** 950–970 (2002) (Cited on page 61).

[Hsieh, 2003] Hsieh, J. *Computed Tomography: Principles, Design, Artifacts, and recent Advances* (SPIE press, 2003) (Cited on page 36).

[Huber, 1992] Huber, P. J. in *Breakthroughs in Statistics* 492–518 (Springer, 1992) (Cited on page 37).

[Ingal, 1995] Ingal, V. & Beliaevskaya, E. X-ray plane-wave Topography Observation of the Phase Contrast from a non-crystalline Object. *Journal of Physics D: Applied Physics* **28,** 2314 (1995) (Cited on page 18).

[IELCAPI, 2006] International Early Lung Cancer Action Program Investigators. Survival of Patients with Stage I Lung Cancer detected on CT Screening. *New England Journal of Medicine* **355,** 1763–1771 (2006) (Cited on page 73).

[Jud, 2018] Jud, C. *X-ray Vector Radiography for Biomedical Applications* PhD thesis (Technical University of Munich, 2018) (Cited on page 8).

[Kak, 1988] Kak, A. & Slaney, M. *Principles of Computerized Tomographic Imaging* (IEEE Press, 1988) (Cited on pages 5, 30, 32, 34).

[Kellar, 2015] Kellar, A., Egan, C. & Morris, D. Preclinical Murine Models for Lung Cancer: clinical trial Applications. *BioMed Research International* **2015** (2015) (Cited on page 74).

[Kenntner, 2012] Kenntner, J. *et al. Fabrication and Characterization of Analyzer Gratings with high Aspect Ratios for Phase Contrast Imaging using a Talbot Interferometer* in *AIP Conference Proceedings* **1437** (2012), 89–93 (Cited on page 29).

[Khan, 1999] Khan, S. U. *et al.* Acute Pulmonary Edema after Lung Transplantation: the Pulmonary Reimplantation response. *Chest* **116,** 187–194 (1999) (Cited on page 70).

[Kim, 2018] Kim, S. Y. *et al.* Critical Care after Lung Transplantation. *Acute and Critical Care* **33,** 206 (2018) (Cited on page 69).

[Kinsinger, 2017] Kinsinger, L. S. *et al.* Implementation of lung cancer screening in the Veterans Health Administration. *JAMA internal medicine* **177,** 399–406 (2017) (Cited on page 74).

[Kirsch, 2010] Kirsch, D. G. *et al.* Imaging primary Lung Cancers in Mice to Study Radiation Biology. *International Journal of Radiation Oncology* Biology* Physics* **76,** 973–977 (2010) (Cited on page 88).

[Koch, 2017] Koch, F. J. *X-ray opti cs made by X-ray lithography: Process optimization and quality control* PhD thesis (Karlsruher Institut für Technologie, 2017) (Cited on pages 29, 60).

[Kottler, 2007] Kottler, C., Pfeiffer, F., Bunk, O., Grünzweig, C. & David, C. Grating Interferometer based scanning Setup for hard X-ray Phase Contrast Imaging. *Review of Scientific Instruments* **78,** 043710 (2007) (Cited on page 42).

[Kroegel, 2011] Kroegel, C. *et al.* Airway Complications following Lung Transplantation - Clinic, Diagnosis, and Interventional Management. *Pneumologie (Stuttgart, Germany)* **65,** 293–307 (2011) (Cited on page 62).

[Lynch, 2011] Lynch, S. K. *et al.* Interpretation of Dark-Field Contrast and particle-size selectivity in Grating Interferometers. *Applied Optics* **50,** 4310–4319 (2011) (Cited on page 26).

[Mahajan, 2017] Mahajan, A. K. *et al.* The Diagnosis and Management of Airway Complications following Lung Transplantation. *Chest* **152,** 627–638 (2017) (Cited on page 62).

[Malecki, 2012] Malecki, A., Potdevin, G. & Pfeiffer, F. Quantitative wave-optical numerical analysis of the Dark-Field signal in Grating-based X-ray Interferometry. *EPL* **99,** 48001 (2012) (Cited on page 26).

[Martin, 2006] Martin, J. E. *Physics for Radiation Protection: a Handbook* 707–709 (John Wiley & Sons, 2006) (Cited on page 8).

[Meinel, 2014] Meinel, F. G. *et al.* Improved Diagnosis of Pulmonary Emphysema using *in vivo* Dark-Field Radiography. *Investigative Radiology* **49,** 653–658 (2014) (Cited on page 62).

[Meuwissen, 2001] Meuwissen, R., Linn, S. C., van der Valk, M., Mooi, W. J. & Berns, A. Mouse Model for Lung tumorigenesis through Cre/lox controlled sporadic activation of the K-Ras Oncogene. *Oncogene* **20,** 6551 (2001) (Cited on page 74).

[Mizobuchi, 2004] Mizobuchi, T., Sekine, Y., Yasufuku, K., Fujisawa, T. & Wilkes, D. S. Comparison of surgical Procedures for vascular and airway Anastomoses that utilize a "modified" non-suture external Cuff Technique for Experimental Lung Transplantation in Rats. *The Journal of Heart and Lung Transplantation* **23,** 889–893 (2004) (Cited on page 71).

[Momose, 2003] Momose, A. Phase-sensitive Imaging and Phase Tomography using X-ray Interferometers. *Optics Express* **11,** 2303–2314 (2003) (Cited on pages 2, 18).

[Momose, 2011] Momose, A., Yashiro, W., Harasse, S. & Kuwabara, H. Four-dimensional X-ray Phase Tomography with Talbot Interferometry and white Synchrotron Radiation: dynamic Observation of a living Worm. *Optics Express* **19,** 8423–8432 (2011) (Cited on page 42).

[Müller, 2013] Müller, M. *Experimental Characterization of the first preclinical X-ray Phase Contrast CT Scanner* Diploma thesis (Technical University of Munich, 2013) (Cited on pages 45, 47, 48).

[NLSTRT, 2013] National Lung Screening Trial Research Team. Results of initial low-dose Computed Tomographic Screening for Lung Cancer. *New England Journal of Medicine* **368,** 1980–1991 (2013) (Cited on page 73).

[Natterer, 1986] Natterer, F. *The Mathematics of Computerized Tomography* (Vieweg + Teubner Verlag, Wiesbaden, 1986) (Cited on page 34).

[Olive, 2006] Olive, K. P. & Tuveson, D. A. The Use of Targeted Mouse Models for Preclinical Testing of Novel Cancer Therapeutics. *Clinical Cancer Research* **12,** 5277–5287 (2006) (Cited on page 74).

[Paganin, 2006] Paganin, D. M. *Coherent X-ray Optics.* (Oxford Science Publications, 2006) (Cited on pages 5, 8, 9).

[Pastorino, 2003] Pastorino, U. *et al.* Early Lung-Cancer Detection with spiral CT and Positron Emission Tomography in heavy Smokers: 2-year Results. *The Lancet* **362,** 593–597 (2003) (Cited on page 73).

[Pfeiffer, 2007a] Pfeiffer, F., Kottler, C., Bunk, O. & David, C. Hard X-ray Phase Tomography with Low-Brilliance Sources. *Physical Review Letters* **98,** 108105 (2007) (Cited on pages 2, 19, 20).

[Pfeiffer, 2006] Pfeiffer, F., Weitkamp, T., Bunk, O. & David, C. Phase Retrieval and Differential Phase-Contrast Imaging with Low-Brilliance X-ray Sources. *Nature Physics* **2,** 258 (2006) (Cited on pages 2, 20, 27).

[Pfeiffer, 2008] Pfeiffer, F. *et al.* Hard-X-ray Dark-Field Imaging using a Grating Interferometer. *Nature Materials* **7,** 134–137 (2008) (Cited on pages 2, 20).

[Pfeiffer, 2007b] Pfeiffer, F. *et al.* High-resolution brain tumor visualization using three-dimensional x-ray phase contrast tomography. *Physics in Medicine & Biology* **52,** 6923 (2007) (Cited on page 35).

[Pfeiffer, 2005] Pfeiffer, F. *et al.* Shearing interferometer for quantifying the coherence of hard X-ray beams. *Physical Review Letters* **94,** 164801 (2005) (Cited on page 26).

[Prade, 2016] Prade, F., Yaroshenko, A., Herzen, J. & Pfeiffer, F. Short-range order in mesoscale systems probed by X-ray grating interferometry. *EPL (Europhysics Letters)* **112,** 68002 (2016) (Cited on page 26).

[Prop, 1984] Prop, J., Ehrie, M., Crapo, J., Nieuwenhuis, P. & Wildevuur, C. R. Reimplantation response in isografted Rat Lungs: Analysis of causal Factors. *The Journal of Thoracic and Cardiovascular Surgery* **87,** 702–711 (1984) (Cited on page 70).

[Rayleigh, 1881] Rayleigh, L. XXV. On copying Diffraction-Gratings, and on some Phenomena connected therewith. *The London, Edinburgh, and Dublin Philosophical Magazine and Journal of Science* **11,** 196–205 (1881) (Cited on page 19).

[Reece, 2008] Reece, T. B. *et al.* Native Lung Volume Reduction Surgery relieves functional Graft Compression after Single-Lung Transplantation for Chronic Obstructive Pulmonary Disease. *The Journal of Thoracic and Cardiovascular Surgery* **135,** 931–937 (2008) (Cited on page 71).

[Reis, 1995] Reis, A., Giaid, A., Serrick, C. & Shennib, H. Improved outcome of Rat Lung Transplantation with Modification of the Nonsuture External Cuff Technique. *The Journal of Heart and Lung Transplantation: the Official Publication of the International Society for Heart Transplantation* **14,** 274–279 (1995) (Cited on page 71).

[Revol, 2011] Revol, V. *et al.* X-ray Interferometer with Bent Gratings: Towards larger Fields of View. *Nuclear Instruments and Methods in Physics Research Section A: AcceleRators, Spectrometers, Detectors and Associated Equipment* **648,** S302–S305 (2011) (Cited on page 49).

[Röntgen, 1896] Röntgen, W. C. Eine neue Art von Strahlen. *MitteiLung. Sitzungsberichte der Physikalisch-medizinischen Gesellschaft zu Würzburg* **137** (1896) (Cited on page 1).

[Royer, 2016] Royer, P.-J. *et al.* Chronic Lung Allograft Dysfunction: a systematic Review of Mechanisms. *Transplantation* **100,** 1803–1814 (2016) (Cited on page 61).

[Russo, 2017] Russo, P. *Handbook of X-ray Imaging: Physics and Technology* (Taylor & Francis, 2017) (Cited on pages 5, 9, 17).

[Samano, 2009] Samano, M. *et al. Bronchial Complications following Lung Transplantation* in *Transplantation Proceedings* **41** (2009), 921–926 (Cited on page 62).

[Santacruz, 2009] Santacruz, J. F. & Mehta, A. C. Airway Complications and Management after Lung Transplantation: Ischemia, Dehiscence, and Stenosis. *Proceedings of the American Thoracic Society* **6,** 79–93 (2009) (Cited on pages 62, 69).

[Scherer, 2017] Scherer, K. *et al.* X-ray Dark-field Radiography-In-Vivo Diagnosis of Lung Cancer in Mice. *Scientific Reports* **7,** 402 (2017) (Cited on pages 3, 61, 77, 79).

[Schleede, 2012] Schleede, S. *et al.* Emphysema Diagnosis using X-ray Dark-Field Imaging at a Laser-Driven Compact Synchrotron Light Source. *Proceedings of the National Academy of Sciences* **109,** 17880–17885 (2012) (Cited on page 62).

[Schröter, 2017] Schröter, T. J. *Vergrößerung des Sehfeldes der Röntgen-Phasenkontrast-Bildgebung für die klinische Anwendung* PhD thesis (Karlsruher Institut für Technologie, 2017) (Cited on pages 60, 92).

[Semple, 2017] Semple, T., Calder, A., Owens, C. & Padley, S. Current and future Approaches to large Airways Imaging in Adults and Children. *Clinical Radiology* **72,** 356–374 (2017) (Cited on page 69).

[Shofer, 2013] Shofer, S. *et al.* Significance of and Risk Factors for the Development of Central Airway Stenosis after Lung Transplantation. *American Journal of Transplantation* **13,** 383–389 (2013) (Cited on page 69).

[Smirnova, 2019] Smirnova, N. F. *et al.* Inhibition of B Cell-dependent Lymphoid Follicle Formation prevents Lymphocytic Bronchiolitis after Lung Transplantation. *JCI Insight* **4** (2019) (Cited on page 63).

[Snigirev, 1995] Snigirev, A., Snigireva, I., Kohn, V., Kuznetsov, S. & Schelokov, I. On the Possibilities of X-ray Phase Contrast MicroImaging by Coherent High-Energy Synchrotron Radiation. *Review of Scientific Instruments* **66,** 5486–5492 (1995) (Cited on pages 2, 18).

[Soyer, 1997] Soyer, P. *et al.* Computed Tomography of Complications of Lung Transplantation. *European Radiology* **7,** 847–853 (1997) (Cited on page 62).

[Strobl, 2014] Strobl, M. General Solution for quantitative Dark-Field Contrast Imaging with Grating Interferometers. *Scientific Reports* **4,** 7243 (2014) (Cited on page 26).

[Swensen, 2003] Swensen, S. J. *et al.* Lung Cancer Screening with CT: Mayo Clinic Experience. *Radiology* **226,** 756–761 (2003) (Cited on page 73).

[Takeda, 2007a] Takeda, T. *et al.* Adenoviral Transduction of MRP-1/CD9 and KAI1/CD82 inhibits lymph node Metastasis in orthotopic Lung Cancer Model. *Cancer Research* **67,** 1744–1749 (2007) (Cited on pages 74, 75).

[Takeda, 2007b] Takeda, Y. *et al.* Deletion of tetraspanin Cd151 results in decreased pathologic Angiogenesis *in vivo* and *in vitro*. *Blood* **109,** 1524–1532 (2007) (Cited on pages 74, 75).

[Talbot, 1836] Talbot, H. F. LXXVI. Facts relating to Optical Science. No. IV. *The London, Edinburgh, and Dublin Philosophical Magazine and Journal of Science* **9,** 401–407 (1836) (Cited on pages 2, 19).

[Tapfer, 2013] Tapfer, A. *Small Animal X-ray Phase-Contrast Imaging* PhD thesis (Technical University of Munich, 2013) (Cited on pages 2, 25, 41).

[Thuering, 2014] Thuering, T. & Stampanoni, M. Performance and optimization of X-ray grating interferometry. *Philosophical Transactions of the Royal Society A: Mathematical, Physical and Engineering Sciences* **372,** 20130027 (2014) (Cited on page 52).

[Thüring, 2011] Thüring, T. *et al.* High Resolution, Large Field of View X-ray Differential Phase Contrast Imaging on a Compact Setup. *Applied Physics Letters* **99,** 041111 (2011) (Cited on page 49).

[Tomasi, 1998] Tomasi, C. & Manduchi, R. *Bilateral filtering for gray and color images* in *Sixth international conference on computer vision (IEEE Cat. No. 98CH36271)* (1998), 839–846 (Cited on page 84).

[Travis, 2011] Travis, W. D. *et al.* International Association for the Study of Lung Cancer/American Thoracic Society/European Respiratory Society International multidisciplinary Classification of Lung Adenocarcinoma. *Journal of Thoracic Oncology* **6,** 244–285 (2011) (Cited on page 73).

[Umkehrer, 2020a] Umkehrer, S. *et al.* A proof-of principal study using phase-contrast imaging for the detection of large airway pathologies after lung transplantation. *Scientific Reports* **10,** 1–9 (2020) (Cited on pages 61, 65, 68).

[Umkehrer, 2020b] Umkehrer, S. *et al.* Dark-field CT imaging visualizes micromorphological changes in murine lung tumors. in preparation (2020) (Cited on page 73).

[Umkehrer, 2019] Umkehrer, S. *et al.* Optimization of *in vivo* murine X-ray Dark-Field Computed Tomography. *Review of Scientific Instruments* **90,** 103103 (2019) (Cited on pages 39, 51, 58).

[vKlaveren, 2009] Van Klaveren, R. J. *et al.* Management of Lung Nodules detected by Volume CT Scanning. *New England Journal of Medicine* **361,** 2221–2229 (2009) (Cited on page 74).

[Velroyen, 2015] Velroyen, A. *X-ray Phase-Contrast and Dark-Field Imaging of Small Animals: Contrast Enhancement and In Vivo Imaging* PhD thesis (Technical University of Munich, 2015) (Cited on pages 2, 42).

[Velroyen, 2015] Velroyen, A. *et al.* Grating-Based X-ray Dark-Field Computed Tomography of living Mice. *EBioMedicine* **2,** 1500–1506 (2015) (Cited on page 86).

[Viermetz, 2015] Viermetz, M. *Optimization of a High Sensitivity X-Ray Phase-Contrast Computed Tomography Setup* MA thesis (Technical University of Munich, 2015) (Cited on page 44).

[vTeuffenbach, 2017] Von Teuffenbach, M. *et al.* Grating-based Phase-Contrast and Dark-Field Computed Tomography: a single-shot Method. *Scientific Reports* **7,** 7476 (2017) (Cited on pages 42, 93).

[Weitkamp, 2005] Weitkamp, T. *et al.* X-ray Phase Imaging with a Grating Interferometer. *Optics Express* **13,** 6296–6304 (2005) (Cited on pages 2, 19, 22, 41).

[White, 1977] White, D. An analysis of the Z-dependence of Photon and Electron Interactions. *Physics in Medicine & Biology* **22,** 219 (1977) (Cited on page 13).

[WHO, 2018] WHO. [July-2019]. WHO. %7Bwww.who.int/news-room/fact-sheets/detail/Cancer%7D (2019) (Cited on page 73).

[Wilkins, 1996] Wilkins, S., Gureyev, T. E., Gao, D., Pogany, A. & Stevenson, A. Phase-Contrast Imaging using polychromatic hard X-rays. *Nature* **384,** 335 (1996) (Cited on page 18).

[Willer, 2018] Willer, K. *et al.* X-ray Dark-Field Imaging of the Human Lung - A feasibility Study on a deceased Body. *PLOS ONE* **13,** e0204565 (2018) (Cited on pages 3, 94).

[Wilson, 2008] Wilson, D. O. *et al.* The Pittsburgh Lung Screening Study (PLuSS) outcomes within 3 years of a first Computed Tomography Scan. *American Journal of RespiRatory and Critical Care Medicine* **178,** 956–961 (2008) (Cited on page 74).

[Wolf, 2015] Wolf, J. *et al.* Lens-term-and Edge-effect in X-ray Grating Interferometry. *Biomedical Optics Express* **6,** 4812–4824 (2015) (Cited on page 26).

[Yang, 2012] Yang, Y. & Tang, X. The second-order differential Phase Contrast and its retrieval for Imaging with X-ray Talbot Interferometry. *Medical Physics* **39,** 7237–7253 (2012) (Cited on page 26).

[Yaroshenko, 2015] Yaroshenko, A. *X-Ray Dark-Field Imaging For Diagnosis of Pulmonary Disorders* PhD thesis (Technical University of Munich, 2015) (Cited on page 3).

[Yaroshenko, 2013] Yaroshenko, A. *et al.* Pulmonary Emphysema Diagnosis with a preclinical Small-Animal X-ray Dark-Field Scatter-Contrast Scanner. *Radiology* **269,** 427–433 (2013) (Cited on pages 61, 62, 83).

[Yashiro, 2010] Yashiro, W., Terui, Y., Kawabata, K. & Momose, A. On the origin of visibility Contrast in X-ray Talbot Interferometry. *Optics Express* **18,** 16890–16901 (2010) (Cited on page 26).

[Yashiro, 2015] Yashiro, W. & Momose, A. Effects of unresolvable edges in Grating-based X-ray differential Phase Imaging. *Optics Express* **23,** 9233–9251 (2015) (Cited on page 26).

[Zanette, 2012] Zanette, I. *et al.* Trimodal Low-Dose X-ray Tomography. *Proceedings of the National Academy of Sciences* **109,** 10199–10204 (2012) (Cited on page 42).

Publications and Scientific Presentations

Publications as first author

Umkehrer, S., Birnbacher, L., Burkhardt, R., von Teuffenbach, M., Yildirim, A. Ö., Pfeiffer, D., Herzen, J., & Pfeiffer, F. Optimization of *in vivo* murine X-ray Dark-Field Computed Tomography. *Review of Scientific Instruments* **90**, 103103 (2019)

Umkehrer, S., Morrone, C., Dinkel, J., Aigner, L., Reiser, M. F., Herzen, J., Yildirim, A. Ö., Pfeiffer, F., & Hellbach, K. A proof-of principal study using phase-contrast imaging for the detection of large airway pathologies after lung transplantation. *Scientific Reports* 10 (1), 2020

Umkehrer, S., Kimm, M. A., Haas, H., Busse, M., Achterhold, K., Pfeiffer, D., Pfeiffer, F., & Herzen, J. Dark-field CT imaging visualizes micromorphological changes in murine lung tumors. *in preparation*

Publications as co-author

Smirnova, N. F., Conlon, T. M., Morrone, C., Dorfmuller, P., Humbert, M., Stathopoulos, G., **Umkehrer, S.**, Pfeiffer, F., Yildirim, A. Ö., & Eickelberg, O. Inhibition of B cell–dependent lymphoid follicle formation prevents lymphocytic bronchiolitis after lung transplantation. *JCI Insight* **4** (2019)

Burkhardt, R., Gora, T., Fingerle, A. A., Sauter, A. P., Meurer, F., **Umkehrer, S.**, von Teuffenbach, M., Kampfer, S., Schilling, D., Feuchtinger, A., Walch, A. K., Rummeny, E., Combs, S. E., Schmid, T. E., Pfeiffer, F., Wilkens, J. J., Herzen, J. Early Detection of Radiation-Induced Lung Damage with X-ray Dark-field Radiography in Mice. *European Radiology* (2020)

Oral presentation

Characterization and optimization of a small animal *in-vivo* grating-based dark-field CT scanner. *DPG-Frühjahrstagung, Regensburg, Germany, April 2019*

Poster presentations

First Experiences with *In-vivo* X-ray Dark-Field Imaging of Lungs after Pulmonary Transplantation in Mice. *KNMF User Meeting, Karlsruhe, Germany, March 2017*

Optimization of the first *in-vivo* X-Ray Dark-field and Phase-Contrast CT-Scanner. *International Symposium on Biomedical Applications of X-ray Phase-Contrast Imaging (IMXP), Garmisch-Partenkirchen, Germany, January 2018*

Acknowledgments

This thesis would not have been possible without the help of many, many people, but in particular I would like to thank...

- my academic supervisor **Prof. Franz Pfeiffer** for giving me this unique possibility to do my doctorate at his Chair of Biomedical Physics in such an inspiring environment and on such a fascinating topic. Thank you for your support, mentoring and sharing your knowledge with me and for all your input.
- my second supervisor **Prof. Julia Herzen** for many enlightening and fruitful discussions, patiently answering all my questions, and her close support throughout all aspects. Thank you for your trust, keeping me motivated and for always having an open door for me.
- **Dr. Lorenz Birnbacher** for all your support and your expertise within the last years and all your numerous proof-readings and suggestions for improvement.
- **Rico Burkhardt** and **Dr. Maximilian v. Teuffenbach** for the good teamwork during this time. Thanks for all the help with various modifications of the setup, all your good ideas and input, and all the support during the project.
- **Lisa Heck** and **Manuela Frank** for all those funny moments, your support in various aspects, and your proof-reading.
- **Simon Pinzek** and **Alex Gustschin** for sharing all your expertise, answering all my questions and eliminating all my doubts especially in regards of all grating-related topics.
- **o**ur collaborators, namely Dr. Katharina Hellbach, **Dr. Melanie Kimm**, and **Dr. Helena Haas** for all your medical and biological expertise and support. Thanks for all your help at the experiments, evaluating and interpreting the results from a different perspective and the interdisciplinary exchange. It was quite a new experience for me and this would not have been possible without you.
- **Nelly de Leiris** and **Dr. Klaus Achterhold** for their support in all administrative and organizational issues.
- **Dr. Martin Dierolf** for keeping up the IT infrastructure at the chair and who helped me more than once with any computer-related problems.
- **Nico Gustschin** for all your support concerning 3D printing.

- The whole group for providing this nice working atmosphere. Especially Christoph, Simone, Kirsten, Jana, Simon, Manuela, Theresa, and Clemens for all of those the enjoyable table-kicker matches we had! Thank you all for all the funny moments we had together, for the legendary singstar evenings, the enjoyable lunch breaks, the nice Christmas parties!

- last but not least, I like to thank my whole family, my friends and Lisa for your continuous support and the motivating words you had if I needed them.